Planet Formation in Radiatively Inefficient Protoplanetary Discs.

Hellary, Phil

Planet Formation in Radiatively Inefficient Protoplanetary Discs

Phil Hellary

Astronomy Unit

Queen Mary, University of London

A thesis submitted for the degree of

Doctor of Philosophy

December 2012

This thesis is dedicated to the memory of my parents.

Declaration

I hereby declare that the work presented in my thesis entitled *Planet Formation in Radiatively Inefficient Protoplanetary Discs* is my own.

Parts of Chapter 2 contains material that has been published in a peer review journal in the following article:

- Hellary, P., Nelson, R. P. (2012), Planet Formation in Radiatively Inefficient Protoplanetary Discs, MNRAS, 419, 2737

Parts of Chapter 3 contains material that is currently being prepared for submission for publication in a peer reviewed journal.

Acknowledgements

I am incredibly grateful for the support and encouragement of my supervisor, Richard Nelson, throughout my time as his student. His knowledge and experience has been an invaluable help to me over the years.

My thanks to my fellow PhD students, past and present, particularly Moritz Fragner and Stephen Fendyke and to the rest of the Planetary Formation and Dynamics research group at QMUL.

I thank the administrative staff in the Department of Mathematics, particularly Bill White who so tirelessly battled the finance department to make sure I got paid.

My thanks to my friends and family for putting up with me being a student for so long.

My thanks to Molly, my cat, for only deleting part of this thesis by stamping over the keyboard and my thanks to my dog, Ruby, for keeping my lap warm during the long nights of research.

Finally, I thank my wife, Catherine, for her love and support and for so selflessly taking over wedding planning while I finished off my research.

Abstract

I examine the effects on planetary system formation of radiatively inefficient disc models where positive corotation torques may counter the rapid inward migration of low-mass planets driven by Lindblad torques. I use N-body simulations coupled with algorithms to model the evolution of the gas disc, type I migration, gap formation and type II migration, planetary atmospheres that enhance the probability of planetesimal accretion by protoplanets, gas accretion on to forming planetary cores and gas disc dispersal.

The inclusion of entropy and vorticity related corotation torques can lead to a net positive torque thus giving rise to outward migration of planets. This can allow larger planets to survive for a longer period of time, allowing some planets to accrete enough gas within the lifetime of the disc to undergo runaway gas accretion thus forming gas giant planets.

I review the current status of extrasolar planet observations and the methods with which these observations are made, and provide a contextual review of the theory of planet formation.

Using these models, I have successfully formed a number of gas giant planets with semi-major axes ranging from 0.1 AU up to 75 AU and masses from 100 Earth masses through to 700 Earth masses, as well as a large number of terrestrial sized planets. In later simulations, a large number of super-Earth, Neptune-mass and gas planets that are too small to be considered giants were formed also.

Contents

List of Figures

List of Tables

Chapter 1

Introduction

1.1 Known Extrasolar Planets

In recent years, a highly diverse population of planets has been observed orbiting main sequence stars. From short period rocky super-Earths such as CoRot-7b (4.8 Earth masses with period 0.85 days) [Léger et al., 2009] and Kepler-10b (4.55 Earth masses with period 0.84 days) [Batalha et al., 2011] through to the very long period massive gas giant planets detected via direct imaging such as beta Pic b (8 Jupiter masses with period 7300 days) [Lagrange et al., 2010] and HR 8799 d (10 Jupiter masses with period 41054 days). Conversely, there have also been discoveries of short-period hot-Jupiters such as 51-Peg b (0.47 Jupiter masses with period 4.23 days) [Mayor and Queloz, 1995] and Wasp-18 b(10.43 Jupiter masses with period 0.94 days) [Hellier et al., 2009] and also some longer period super-Earths such as HD 20794 d (4.8 Earth masses with period 90.31 days) (Pepe et. al. 2011) although observations for such small planets are increasingly difficult with longer periods. Formalhaut b, originally thought to be a long period Jupiter-massed object [Kalas et al., 2008] now, thanks to high resolution observations using ALMA, appears to be a small body no larger than a few Earth masses with a companion with an even greater period on the outside of the system's dust ring [Boley et al., 2012]. Hot Neptunes have also been observed such as Gliese 436b (23.43 Earth masses with period 2.64 days) [Butler et al., 2004] and Kepler-4 b (24.48 Earth masses with period 3.21 days) [Borucki et al., 2011]. Again, such

planets have been found with larger periods such as HD 10180 g (21.40 Earth masses with period 601.20 days) [Moutou et al., 2011] and HD 192310 c (24 Earth masses with period 525.8 days) [Pepe et al., 2011]. Observational discoveries of multiple-planet systems are also now becoming common such as the five planet system orbiting the star 55 Cancri consisting of gas giants and Neptune-mass bodies [Fischer et al., 2008], the HR 8799 system that reportedly contains four massive planets between 4 and 10 Jupiter masses [Marois et al., 2008] and the recently reported Kepler-11 system consisting of six nearly coplanar planets - mostly low mass Neptune-mass bodies and super Earths but with perhaps one Jupiter mass planet orbiting at a larger distance [Lissauer et al., 2011].

A question that needs to be addressed is whether a particular model of planet formation, such as the core-accretion model, can explain this broad diversity of observed planets - robust enough in its variety so as to explain the wide range of observed systems. Alternatively, it might be the case that very different physical processes are operating on different length and/or timescales within protoplanetary discs so as to form planets with such diverse characteristics. For example, core-accretion at locations relatively close to the central star and operating on long time scales might form short period systems [Pollack et al., 1996] while gravitational fragmentation occurring at large radii on short-time scales might form long-period giant planets or low mass brown dwarfs [Boss, 1997; Stamatellos and Whitworth, 2008].

In order to begin addressing this question in detail, it is necessary to construct models of planetary formation that are global in their reach - they must allow for the formation of multiple planet systems with a large diversity of masses and orbital elements (semimajor axes, eccentricities, inclinations etc). In this thesis, I present the results from global models that are based on the oligarchic growth scenario for planet formation, that have been constructed using a symplectic N-body code [Chambers, 1999] combined with first a simplified prescription for the gas disc model (Chapter 3) and then combined with a self-consistent 1D evolving disc model (Chapter 4). The models also include planetary migration, the accretion of planetesimals, gas-envelope accretion, and disc dispersal on Myr time scales. One of the main objectives in this work is to examine how our current understanding of migration of low-mass planets influences the formation of planetary systems,

with particular emphasis on the corotation torques in radiatively-inefficient discs [Paardekooper et al., 2010, 2011]. The prescriptions I have used in both of these studies for a number of physical processes, such as gas accretion, are very simplified due to computational necessity. However, they serve the useful purpose of enabling N-body simulations to be performed of planetary system formation that leads to a diversity of outcomes which can be used to guide future model developments.

A substantial body of previous work exists that has examined the role of migration in the formation of planets using N-body simulations. Papaloizou and Larwood [2000] utilised N-body simulations modelling planet-planet collisions combined with a prescription for migration and eccentricity/inclination damping to examine planetary growth. McNeil et al. [2005] and Daisaka et al. [2006] examined the effects on terrestrial planet formation of type I migration and Fogg and Nelson [2007, 2009] examined the influence of type I migration on the formation of terrestrial planets in the presence of migrating Jovian-mass planets. Terquem and Papaloizou [2007] used N-body simulations with Type I migration to examine the formation of hot super-Earths and Neptunes and McNeil and Nelson [2009, 2010] carried out large-scale simulations of oligarchic growth to explore the formation of systems of hot-Neptunes and super-Earths such as those around the stars Gliese 581 and HD698433, using a novel symplectic integrator with multiple timesteps.

An alternative to these approaches has been planetary population synthesis modelling, as presented by Ida and Lin [2010]; Ida et al. [2008], Mordasini et al. [2009a], Mordasini et al. [2009b] and Miguel et al. [2011]. These monte-carlo based approaches have significant advantages in being able to cover a very broad range of parameter space thus allowing meaningful statistical comparisons with observational data to be undertaken. The computational efficiency of such regimes also allows complex models of planetary atmospheres and gas accretion to be included as presented by the Mordasini et al work. However, accurate treatment of planet-planet gravitational interactions are difficult to include in these models with the result that predictions about planetary system multiplicity, orbital eccentricities and inclinations are not a natural outcome of the models (although note that models by Ida and Lin [2010] do now include a simplified treatment of

planet-planet interaction dynamics).

1.2 Detection Methods for Extrasolar Planets

There are now six known methods that have been used for the detection of extrasolar planets.

1.2.1 Radial velocity observations

As planets are not massless bodies, they exert a gravitational pull on their parent star. Although the star's gravitational potential is far more significant, a planet's mass alters the centre of gravity of a system so that both bodies co-orbit a common centre of mass. In the case of binary stars, this common centre of mass can often reside at a point of space between both bodies, however, in the case of a planet orbiting a star, the centre of mass usually resides inside the star. This has the effect of causing a 'wobble' in the star's motion.

This can be observed via spectroscopy due to the frequency of photons from the star being doppler shifted in response to the movement of the star along the line of sight 1.1.
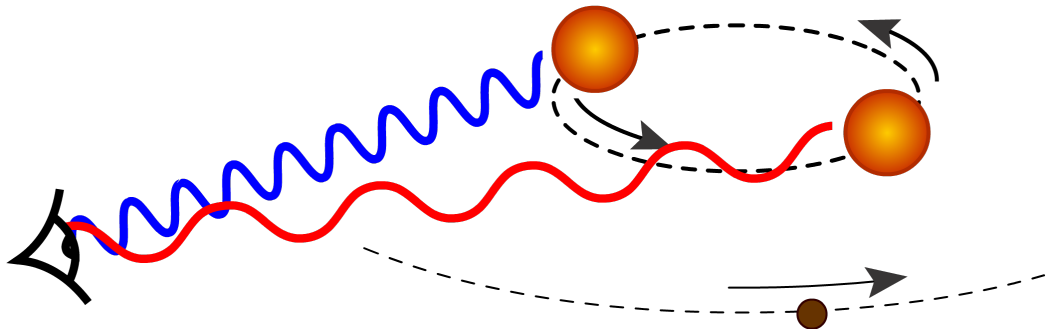
Figure 1.1: The doppler effect changes to the frequency of light from a star undergoing a 'wobble' due to the gravitational interaction with an orbiting planet.

The observed velocity of a star of mass $M_\odot$ with an attendant planet of mass

M_p in a circular orbit of radius r is

$$v_\mathrm{observed} \leq \frac{M_\mathrm{p}}{M_\odot} \sqrt{\frac{GM_\odot}{r}} \sin i \tag{1.1}$$

where i is the inclination of the planet's orbit to the line of sight of the observer.

This method of planet detection can only give us a lower limit for a planet's mass due to the inclusion of the inclination i in the calculated result - $M_\mathrm{p} \sin i$. However, there is additional information that can be gleaned about a planet's characteristics using this method.

A planet on a circular orbit around an observed star will affect the same gravitational pull throughout the orbit. For a planet on an eccentric orbit, it moves faster at pericentre than at apocentre and correspondingly, the observed velocity of the star will also be greater at pericentre. Thus variations in the magnitude of the radial velocity can give us information as to the eccentricity of an extrasolar planet.

An example of an observed radial velocity curve of a planet on a circular orbit is shown in figure 1.2 [Mayor and Queloz, 1995] and an example of an observed radial velocity curve for an eccentric orbit is shown in figure 1.3 [Pepe et al., 2002].

1.2.2 Transit surveys

If an extrasolar planet's orbital plane is edge on to an observer then it will cross a path between the observer and its parent star then there will be a dip in the observed stellar flux.

The observed flux from a star is directly proportional to it's cross-sectional area and the area concealed by a transiting planet is equal to the planet's cross sectional area. Thus it follows that the decrease in the observed flux from the star is

$$\frac{\Delta F_\odot}{F_\odot} = \left(\frac{R_\mathrm{p}}{R_\odot}\right)^2. \tag{1.2}$$

Observations of this nature have a low probability of occurring as a planetary orbit must be observed almost edge on for an observer in order for a transit to be
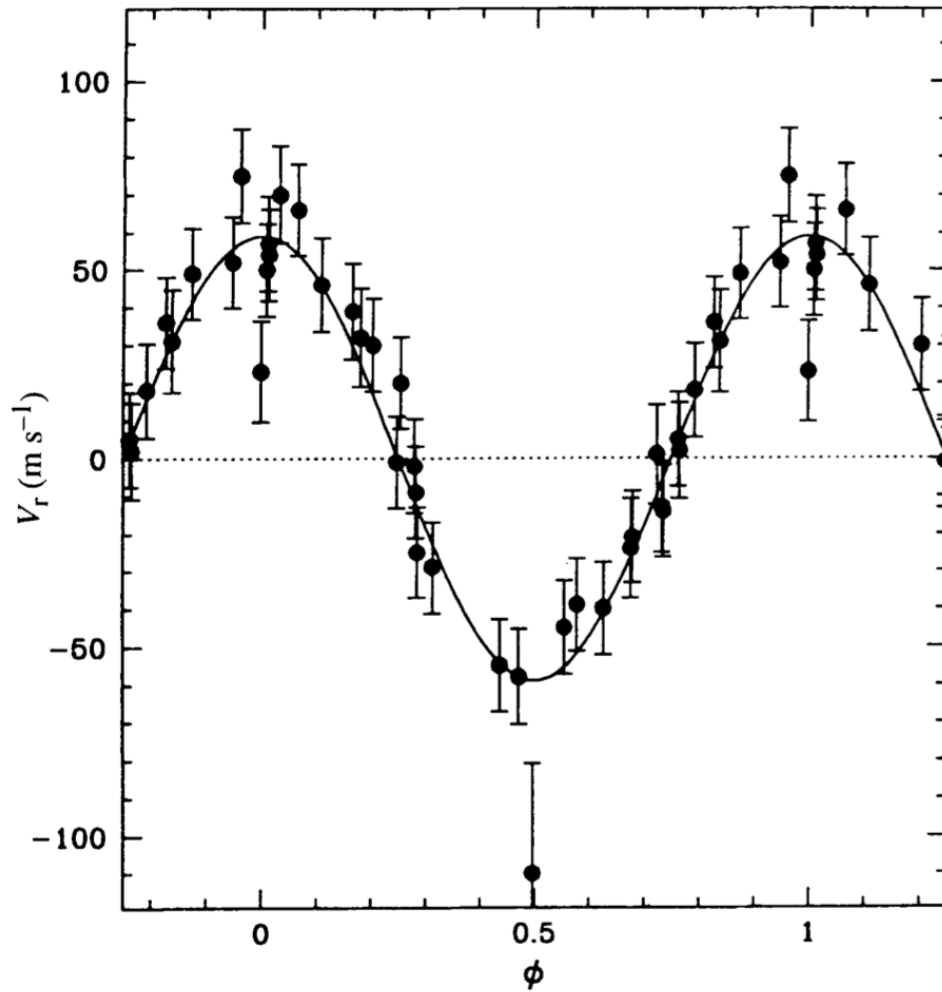
Figure 1.2: The radial velocity survey results for 51 Pegasi which led to the discovery of the first planet to be detected orbiting a main sequence star, 51 Pegasi b.
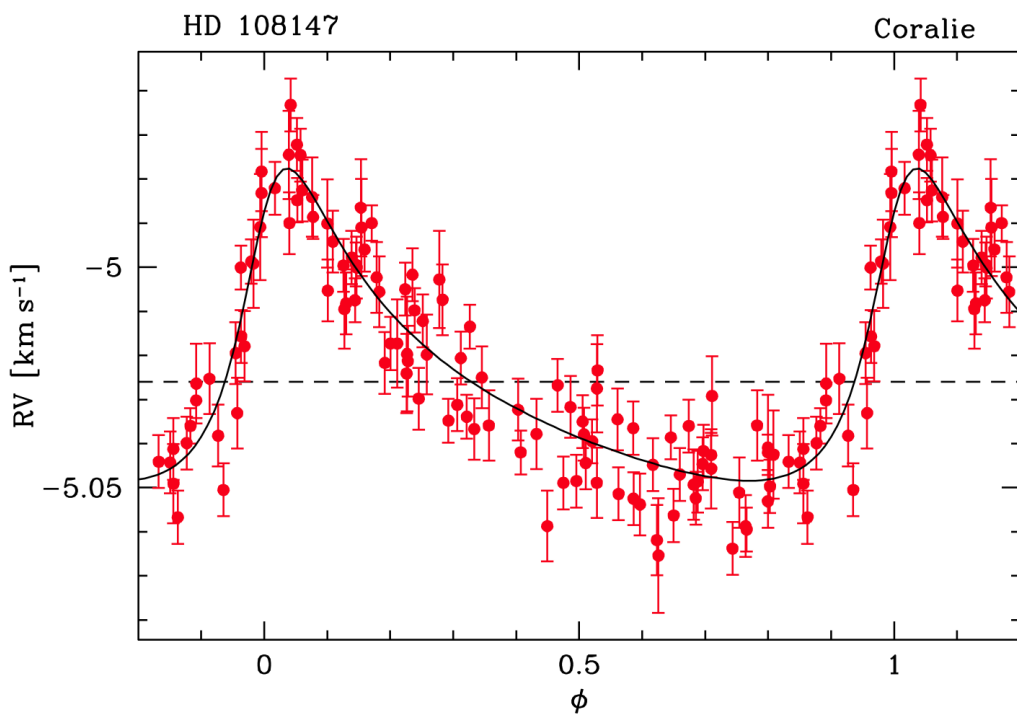
Figure 1.3: The radial velocity survey results for HD 108147 which led to the discovery of the hot Jupiter, HD 108147 b, a planet on an eccentric orbit.
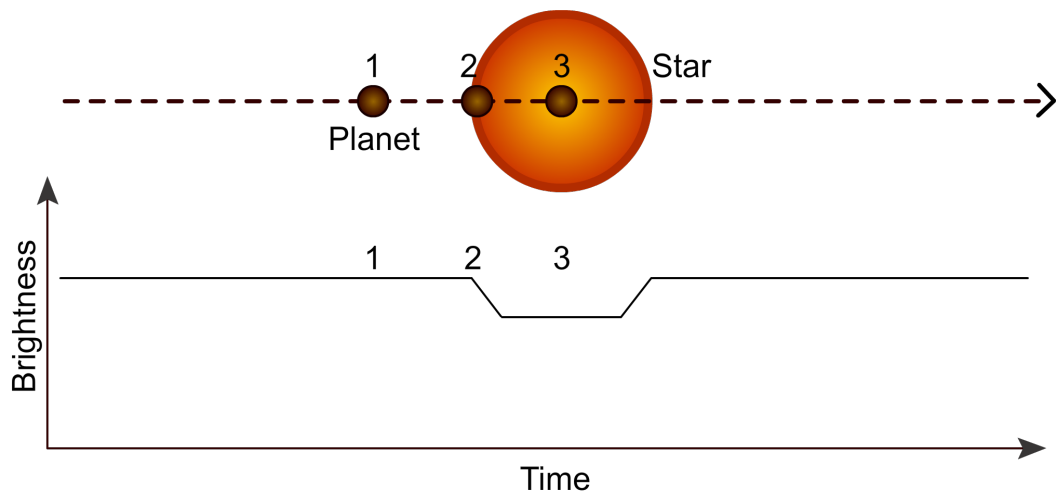
Figure 1.4: The effect on observed brightness of a star as a planet crosses across the star's surface. At (1) the star is not occluded at all and the flux is correspondingly constant. At (2) the planet is beginning to occlude part of the star and so the flux detected begins to drop. At (3) the whole planet is occluding part of the star so the drop in observed stellar flux is at a maximum.

detected. The probability of such an orbit occurring is proportional to the ratio of a star's diameter to the diameter of the orbit. This probability decreases the further away from a star a planet orbits.

Also, small planets produce a very small dip in flux. A Jupiter sized planet orbiting a solar type star would give rise to a drop in stellar flux of approximately 1 percent whereas a terrestrial Earth sized planet would only give rise to around a 0.01 percent drop in observed flux. Furthermore, a planet needs to be observed multiple times in order to calculate the orbital period of a planet to reasonable accuracy - at least three observed transits are required (two for the initial measurement of the orbital period, the third for confirmation).

For these reasons, it is necessary to continuously monitor a large number of stars over a long period of time in order to have a chance to detect potential extrasolar planets. As an example, the Kepler spacecraft is performing transit surveys over 0.28 percent of the sky and is planned to do so for at least 7.5 years. It is observing approximately 150,000 stars. It has currently been operational for about 3.5 years which means that the longest period planets that it has reasonably

been able to detect due to the requirements of multiple observations is about a third of this. The longest period planet currently detected by Kepler is Kepler-22b and has a period of 289.86 days.

Transit surveys unfortunately have a high rate of false detections due to various other phenomena producing similar affects on a star's apparent flux such as eclipsing binary stars, star spots and stellar luminosity fluctuations. However, when coupled with radial velocity observations, they can produce a rich amount of information about a planet. The radius of a planet can be calculated and thus when combined with the mass provided by a radial-velocity observation, it's average density can be evaluated. Not only this but the transit method can even be used to study the atmosphere of a planet. As a planet transits a star, light from the star can pass through the upper atmosphere of the planet (providing the atmosphere is not too optically thick) and studies of the high-resolution stellar spectrum can lead to the detection of elements or compounds present in the planet's atmosphere such as Na, CH_4 or H_2O [Tinetti et al., 2007]. Lastly, when a planet is transiting on the opposite side of a star, a planet's radiation can be measured by subtracting the infra-red photometric intensity before the occultation from that during. These measurements can give a planets temperature. For example, planets TrES-1 and HD 209458b have been measured to have temperatures of 1060 and 1130 K respectively [Charbonneau et al., 2005; Deming et al., 2005].

An example of a transit survey detection curve is shown in figure 1.5 [Fabrycky et al., 2012].

1.2.3 Gravitational microlensing

Einstein's theory of general relativity provides the underpinnings of gravitational lensing - namely that gravity can distort space-time. Light from a distant source star can be focussed due to a foreground lens star, bending the light from the source star (see figure 1.6). If the lens star has an orbiting planet then the planet's gravitational field can also contribute to the lensing effect.

The detected changes in light and the overall magnification can give us information about the distribution of mass of the gravitational lens.
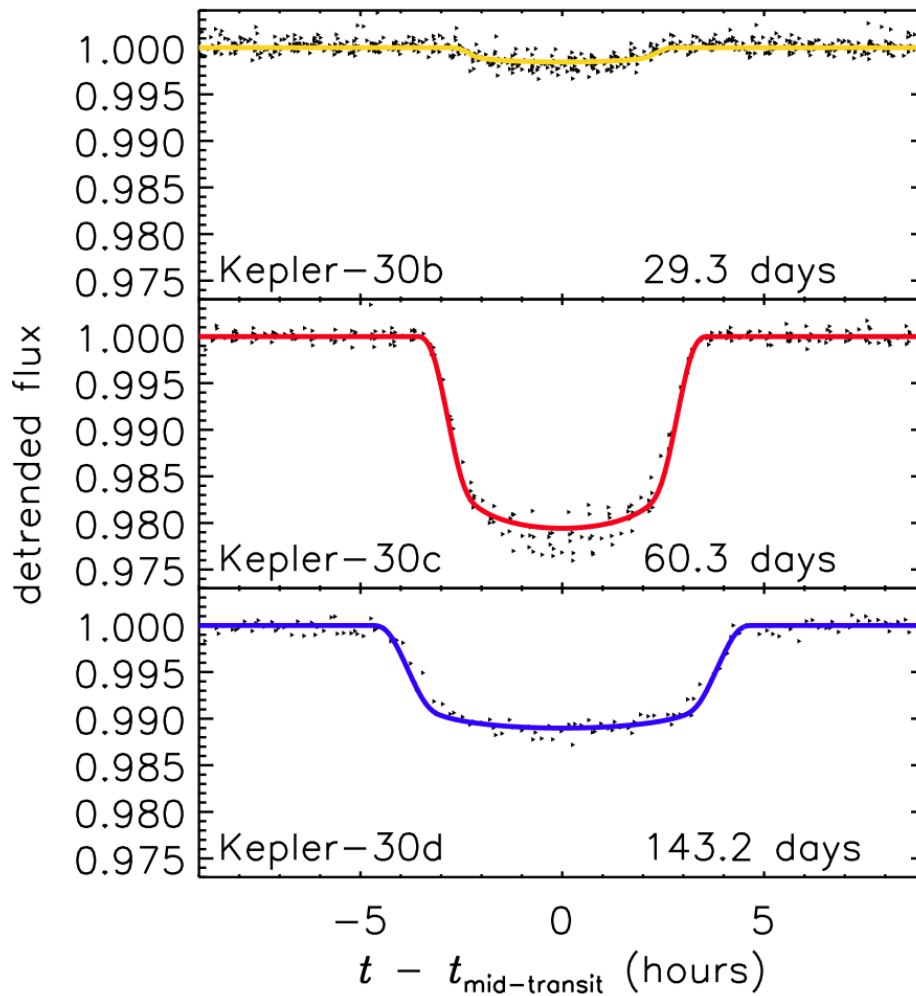
Figure 1.5: The transit survey phase curves for Kepler-30 which shows the detection of three planets around the same star, Kepler-30b, Kepler-30c and Kepler-30c.
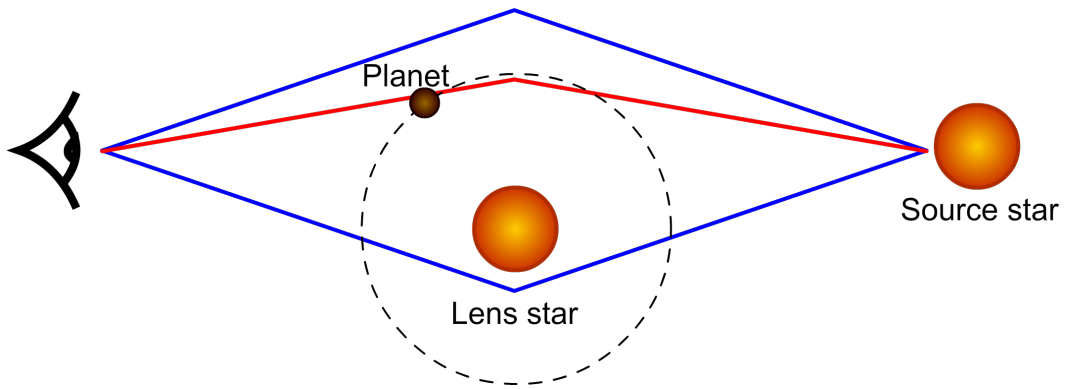
Figure 1.6: The effect of gravitational lensing on distant starlight due to the presence of a planet.

The probability of such an event occurring is very small indeed so a very large number of distant stars have to be continuously observed. Furthermore, since the chance alignment between two stars that leads to a gravitational lensing effect will never happen again, planets detected with this method will only ever be observed once. However, gravitational lensing can be sensitive to smaller planets that are difficult for other detection methods to observe. The first low mass planet to have a relatively large semi-major axis, OGLE-2005-BLG-390Lb, was detected by this method in 2006 [Beaulieu et al., 2006]. Its microlensing light curve is shown in figure 1.7

1.2.4 Direct imaging

Planets are very faint light sources in comparison to the stars they orbit - orders of magnitude fainter. Therefore, light reflected off a planet is usually lost in the glare from the star. However, there are cases when direct detection of a planet is possible - when a planet is large, lies a long way from the parent star and is hot so that it emits a significant amount of infrared radiation (i.e. the planet must be young, ~ 10 Myr old). A coronagraph is used to block the glare of the light from the star so that imaging of light reflected from a planet's surface is possible. Four very large planets, between 4 and 10 Jupiter masses in size were detected by this method in 2008 around star HR 8799 (see figure 1.8) [Marois et al., 2008].
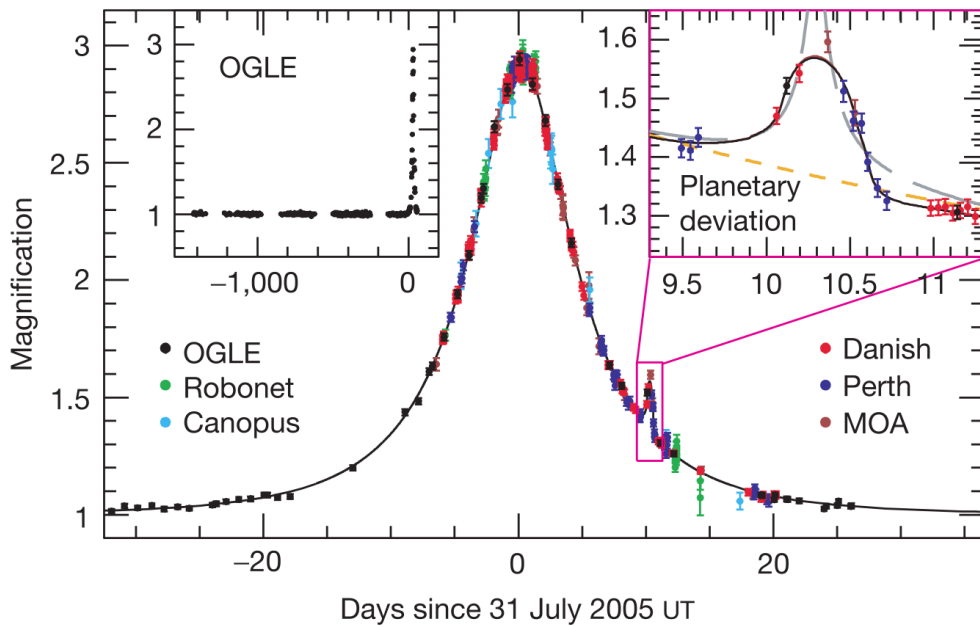
Figure 1.7: The observed light curve used in the detection of OGLE-2005-BLG-390Lb. The anomaly that was used in the detection of the planet is expanded in the top right corner.

Their luminosity and distance from the central star made this detection possible, they are only just within the limits of planet classification since if they were much more massive, deuterium fusion could occur and they would be classified as brown dwarf stars.
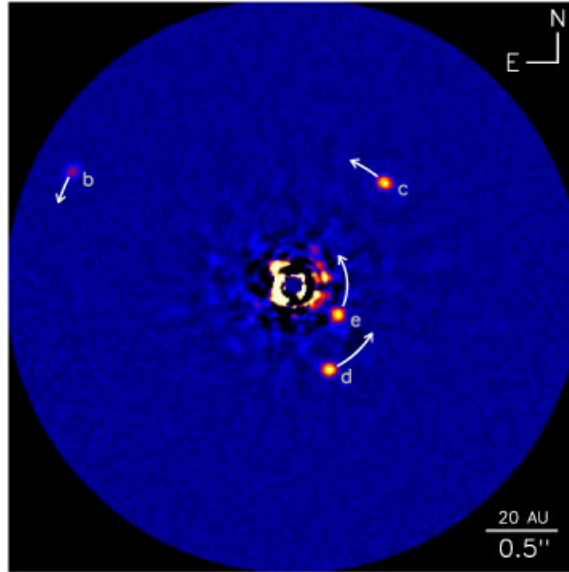
Figure 1.8: A coronagraph of HR 8799 showing four apparent planets around the central star.

1.2.5 Pulsar timing

The method that has produced the lowest number of exoplanet candidates and yet is credited as detecting the very first exoplanets is pulsar timing. Pulsars are a type of neutron star that emit beams of electromagnetic radiation from their magnetic poles. If such a star rotates off axis to these poles then the beams' orientation rotates with the star's rotation. As an observer, this will manifest in a regular pulsating signal as the beam is swung across the observer. The rotation of such stars - and correspondingly the pulsating signal - are so regular that very slight changes to the timings observed can be used to measure a pulsar's motion. Variances in the motion of a star can be used to detect extrasolar planets as described in section 1.2.1. This method is so accurate that very small planets

can be detected, down to dwarf planet sizes. The first planets detected by this method (and thus the first extrasolar planets ever detected) are PSR B1257+12 c and d and were detected in 1992 by Wolszczan and Frail [1992].

1.3 Planet Formation Models

1.3.1 Protoplanetary discs

Planets are formed in protoplanetary discs around young stars. Giant clouds of molecular hydrogen in star forming regions collapse and fragment leading to protostars. At the centre of these, the gas has low angular momentum, allowing it to form a dense, hydrostatically supported protostellar core. Further material is initially prevented from accreting onto this core due to its relatively high angular momentum. Conservation of this causes the surrounding gas to form a rotationally supported disc. A large fraction of this gas then accretes onto the central core through the accretion disc. Once sufficient mass has been accreted by the core, deuterium fusion begins and then hydrogen fusion. By this time, most of the nebula gas has diffused through the disc and has accreted so that a young star (known as a T Tauri star) lies at the centre of the disc that now contains a few percent of the star's mass. It is in these discs - protoplanetary discs - that planet formation occurs according to the core accretion model. We note, however, that fragmentation of the disc during its earlier self-gravity stage may also occur. See figure 1.9.

1.3.2 Gravitational Instability Model

Young, compact objects have been observed in star forming regions right the way through the brown dwarf range down to sub-deuterium-burning masses (e.g. Zapatero Osorio et al. [1999]). There is no reason why the process of gravitational instability that forms stars couldn't extend down to smaller gas giant sized planets, since the opacity limit for fragmentation can reach a few Jupiter masses.

Similar to how gravitational instability leads to the fragmentation of molecular cloud cores which subsequently form protoplanetary discs, the outer regions of the

(a) Nebula

dense cores

(b) Gravitational collapse

(c) Protostar

forming disc

Collapsing envelope

(d) T Tauri star

T Tauri star

protoplanetary disc
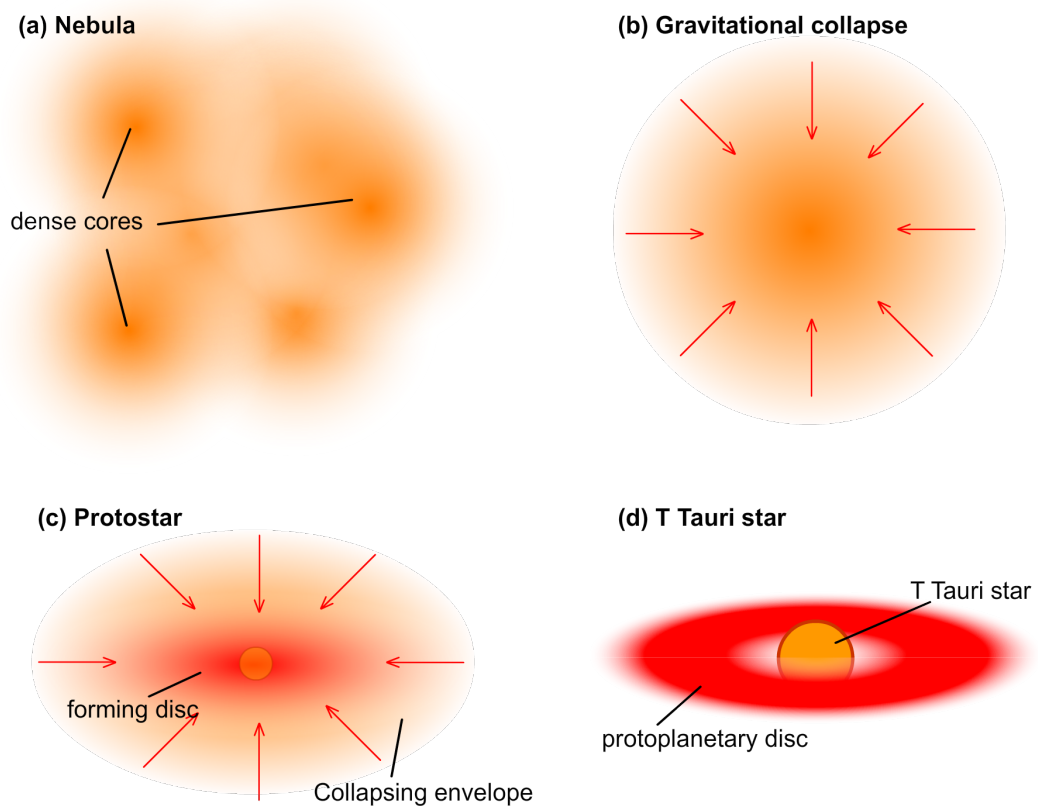
Figure 1.9: The formation of a T Tauri star and a protoplanetary disc.

protoplanetary disc can become gravitationally unstable, fragment and collapse leading to the formation of planets or brown dwarfs (e.g. Boss [1997]; Stamatellos and Whitworth [2008]). However, for such a process to occur, the protoplanetary disc needs to be massive, resulting in planets that are massive gas giants. As such, this method of planet formation can account for a minority of observed extrasolar planets.

Evidence such as the results presented in Matsuo et al. [2007] suggests that the majority of extrasolar planets are contained within a mass and semi-major axis distribution that are inconsistent with the gravitational instability model. Furthermore, the distinct dip in the mass function of observed objects between 10-50 Jupiter masses (the so called 'brown dwarf desert') suggests that the formation of planets via this method is relatively rare [Wuchterl et al., 2000]. I note, however, that recent developments indicate that clumps formed through gravitational instability may migrate inward and experience tidal downsizing, leading ultimately to a range of planet masses [Nayakshin et al., 2011].

1.3.3 Core Nucleated Accretion Model

Instead of building planets from the top down - turning clumps of gas into smaller planets - another approach is from the bottom up. This is the basis for the core nucleated accretion model.

In this model, micrometer sized dust particles, composed primarily of surviving interstellar grains and condensates formed in the protoplanetary disc, slowly collide and stick together and settle toward the mid-plane of the disc. Observations of infrared spectra of young discs show the signatures of this coagulation process [Kessler-Silacci et al., 2006]. Once the concentration of these clumps reaches a high enough density, gravitational instabilities within them can occur leading to the formation of rocky bodies or planetesimals up to about 1-10 km in size [Johansen et al., 2011]. In a more traditional picture, planetesimals may instead form by continued coagulation of dust grains, leading to bodies with size of 1-10km [Weidenschilling, 2000; Windmark et al., 2012].

From here, gravitational interactions between planetesimals leads to a period of rapid runaway accretion where the rate of solid-body accretion is determined

by the mass of the body - more massive bodies accreting more rapidly than less massive ones. Once the larger bodies - now protoplanets - have grown sufficiently in size, the random velocity evolution of the surrounding planetesimals is no longer governed by planetesimal-planetesimal interactions but rather by the gravitational scattering caused by the protoplanets. This leads to an increase in the random velocities of the planetesimals which correspondingly leads to a reduction in the accretion rate for the protoplanets due to the effects of gravitational focussing decreasing. This slower accretion phase is known as oligarchic growth [Kokubo and Ida, 1998].

Due to the dependence of the accretion rate during oligarchic growth on random velocities and the random velocities of planetesimals increasing due to the mass of a planet, this is a self-limiting growth phase. Whilst it has been shown to successfully form planets analogous to present day terrestrial planets [Chambers and Wetherill, 1998], this process on its own cannot grow planets larger than a few Earth masses and struggles to form planets in the giant planet region of our solar system. This is because the formation timescale during oligarchic growth depends on the solid surface density and on the orbital radius.

Gas giant planets are thought to be composed of solid rocky cores surrounded by massive gas envelopes (although cores present during the formation of gas giants could since have shrunk through core erosion processes such as convection).

The rocky cores of gas giants are formed along with rocky planets during oligarchic growth. Planets accrete gas from the surrounding nebula if the escape velocity from the planet is greater than the sound speed in the surrounding protoplanetary disc. For small planets this is a very slow process with planets accreting only very small atmospheres during the lifetime of the gas disc. In order for a planet to be able to grow to a gas giant size, a core of about 10 Earth masses needs to form within the lifetime of the disc [Pollack et al., 1996], however, recent work by Movshovitz et al. [2010] suggests that only about a 3 Earth mass core may be needed.

Once a planet has accreted a sufficient amount of gas mass (approximately the equivalent to its solid core mass), the rate of gas accretion increases rapidly and switches to a phase of runaway gas accretion. This continues until all the gas in the vicinity of the planet's orbit has been accreted and takes of the order

of 10^5 years to complete compared to 10^6 years to accrete all the gas mass prior to this point.

Chapter 2

Theory

2.1 The Minimum Mass Solar Nebula Model

Although we are obviously unable to observe the solar system's original proto-planetary disc, work has been done to calculate what the original mass distribution would have been during the formation of our solar system with the most commonly agreed upon result being the Minimum Mass Nebular Model (MMSN) [Hayashi, 1981].

In the construction of this model, the total observed current mass held in heavy elements throughout the planets, comets and asteroids in the solar system is first calculated. It is then assumed that the heavy element to gas ratio would have been the same in the protoplanetary disc as that which is currently observed in the Sun. Assuming that no heavy elements were lost during the formation of the solar system, this gives an estimate of the total mass of the original protoplanetary disc. It is approximately 1.5% of a solar mass. In order to calculate the original mass distribution of the original disc, an assumption is made that all the planets were formed where they are now (something that does not appear to hold true in my simulations). As such, the total disc mass is smeared out so that it represents the same proportional mass distribution as is currently observed. The mass profile calculated by Hayashi [1981], and referred to as the MMSN profile hereafter, is:

$$\Sigma = 1731 \left(\frac{a}{1\mathrm{AU}} \right)^{-3/2} \mathrm{gcm}^{-2} \tag{2.1}$$

2.2 Ice line density enhancement

Hayashi [1981]'s MMSN model also has a corresponding power law for the equilibrium temperature in the gas disc:

$$T = 280 \left(\frac{a}{1\text{AU}} \right)^{-1/2} \text{K} \tag{2.2}$$

However, if the temperature drops enough, various materials in the disc can condense into solids with the most significant being water condensing into ice. Since we know that the condensation temperature of water is 170 K, we can use equation 2.2 to find the radius at which this enhancement to the solids surface density can occur, 2.7 AU. Within this radius, the MMSN takes the solids' density to be 7.1 g/cm^2 and outside, 30 g/cm^2. In reality, such a discontinuity is unrealistic and the change in density enhancement is likely to be far less sharply defined. In my work, I smear the discontinuity out somewhat as described in section 3.1.1.3. It is noteworthy that analysis of meteorites believed to originate in the asteroid belt indicate a gradient in volatiles, with volatile rich bodies being located in the outer belt at ~ 3 AU and volatile-poor bodies originating in the inner belt around ~ 2 AU. This is supported by spectroscopic observations of asteroids which indicate the presence of dry S-type bodies in the inner belt and volatile-rich C-type bodies in the outer belt [Gradie and Tedesco, 1982].

2.3 Planets and Planetesimals

As described in section 1.3.3, the growth of planets goes through several phases. First micrometer sized dust particles settle towards the mid plane of the disc and agglomerate into large enough clumps that then grow through pairwise inelastic collisions into rocky bodies or planetesimals up to about 1-10 km in size.

From this point onwards, perturbations in the orbits of planetesimals are dominated by interactions between pairs of solid bodies rather than effects such as collective gravitational effects and gas drag. Planetesimals continue to grow in size through pairwise mergers. Larger planetesimals grow faster since the accretion rate for a body is determined by its size and mass, the surrounding

solids surface density and the relative velocities of its surrounding bodies:

$$\dot{M}_{\mathrm{p}} \simeq \pi R^2 \frac{\Sigma_{\mathrm{p}}}{h} v_p F_{\mathrm{g}} \qquad (2.3)$$

where R is the radius of the body, Σ_{p} is the local solids surface density surrounding the body, h is the disc scale height and v_p is the relative velocity dispersion of the disc [Thommes et al., 2003]. F_{g} is the gravitational focussing factor which relates the effective cross sectional accretion area to the body's physical cross sectional area. This can be written as

$$F_{\mathrm{g}} = 1 + \left(\frac{v_{\mathrm{e}}}{v_{\mathrm{p}}} \right)^2 \qquad (2.4)$$

where v_{e} is the escape velocity from the body's surface and v_{p} is the velocity dispersion in the disc.

Looking at this equation, it is clear that two scenarios for body growth can occur. If $v_{\mathrm{p}} \gtrsim v_e$ then equation 2.4 tends towards 1 giving us a mass accretion rate that is approximately proportional to R^2 so that $\dot{R}$ is independent of R. This type of growth is referred to as *orderly*. If, however, $v_{\mathrm{p}} \ll v_{\mathrm{e}}$ then the mass accretion rate is approximately proportional to R^4 due to the strong dependence on the escape velocity which itself is proportional to R. With such a strong dependence on the radius, larger bodies will grow far faster than their smaller counterparts. This is known as *runaway growth* and the larger bodies that grow out of this regime are known as planetary embryos or *protoplanets*.

2.3.1 Oligarchic Growth

Once a protoplanet becomes large enough, the gravitational interactions between it and other bodies changes from dispersion dominated driven growth - where the relative velocities of local planetesimals are determined mainly by their collective random epicyclic motion - to shear dominated driven growth - where the gravitational interaction with the protoplanet drives the relative velocities of the local planetesimals. Ida and Makino [1993] found that the condition for transferring from a planetesimal-planetesimal driven dispersion dominated growth regime to

a protoplanet-planetesimal driven shear dominated growth regime is

$$2\Sigma_{\mathrm{M}}M > \Sigma_{\mathrm{m}}m \tag{2.5}$$

where M is the protoplanet mass, m is the effective planetesimal mass, Σ_{m} is the local surface density of the planetesimals in the disc and Σ_{M} is the effective surface density of a protoplanet in the disc given by

$$\Sigma_{\mathrm{M}} = \frac{M}{2\pi a \Delta a_{stir}} \tag{2.6}$$

where a_{stir} is the width of the annulus within which the disc is gravitationally stirred by the protoplanet [Thommes et al., 2003].

The dynamical friction between bodies that drives the planetesimal velocity distribution also works to damp down the random motions of the protoplanets so that protoplanets that are relatively close together collide and merge. As a result, protoplanets grow far faster than planetesimals and grow in a runaway fashion, however, the mass doubling of larger protoplanets is slower than smaller embryos. This phase of rapid protoplanet growth is known as *oligarchic growth*.

2.3.2 Isolation Mass

As larger protoplanets grow at a slower rate than smaller protoplanets, this leads to a self limiting regime - the smaller ones will catch up. Growth is slowed due to larger eccentricities meaning that planetesimals have larger relative velocities and thus the effective cross sectional accretion area is reduced. Larger protoplanets thus grow slower from planetesimal accretion than smaller bodies although protoplanet-protoplanet mergers continues until embryos are far enough separated from one another that they are effectively isolated. The result of this is that protoplanets up to about the size of Mars are formed at regularly spaced distances from the central star. The mass that these protoplanets can reach through this runaway accretion phase is the *isolation mass* and is given by

$$M_{\mathrm{iso}} = \frac{(4\pi b R^2 \Sigma_m)^{3/2}}{(3M_{\odot})^{1/2}} \tag{2.7}$$

[Lissauer, 1987]. Here b is a constant defining the separation of protoplanets in multiples of their mutual Hill radius and is approximately 10 [Kokubo and Ida, 1998]. The mutual Hill radius of two planets is given by:

$$R_{\mathrm{h,m}} = \frac{1}{2} \left(\frac{M_1 + M_2}{3M_\odot} \right)^{1/3} (a_1 + a_2).$$

(2.8)

At small semi-major axis, Kepler shear is too great to allow planets of larger than a few Earth masses to form unless the disc mass is significantly boosted above the MMSN. The greater the distance from the central star, the larger the isolation mass can be. This may explain why massive cores can form at large distances from a star leading to giant planet formation beyond the ice line.

2.3.3 Terrestrial and Giant Planets

Oligarchic growth is the process by which terrestrial planets and the cores of giant planets are believed to have been formed. The limit on planet masses due to the isolation mass at small semi-major axis matches well with the observed terrestrial planet region provided that giant impacts can grow planets beyond the isolation mass which is approximately a mars mass in the terrestrial zone [Chambers and Wetherill, 1998].

Furthermore, the epoch of oligarchic growth in the gas giant region (i.e. where Jupiter is now - ~ 5 AU) is on the order of millions of years which matches up well with the observed lifetime of the gas in protoplanetary discs (a few million years) and oligarchic growth can form gas giant cores up to about 10 Earth masses in the same timescale [Thommes et al., 2003]. A giant planet's core has to grow sufficiently before the gas of the disc dissipates in order for there to be enough gas left for envelope accretion. The low hydrogen and helium content in Uranus and Neptune compared to Saturn and Jupiter suggests that their core growth was too slow and that the gas disc had largely dissipated by the time of their gas accretion phases [Lissauer, 1995; Thommes et al., 2003].

2.4 Atmospheric Drag Induced Capture Radii Enhancement

Planets and protoplanets of as low mass as Mars have an escape velocity that is greater than the speed of sound in the gas disc. This means that a tenuous atmosphere begins to be accreted. This atmosphere leads to an increased cross sectional accretion area for a planet due to the gas drag acting on planetesimals that pass through the denser gas which in turn increases the effective capture radius for a planet (see figure 2.1).
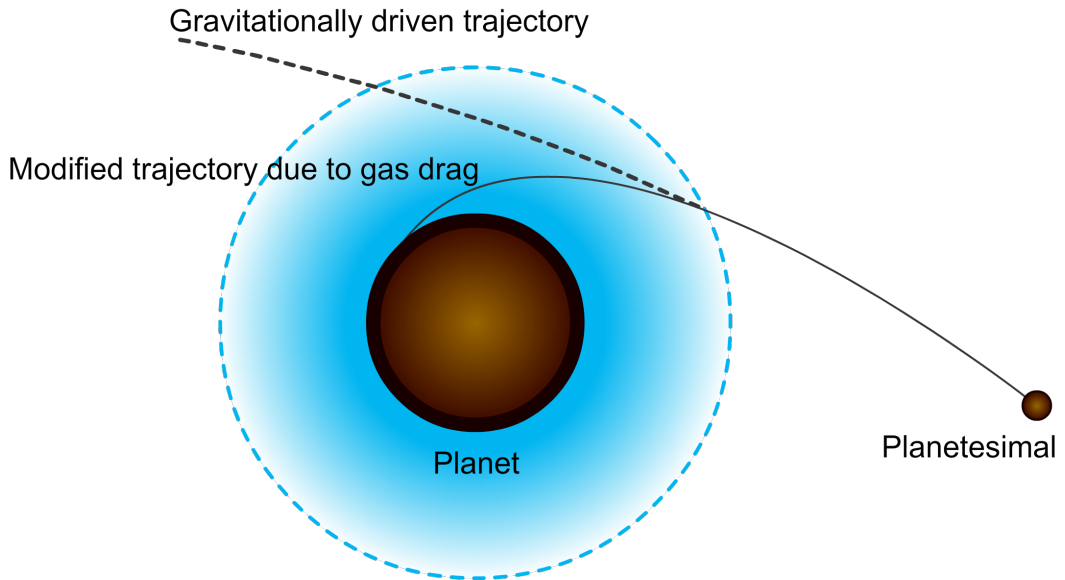
Figure 2.1: The effects of a dense atmosphere on increasing the effective capture radius of a protoplanet.

I use the prescription described in section 2.5 of Inaba and Ikoma [2003] to model this effect (see their Eq. 17 and appendix A). In this model, a planetesimal that is within the Hill sphere of the protoplanet, and located a distance $r_{\rm c}$ from the centre of the protoplanet, will be captured if its physical radius is less than $r_{\rm crit}$ given by the expression

$$r_{\rm crit} = \frac{3}{2} \frac{v_{\rm rel}^2 + 2Gm_{\rm p}/r_{\rm c}}{v_{\rm rel}^2 + 2Gm_{\rm p}/r_{\rm H}} \frac{\rho(r_{\rm c})}{\rho_{\rm p}} r_H. \tag{2.9}$$

Here $\rho(r_c)$ is the local density of the protoplanet atmosphere, ρ_p is the density of the planetesimal, r_H is the protoplanet's Hill radius and v_{rel} is the relative velocity between the two bodies.

The atmosphere model requires us to specify the luminosity of the planet. I assume that this is equal to the gravitational energy released by incoming planetesimals

$$L_p = \frac{G m_p}{r_p} \frac{dm_p}{dt} \tag{2.10}$$

I monitor the accretion rate of solids experienced by protoplanets in my simulations, and use this to determine the accretion luminosity. My simulations use superplanetesimals to model planetesimals due to computational necessity. These superplanetesimals have the physical characteristics of the planetesimals they model but have an increased mass. The accretion of these bodies is very stochastic in nature over the timescale of simulation evolution. Actual planetesimal accretion would be a constant stream of small body accretion. In order to account for this, smooth out the stochastic nature of superplanetesimal accretion, the average luminosity of a protoplanet is calculated over temporal windows of 200 local orbits (or 4000 years, whichever is smaller). The calculated luminosity is limited to within the range 10^{-9} to 10^{-4} L$_\odot$.

The Inaba and Ikoma [2003] model assumes that the contribution to the gravitating mass from the atmosphere is negligible compared to that of the solid core. In order to avoid an overestimation of the capture radius of larger planets, I limit the effective capture radius of a planet to be a maximum of 1/20 of a planet's Hill radius for these planets. The transition is smoothed using the expression

$$\begin{aligned}
r_{capture} = & \left[0.5 - 0.5 \tanh \left(\frac{m_p - 30 M_\oplus}{5 M_\oplus} \right) \right] r_{atmos} \\
& + \left[0.5 + 0.5 \tanh \left(\frac{m_p - 30 M_\oplus}{5 M_\oplus} \right) \right] 0.05 r_H
\end{aligned} \tag{2.11}$$

where $r_{capture}$ is the effective capture radius, r_{atmos} is the enhanced capture radius due to the atmosphere and r_H is the Hill radius. Figure 2.2 shows the effective capture radius as a function of planet mass and luminosity, including the above smoothing procedure.
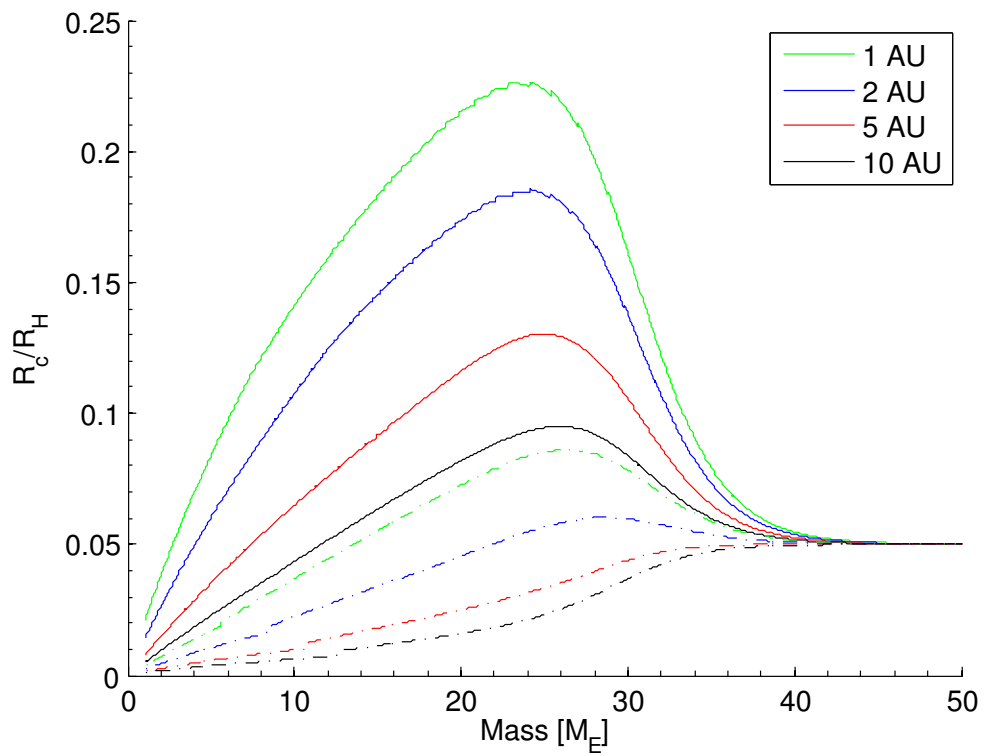
Figure 2.2: Effective planetesimal capture radius enhancement due to atmospheric drag for 10 km planetesimals and with various planet luminosities. Solid lines correspond to $L_{\mathrm{p}} = 10^{-8}$ $L_{\odot}$; dot-dashed lines correspond to $L_{\mathrm{p}} = 10^{-5}$ $L_{\odot}$.

2.5 Planet-Disc Interactions

2.5.1 Aerodynamic drag

The most basic form of planet-disc interactions is aerodynamic or *Stokes drag*. This is a frictional drag force that applies to particles in a fluid. In the application to protoplanetary discs, this provides an efficient source of eccentricity and inclination damping since it damps movement along all axes. It also causes slow and inward drift because planetesimals on Keplerian orbits experience a head-wind from the surrounding sub-Keplerian disc. I apply this effect using the Stokes' drag law [Adachi et al., 1976],

$$\mathbf{F}_{\mathrm{drag}} = m_{\mathrm{p}} \left(\frac{-3\rho C_{\mathrm{D}}}{8\rho_{\mathrm{p}} r_{\mathrm{p}}} \right) v_{\mathrm{rel}} \mathbf{v}_{\mathrm{rel}} \tag{2.12}$$

where ρ is the local gas density, r_{p} is the radius of the body and C_{D} is a dimensionless drag coefficient (here taken to be unity). $\mathbf{v}_{\mathrm{rel}}$ is the velocity of a planetesimal relative to the local gas disc and is defined as:

$$\mathbf{v}_{\mathrm{rel}} = \mathbf{v}_p - \mathbf{v}_{\mathrm{K}} \left(1 - \eta \right) \tag{2.13}$$

where v_{p} is the planetesimal velocity, v_{K} is the local Keplerian velocity, given by

$$v_{\mathrm{K}} = \sqrt{\frac{GM_{\odot}}{R}} \tag{2.14}$$

in the orbital direction and η is the fractional difference between the gas velocity and the local Keplerian velocity due to partial pressure support of the gas disc:

$$\eta = \frac{\pi}{16} \left(\alpha + \beta \right) \left(\frac{c_s}{V_K} \right)^2 . \tag{2.15}$$

Here c_s is the sound speed in the disc and α and β are the surface density and temperature power laws of the gas disc respectively.

2.5.2 Type-I Migration

Although, as has been mentioned in section 2.3, oligarchic growth can lead to the formation of gas giant planet cores, these calculations have considered protoplanets that are affected only by gravitational interactions with other solid bodies in the protoplanetary disc - interactions with the gas in the disc have been ignored.

When planets become massive enough (between a lunar and Mars mass), the gravitational pull they exert on the surrounding gas causes significant density waves to form (see figure 2.3). These are launched at Lindblad resonances both inside and outside the planet in the disc, and lead to an exchange of angular momentum between the planet and the disc gas. Each excited wave exerts a torque on the planet. Torques exerted at Lindblad resonances interior to a planet are positive while those outside a planet are negative. [Tanaka et al., 2002]. Due to asymmetry in the disc caused by the surface density, pressure and disc thickness varying radially, these torques are not equal and the net torque is almost always negative.

The migration timescale for planets undergoing type I migration is [Daisaka et al., 2006]:

$$\tau_{\mathrm{mig}} = 0.23 \left(\frac{M_{\mathrm{p}}}{M_{\odot}} \right)^{-1} \left(\frac{\Sigma_{\mathrm{g}} r^2}{M_{\odot}} \right)^{-1} \left(\frac{c_{\mathrm{s}}}{r\Omega_{\mathrm{p}}} \right)^2 \Omega_{\mathrm{p}}^{-1} \tag{2.16}$$

where Ω is the Keplerian orbital angular velocity:

$$\Omega = \sqrt{\frac{GM_{\odot}}{R^3}} \tag{2.17}$$

Thus the time it takes for a planet to migrate inwards is inversely proportional to a planet's mass. In an MMSN disc, a $0.1 M_{\oplus}$ planet would take about 5 million years to migrate in from $5 AU$ to the central star - longer than the lifetime of the disc. However, a $10 M_{\oplus}$ body, i.e. a reasonably sized gas giant core, would take only 50,000 years - far shorter than the time it would take for Oligarchic growth to form such a body.

The consequence of this rapid inward migration has been a problem in formation models - most larger bodies formed should migrate in and fall onto the central star long before they can form a gap in the disc and undergo type II
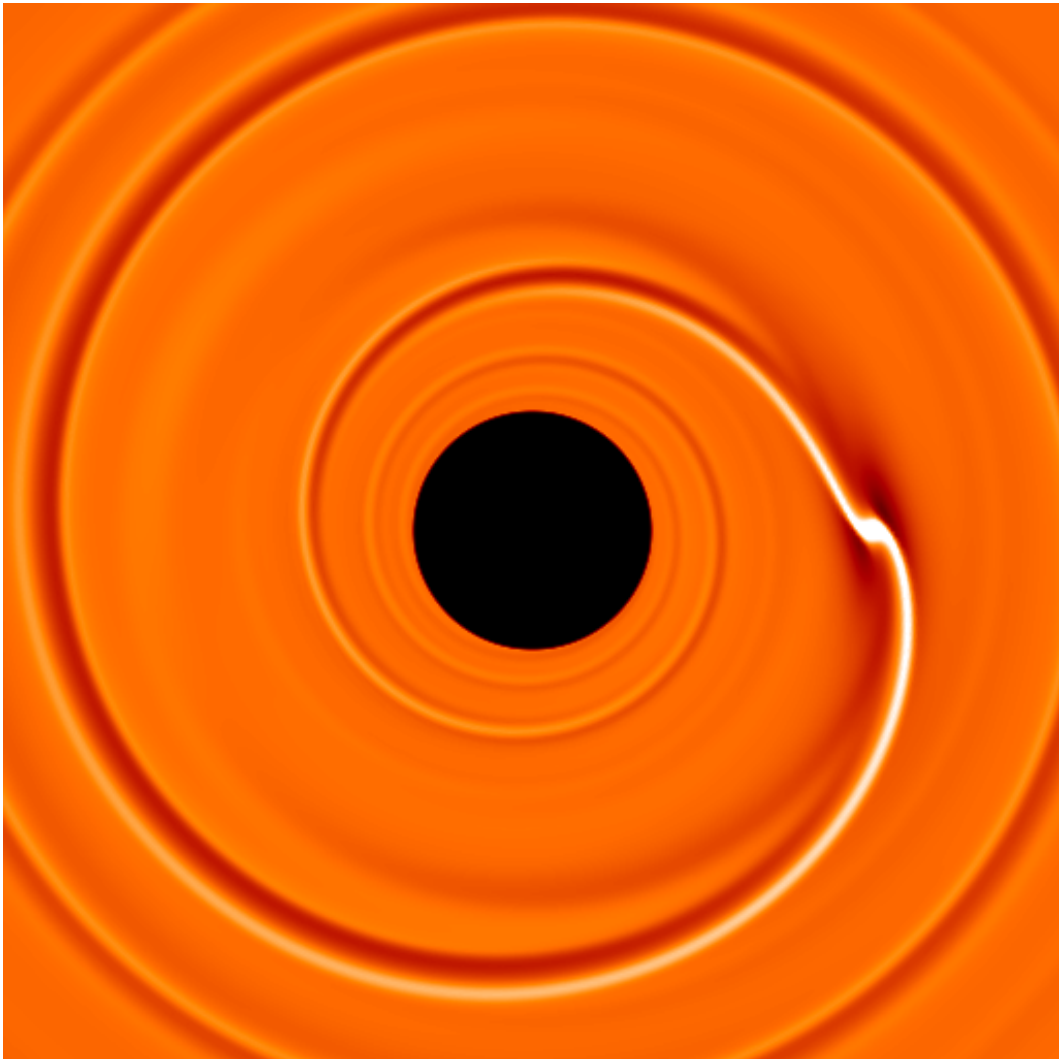
Figure 2.3: Spiral density waves interior and exterior to a planet embedded in a gas disc. [Masset]

migration (see section 3.1.5). It does, however, give a possible explanation as to how hot neptune or super-earth type planets could have formed.

2.5.3 Migration in radiatively-inefficient discs

The migration regimes for medium sized (terrestrial up to sub-gap forming) planets was long treated simply using a linear analysis as it was considered one of the simplest migration cases. Unfortunately, the rapid inward migration that is characteristic of this type I migration leads to a difficulty in reproducing the semi-major axis distribution of observed planets via planetary synthesis models and a reduction of between 10 [Ida and Lin, 2008] and 1000 [Mordasini et al., 2009a] is needed in order to produce results that are in reasonable agreement with extrasolar planet observations.

A modification to the torques that lead to the rapid type I style inward migration is to consider discs that are *non* isothermal in nature. In such models the energy balance is considered in a more realistic manner and it has been shown [Paardekooper and Mellema, 2006] in three dimensional radiation-hydrodynamic simulations that inward migration of low mass planets can not only be slowed down and stopped, migration can also reverse so that planets can move outwards depending on the local disc opacity. This is due to the radial entropy gradient in the disc and the corotation torque [Paardekooper and Mellema, 2008].

In my studies here, I have included the migration of low mass planets by implementing the torque formulae presented by Paardekooper et al. [2010] and Paardekooper et al. [2011]. These formulae describe how the various torque contributions vary as the planet mass and local conditions in the disc change. Specifically, corotation torques depend sensitively on the ratio of the horseshoe libration time scale to either the viscous or thermal diffusion time scales.

There are two basic contributions to the corotation torque: the vorticity-related corotation torque and the entropy-related corotation torque. In an inviscid two dimensional disc, the vortensity (ratio of vorticity to surface density) is a conserved quantity on streamlines. Fluid elements undergoing horseshoe orbits in the presence of a planet therefore conserve this quantity. For power-law surface density profiles with indices greater (less negative) than $-3/2$, there is a nega-
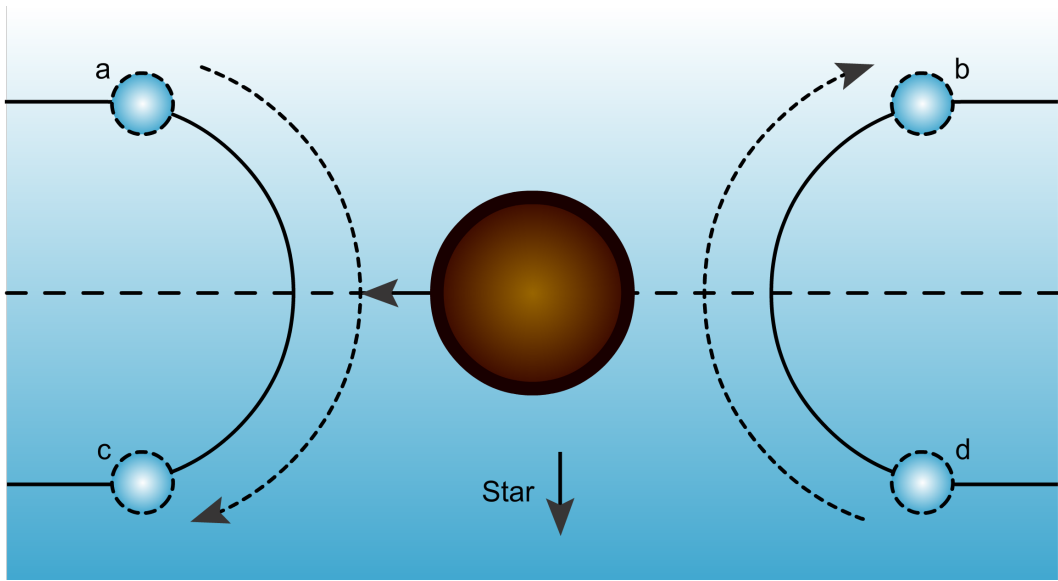
Figure 2.4: Consider a disc with a modest negative surface density gradient. Fluid elements move in horseshoe orbits conserving their vortensity $\sim (\Omega/\Sigma)$. A fluid element beginning outside the planet at (a) undergoes a horseshoe U-turn and moves interior to the planet to (c). In doing so, Ω increases, so Σ must increase also, generating a positive Σ enhancement in front of the planet that exerts a positive torque. The converse is true for fluid elements moving from (d) to (b), leading to a density reduction behind the planet, reinforcing the positive corotation torque. To prevent saturation, the viscous diffusion time across the horseshoe region must be approximately equal to half the horseshoe libration period.
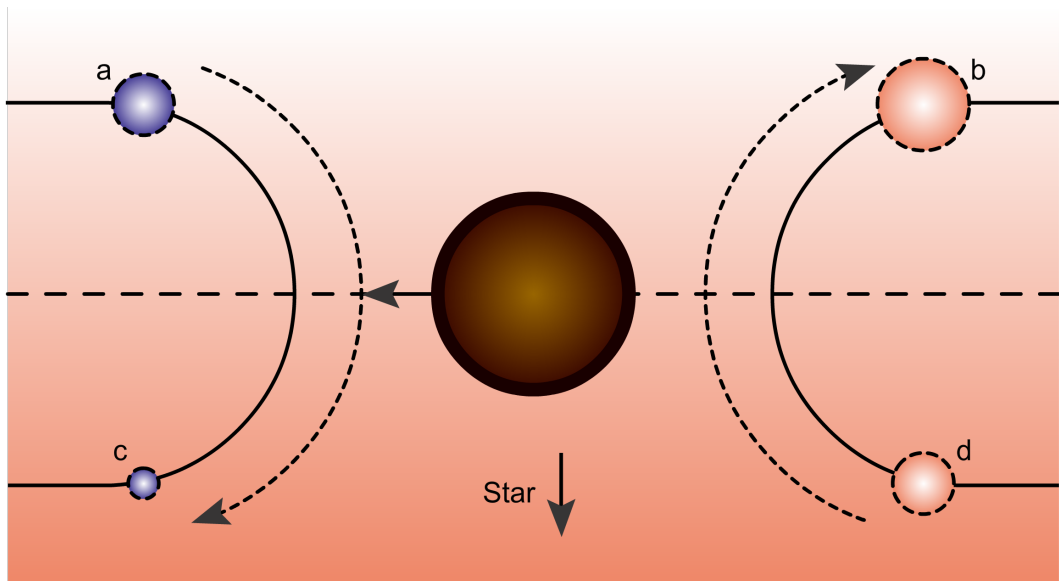
Figure 2.5: A pocket of gas undergoing a horseshoe orbit in a disc with a temperature gradient moves round from a low temperature region (a) to a high temperature region (c). It contracts adiabatically so that when it reaches (d), it has a higher density. Similarly, a pocket of gas at (d) moves around to a lower temperature region (b) where the surrounding gas is cooler and so expands adiabatically leading to a lower density region. If the cooling time is such that by the time a pocket of gas moves from (c) to (d) it will have cooled to the same temperature as the local gas then a positive torque can be sustained. For this to happen, the cooling time has to be the same as half the libration period.

tive radial vortensity gradient, and the exchange of angular momentum between an embedded planet and disc material as the fluid follows horseshoe streamlines generating a positive torque on the planet [Goldreich and Tremaine, 1979]. In the absence of viscous diffusion, material undergoing horseshoe orbits eventually phase mixes because of the varying horseshoe orbit time scales, erasing the vortensity profile in the corotation region and saturating the corotation torque (i.e. switching it off, see figure 2.4). The action of viscous stresses can desaturate the horseshoe torque by maintaining the vortensity gradient across the horseshoe region, and this occurs optimally when the viscous diffusion time scale across the width of the horseshoe region is approximately equal to half the horseshoe libration time. The presence of horseshoe streamlines inevitably means that the associated horseshoe torque is a non linear effect (because horseshoe orbits are not present in a linear theory), usually referred to as horseshoe drag [Masset, 2001; Paardekooper and Papaloizou, 2008; Ward, 1991]. As the viscosity is increased above its optimal value the vortensity on streamlines begins to be modified significantly as the fluid undergoes horseshoe U-turns. For large enough viscosity the vorticity-related corotation torque eventually approaches the smaller value obtained from linear theory [Masset, 2002]. This arises when the viscous diffusion time is shorter than the horseshoe U-turn time.

A similar process occurs for the entropy-related corotation torque (see figure 2.5, but in this case the controlling parameter is the thermal diffusion time scale instead of the viscous one. Optimal corotation torques are obtained when both the thermal and viscous diffusion time scales across the width of the horseshoe region are equal to approximately half the horseshoe libration time. It should be noted that, in addition to thermal diffusion, viscosity is required to desaturate the entropy-related horseshoe torque. This is because material trapped in the horseshoe region in an inviscid disc constitutes a closed system that can only exchange a finite quantity of angular momentum with the planet. Viscosity is required to couple this region with the rest of the disc, such that exchange of angular momentum can desaturate the corotation torque.

For simplicity of implementation, I adopt the approximation suggested by Lyra et al. [2010] and assume that the thermal and viscous time scales in the disc are equal. For a disc in thermodynamic equilibrium, where the heating is

provided by viscous dissipation and local cooling is via blackbody radiation, this is a reasonable assumption to make.

Based on the above discussion, the torque experienced by a low mass planet embedded in a disc depends on the Lindblad torques (originating from the excitation of density waves at Lindblad resonances), and a weighted sum of the vorticity-related horseshoe drag, the entropy-related horseshoe drag, the vorticity-related linear corotation torque, and the entropy-related linear corotation torque. These torque contributions are given as follows:

The Lindblad torque is

$$\Gamma_{\mathrm{LR}} = \left(\frac{\Gamma_0}{\gamma} \right) \left[-2.5 - 1.7\beta + 0.1\alpha \right] \qquad (2.18)$$

the vorticity-related horseshoe drag is

$$\Gamma_{\mathrm{VHS}} = \left(\frac{\Gamma_0}{\gamma} \right) \left[1.1 \left(\frac{3}{2} - \alpha \right) \right] \qquad (2.19)$$

the entropy-related horseshoe drag is

$$\Gamma_{\mathrm{EHS}} = \left(\frac{\Gamma_0}{\gamma} \right) \left[7.9 \frac{\zeta}{\gamma} \right] \qquad (2.20)$$

the vorticity-related linear corotation torque is

$$\Gamma_{\mathrm{LVCT}} = \left(\frac{\Gamma_0}{\gamma} \right) \left[0.7 \left(\frac{3}{2} - \alpha \right) \right] \qquad (2.21)$$

the entropy-related linear corotation torque is

$$\Gamma_{\mathrm{LECT}} = \left(\frac{\Gamma_0}{\gamma} \right) \left[\left(2.2 - \frac{1.4}{\gamma} \right) \zeta \right] \qquad (2.22)$$

In these above expression γ is the ratio of specific heats, α and β are the exponents in the surface density and temperature profiles and ζ is given by

$$\zeta = \beta - (\gamma - 1)\alpha. \qquad (2.23)$$

Γ_0 is given by

$$\Gamma_0 = \left(\frac{m_{\mathrm{p}}}{M_*}\right) \left(\frac{m_{\mathrm{p}}}{\Sigma_{\mathrm{p}} a_{\mathrm{p}}^2}\right) \left(\frac{a_{\mathrm{p}} \Omega_{\mathrm{p}}}{c_s}\right)^2 a_{\mathrm{p}}^2 \Omega_{\mathrm{p}}^2, \tag{2.24}$$

where a_{p} is the planet semimajor axis, and a subscript 'p' denotes that quantities should be evaluated at the orbital location of the planet. In order to obtain the correct total torque as a function of the thermal and viscous diffusion coefficients I combined the above individual torque expressions into the following formula [Paardekooper et al., 2011]:

$$\begin{aligned} \Gamma_{\mathrm{tot}} &= \Gamma_{\mathrm{LR}} + \Gamma_{\mathrm{VHS}} F_{\mathrm{v}} G_{\mathrm{v}} + \Gamma_{\mathrm{EHS}} F_{\mathrm{v}} F_{\mathrm{d}} \sqrt{G_{\mathrm{v}} G_{\mathrm{d}}} \\ &+ \Gamma_{\mathrm{LVCT}} (1 - K_{\mathrm{v}}) + \Gamma_{\mathrm{LECT}} (1 - K_{\mathrm{v}})(1 - K_{\mathrm{d}}) \end{aligned} \tag{2.25}$$

where the functions G_ν, G_{d}, F_{v}, F_{d}, K_{v} and K_{d} are related either to the ratio between the viscous/thermal diffusion time scales and the horseshoe libration time scale, or to the ratio of the viscous/thermal diffusion time scales and the horseshoe U-turn time scale.

The horseshoe libration time is given by $t_{\mathrm{lib}} = 8\pi/(3\Omega_{\mathrm{p}} x_{\mathrm{s}})$, and the viscous diffusion time scale across the horseshoe region is given by $t_{\mathrm{v}} = (x_{\mathrm{s}} a_{\mathrm{p}})^2/\nu$, where ν is the viscous diffusion coefficient. Similarly the thermal diffusion time scale is given by $t_{\mathrm{d}} = (x_{\mathrm{s}} a_{\mathrm{p}})^2/D$, where D is the thermal diffusion coefficient (defined below). Following Paardekooper et al. [2011], I define two parameters that determine the relation between the thermal/diffusion time scales and the horseshoe libration time scale

$$p_{\mathrm{v}} = \frac{2}{3} \sqrt{\frac{a_{\mathrm{p}}^2 \Omega x_{\mathrm{s}}^3}{2\pi\nu}} \equiv \sqrt{\frac{16}{27} \frac{t_{\mathrm{v}}}{t_{\mathrm{lib}}}}, \tag{2.26}$$

which I refer to as the viscous diffusion parameter, and

$$p_{\mathrm{d}} = \sqrt{\frac{a_{\mathrm{p}}^2 \Omega x_{\mathrm{s}}^3}{2\pi D}} \equiv \sqrt{\frac{4}{3} \frac{t_{\mathrm{d}}}{t_{\mathrm{lib}}}}, \tag{2.27}$$

which I refer to as the thermal diffusion parameter. Note that ν and D are assumed to be equal in this thesis, and are complicated functions of radial position in the disc because of the functional form used to define the opacity in equation

([3.8](#)). These diffusion parameters are used to define the following functions

$$F_{\mathrm{v}} = \frac{1}{[1 + (p_{\mathrm{v}}/1.3)^2]} \tag{2.28}$$

$$F_{\mathrm{d}} = \frac{1}{[1 + (p_{\mathrm{d}}/1.3)^2]}. \tag{2.29}$$

Using the viscous diffusion parameter p_{v}, the following functions are defined as

$$G_{\mathrm{v}} = \begin{cases} \frac{16}{25} \left(\frac{45\pi}{8} \right)^{3/4} p_{\mathrm{v}}^{3/2} & \text{if } p_{\mathrm{v}} < \sqrt{8/(45\pi)} \\\\ 1 - \frac{9}{25} \left(\frac{8}{45\pi} \right)^{4/3} p_{\mathrm{v}}^{-8/3} & \text{if } p_{\mathrm{v}} \geq \sqrt{8/(45\pi)} \end{cases} \tag{2.30}$$

$$K_{\mathrm{v}} = \begin{cases} \frac{16}{25} \left(\frac{45\pi}{28} \right)^{3/4} p_{\mathrm{v}}^{3/2} & \text{if } p_{\mathrm{v}} < \sqrt{8/(45\pi)} \\\\ 1 - \frac{9}{25} \left(\frac{28}{45\pi} \right)^{4/3} p_{\mathrm{v}}^{-8/3} & \text{if } p_{\mathrm{v}} \geq \sqrt{28/(45\pi)} \end{cases} \tag{2.31}$$

and using the thermal diffusion parameter p_{d}, the following functions are defined as

$$G_{\mathrm{d}} = \begin{cases} \frac{16}{25} \left(\frac{45\pi}{8} \right)^{3/4} p_{\mathrm{d}}^{3/2} & \text{if } p_{\mathrm{d}} < \sqrt{8/(45\pi)} \\\\ 1 - \frac{9}{25} \left(\frac{8}{45\pi} \right)^{4/3} p_{\mathrm{d}}^{-8/3} & \text{if } p_{\mathrm{d}} \geq \sqrt{8/(45\pi)} \end{cases} \tag{2.32}$$

$$K_{\mathrm{d}} = \begin{cases} \frac{16}{25} \left(\frac{45\pi}{28} \right)^{3/4} p_{\mathrm{d}}^{3/2} & \text{if } p_{\mathrm{d}} < \sqrt{28/(45\pi)} \\\\ 1 - \frac{9}{25} \left(\frac{28}{45\pi} \right)^{4/3} p_{\mathrm{d}}^{-8/3} & \text{if } p_{\mathrm{d}} \geq \sqrt{28/(45\pi)} \end{cases} \tag{2.33}$$

according to [Paardekooper et al., 2011].

2.5.3.1 Thermal and viscous diffusion

Radiative diffusion in the disc causes the thermal energy per unit volume, e, to evolve according to

$$\frac{\partial e}{\partial t} = -\nabla.\mathbf{F} \tag{2.34}$$

36

where the radiative flux in the radial direction (across the horseshoe region) may be expressed as

$$F_{\rm r} = -\frac{4a_{\rm r}c}{3}\frac{T^3}{\kappa\rho}\frac{dT}{dr}.$$
(2.35)

Here $a_{\rm r}$ is the radiation constant and c is the speed of light. Noting that $e = P/(\gamma-1)$ and $P = k_{\rm B}\rho T/(\mu m_{\rm H})$, and assuming that ρ is locally constant, I obtain the diffusion equation governing temperature evolution

$$\frac{\partial T}{\partial t} = \nabla_{\rm r}\left(D\frac{dT}{dr}\right)$$
(2.36)

where the diffusion coefficient, D, is given by

$$D = \frac{4a_{\rm r}c}{3}\frac{T^3}{\kappa\rho^2}\frac{(\gamma-1)\mu m_{\rm H}}{k_{\rm B}}.$$
(2.37)

where μ is the mean molecular weight of the gas and $m_{\rm H}$ is the mass of a hydrogen atom. Only $\frac{dT}{dr}$ remains in equation 2.36 as I assume the disc is isothermal in the vertical direction and is axisymmetric. I set the viscous diffusion coefficient equal to the thermal diffusion coefficient for the purpose of determining the level of saturation of corotation torques ($\nu = D$).

2.6   Type II migration

Protoplanets accrete a gas envelope gradually until their gas content is comparable in mass to that of their solid material. After this switchover, the rate of gas accretion accelerates rapidly in a runaway regime [Pollack et al., 1996]. This regime lasts only a few thousand years and continues until the planet has cut off its supply of gas by forming a gap in the disc [Lin and Papaloizou, 1979]. At this point, the planet can still accrete gas albeit at a far slower rate which is dependent on the viscous disc's ability to supply material to the planet.

Initial estimates put the time it would have taken for a Jupiter-like body to form in a 3 times MMSN nebula were about 8 MYr [Pollack et al., 1996]. Further refinements to the model lead to timescales of about 3 MYr [Lissauer et al., 2009] and recent improvements have reduced the time to as short as 1 MYr for a 3

times MMSN disc [Movshovitz et al., 2010].

In my studies here, I use methods based around the Movshovitz et al. [2010] model. The methods used are described in sections 3.1.6 and 4.2.2.

Chapter 3

N-body Models for Planet Formation

3.1 Model Description

3.1.1 Disc parameters

To limit the parameter space covered by the simulations, I considered only disc models that can provide outward migration when unsaturated corotation torques are included (see figure 3.1). The conditions under which outward migration occurs are discussed in later sections, but as a rule of thumb I find that the temperature radial power-law index, β, must be approximately 0.25 larger than the surface density power-law index, α.

3.1.1.1 Gas disc component

The initial gas surface density is given by the power-law expression

$$\Sigma_g(R) = \Sigma_g \left(1\,\text{AU}\right) \left(\frac{R}{1\,\text{AU}}\right)^{-\alpha}. \tag{3.1}$$

The volume density of gas is then

$$\rho(R,z) = \frac{\Sigma(R,t)}{\sqrt{2\pi}H} \exp\left(-z^2/2H^2\right) \tag{3.2}$$

39
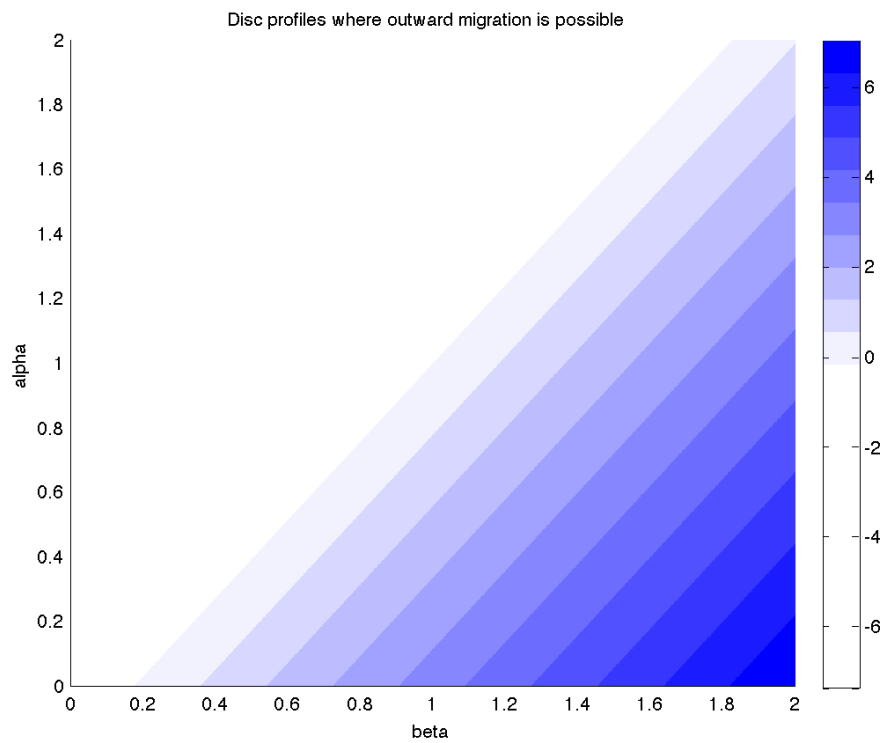
Figure 3.1: Disc profiles where outward migration is possible plotted against disc surface density exponent (alpha) and disc temperature exponent (beta). Regions shaded blue correspond to parameters for which outward migration is possible. Dark blue regions correspond to parameters for which strong outward migration is possible whereas for light shades, outward migration is weak.

where H is the local disc scale height. The disc temperature is also given by a power-law function of radius

$$T(R) = T(1\,\text{AU}) \left(\frac{R}{1\,\text{AU}} \right)^{-\beta} \qquad (3.3)$$

where $T(1\,\text{AU})$ is taken to be 280 K.

A disc with power-law density and temperature profiles also has a power-law entropy profile. The associated power-law index is given by

$$\zeta = (\alpha + \beta) - \alpha\gamma \qquad (3.4)$$

where γ is the usual ratio of specific heats, here taken to be $\gamma = 7/5$. The isothermal sound speed is

$$c_{\text{s}} = \sqrt{\frac{k_{\text{B}}T}{m_{\text{H}}\mu}} \qquad (3.5)$$

where k_{B} is the Boltzmann constant, m_{H} is the mass of a hydrogen atom and μ is the mean molecular weight (here assumed to equal 2.4). The disc scale height is given by

$$H = c_{\text{s}}\Omega_{\text{K}} \qquad (3.6)$$

where Ω_{K} is the Keplerian angular velocity. The angular velocity of the gas is given by

$$\Omega(R) = \Omega_{\text{K}}(R) \left[1 - (\alpha + \beta) \left(\frac{H}{R} \right)^2 \right]. \qquad (3.7)$$

3.1.1.2 Opacities

I take the opacity κ to be always equal to the Rosseland mean opacity, and I take the temperature and density dependence to be given by the formulae of Bell

et al. [1997] below 3730 K and by Bell and Lin [1994] above this value:

$$\kappa[\text{cm}^2/\text{g}] = \begin{cases} 10^{-4}\,T^{2.1} & T < 132\,\text{K} \\ 3\,T^{-0.01} & 132\,\text{K} \leq T < 170\,\text{K} \\ 10^{-2}\,T^{1.1} & 170\,\text{K} \leq T < 375\,\text{K} \\ 5\times 10^4\,T^{-1.5} & 375\,\text{K} \leq T < 390\,\text{K} \\ 0.1\,T^{0.7} & 390\,\text{K} \leq T < 580\,\text{K} \\ 2\times 10^{15}\,T^{-5.2} & 580\,\text{K} \leq T < 680\,\text{K} \\ 0.02\,T^{0.8} & 680\,\text{K} \leq T < 960\,\text{K} \\ 2\times 10^{81}\,\rho\,T^{-24} & 960\,\text{K} \leq T < 1570\,\text{K} \\ 10^{-8}\,\rho^{2/3}\,T^3 & 1570\,\text{K} \leq T < 3730\,\text{K} \\ 10^{-36}\,\rho^{1/3}\,T^{10} & 3730\,\text{K} \leq T < 10000\,\text{K} \end{cases} \tag{3.8}$$

3.1.1.3   Disc solid component

The disc solid component is composed initially of protoplanets and planetesimals (that I model as a computationally feasible number of 'superplanetesimals' of much larger mass than real planetesimals, but with an assumed radius equal to that of realistic planetesimals (10 km) such that they experience the appropriate gas drag force).

Protoplanets are initially spaced by 10 mutual Hill radii, and planetesimals are scattered throughout the disc such that the total solids content follows the surface density power-law prescribed for the gaseous component. As in Thommes et al. [2003], planetesimal eccentricities and inclinations are distributed according to a Rayleigh distribution and have RMS values of the eccentricity $e = 0.01$ and inclination $i = 0.005$ radians, respectively. The surface density of solids is enhanced beyond the snow line, whose position R_{snow} is determined by the location where the temperature falls below 170 K. The snow line discontinuity is

spread over a distance ~ 1 AU:

$$\Sigma_{\mathrm{s,0}}(R) = \left\{ \Sigma_1 + (\Sigma_2 - \Sigma_1) \left[\frac{1}{2}\left(\frac{R - R_{\mathrm{snow}}}{0.5\,\mathrm{AU}} \right) + \frac{1}{2} \right] \right\} \left(\frac{R}{1\,\mathrm{AU}} \right)^{-\alpha} \tag{3.9}$$

The surface density enhancement due to the snowline is $(\Sigma_2/\Sigma_1) = 30/7.1$ as in Thommes et al. [2003]. Planetesimal densities are set at 3 g/cm^3 throughout the disk. Protoplanet densities are set at 3 g/cm^3 inside the snowline and 1.5 g/cm^3 beyond, as defined by Thommes et al. [2003]. The mass of the protoplanets at $t = 0$ is $M_{\mathrm{p}} = 0.2$ M$_\oplus$, and the mass of the superplanetesimals is 0.04 M$_\oplus$.

3.1.2 Disc evolution

The dispersal of the gas disc is simply modelled by modifying 3.1 so as to include a decay term that mimics the dispersal of the gas disc by viscous evolution and photoevaporation on a timescale defined by τ_{disc}:

$$\Sigma_{\mathrm{g}}(R, t) = \Sigma_{\mathrm{g}}\,(1\,\mathrm{AU}) \left(\frac{R}{1\,\mathrm{AU}} \right)^{-\alpha} \exp\left(-t/\tau_{\mathrm{disc}}\right) \tag{3.10}$$

In this investigation, τ_{disc} is taken to be 1 Myr.

3.1.3 Planetary Migration

3.1.3.1 Eccentricity reduction factor

I follow the planetary migration model as defined in 2.5.3, however, I use a slight modification of the torque expression 2.26:

$$\begin{aligned}
\Gamma_{\mathrm{tot}} &= \Gamma_{\mathrm{LR}} + \Big\{ \Gamma_{\mathrm{VHS}} F_{\mathrm{v}} G_{\mathrm{v}} + \Gamma_{\mathrm{EHS}} F_{\mathrm{v}} F_{\mathrm{d}} \sqrt{G_{\mathrm{v}} G_{\mathrm{d}}} \\
&+ \Gamma_{\mathrm{LVCT}}(1 - K_{\mathrm{v}}) + \Gamma_{\mathrm{LECT}}(1 - K_{\mathrm{v}})(1 - K_{\mathrm{d}}) \Big\} E
\end{aligned} \tag{3.11}$$

The factor E, that multiplies all terms that can contribute to the corotation torque, allows for the fact that corotation torques may be strongly attenuated when the planet has a finite eccentricity, such that it undergoes radial excursions

that are larger than the width of the horseshoe region [Bitsch and Kley, 2010]. To account for this effect I define E according to

$$E = (1 - \tanh(e/x_{\rm s})) \tag{3.12}$$

where the dimensionless horseshoe width is given by

$$x_{\rm s} = \frac{1.1}{\gamma^{1/4}} \sqrt{\frac{q}{h}}, \tag{3.13}$$

$q = M_{\rm p}/M_*$ and $h = H/R$. The physical horseshoe width can be obtained by multiplying x_s by a planet's Hill radius, $r_{\rm H}$. Note that for most simulations I set $E = 1$, but for a subsample of my runs (labelled as 'E') I use equation (3.12) to define E.

3.1.4 Eccentricity and Inclination damping

To damp the inclinations of protoplanets I used the prescription given in Appendix A of Daisaka et al. [2006]:

$$F_{\rm idamp,z} = M_{\rm p} \left(\frac{M_{\rm p}}{M_\odot} \right) \left(\frac{a_{\rm p}\Omega_{\rm p}}{c_s} \right)^4 \left(\frac{\Sigma_{\rm g} a_{\rm p}^2}{M_\odot} \right) \Omega_{\rm p} \left(2A_{\rm z}^c v_{\rm z} + A_{\rm z}^s z\Omega_{\rm p} \right) \tag{3.14}$$

where $A_z^c = -1.088$ and $A_z^s = -0.871$.

In addition to experiencing migration through interaction with the gas disc, protoplanets also undergo eccentricity and inclination damping. To damp eccentricities I used a simple time scale damping formula given by

$$F_{\rm edamp,r} = -\frac{v_{\rm r}}{t_{\rm edamp}}, \quad F_{\rm edamp,\theta} = -\frac{0.5 \left(v_\theta - v_{\rm K} \right)}{t_{\rm edamp}} \tag{3.15}$$

where

$$t_{\rm edamp} = \left(\frac{M_{\rm p}}{M_\odot} \right)^{-1} \left(\frac{a_{\rm p}\Omega_{\rm p}}{c_s} \right)^{-4} \left(\frac{\Sigma_{\rm g} a_{\rm p}^2}{M_\odot} \right)^{-1} \Omega_{\rm p}^{-1} \tag{3.16}$$

I adopted this prescription rather than using the eccentricity damping forces prescribed in Daisaka et al. [2006] because I found that the latter could generate significant jitter in the acceleration experienced by the planets in disc models

with strong radial temperature gradients, where H/r becomes small near the disc outer edge. The formula based on the time scale argument produced smoother results, apparently because it is based on an orbit-averaging procedure rather than capturing the instantaneous force experienced by a planet around its orbit.

3.1.5 Type II-Migration

For massive planets, the migration changes from being of type I to being of type II as gap formation occurs. Under these circumstances the planet migrates inward on a time scale equal to the local viscous evolution time, τ_ν, provided that the planet mass is smaller than the disc mass interior to the planet. For more massive planets the migration slows down due to the inertia of the planet (and is ultimately determined by the time over which the viscous flow in the disc delivers a mass of gas comparable to that of the planet to the planet orbital radius [Ivanov et al., 1999; Syer and Clarke, 1995]).

The viscous evolution time is $\tau_\nu = R^2/(3\nu)$, where I use equation 3.27 to calculate ν, and I apply the following torque in the type II migration regime

$$\Gamma_{\text{II}} = -\frac{M_{\text{p}} j_{\text{p}}}{\tau_\nu} \left(1 + \frac{M_{\text{p}}}{\pi a_{\text{p}}^2 \Sigma_{\text{p}}} \right)^{-1} \tag{3.17}$$

where M_{p} is the planet mass, j_{p} is the specific angular momentum, a_{p} is the planet semimajor axis and Σ_{p} is the disc surface density at the planet's semimajor axis location. I transition smoothly between the type I and type II migration regimes using the following expression

$$\Gamma_{\text{eff}} = \Gamma_{\text{II}} B + \Gamma_{\text{I}} (1 - B) \tag{3.18}$$

where Γ_{eff} is the torque applied during the transition, Γ_{I} is the type I torque, and the transition function B is given by

$$B = 0.5 + 0.5 \tanh \left(\frac{M_{\text{p}} - 65 M_\oplus}{15 M_\oplus} \right). \tag{3.19}$$

I adopted this form for B so as to allow the transition to type II migration to

begin for $M_{\mathrm{p}} = 30\mathrm{M}_{\oplus}$, and for the transition to be complete for planets with mass $M_{\mathrm{p}} = 100\mathrm{M}_{\oplus}$, in broad agreement with the results from analytic considerations [Ward, 1997] and numerical simulations [D'Angelo et al., 2003]. In the type II regime, eccentricities and inclinations are damped on a time scale equal to $\tau_\nu/10$.

3.1.6 Gas Accretion Model

As protoplanets grow through mutual collision and planetesimal accretion they are able to accrete a gaseous envelope from the surrounding disc, and may eventually become gas giant planets. To model gaseous envelope accretion, I have implemented a very approximate scheme by calculating fits to the results of 1D giant planet formation calculations presented by Movshovitz et al. [2010]. Working in time units of Myr and mass units of Earth masses, the gas accretion rate is given by

$$\frac{dm_{\mathrm{ge}}}{dt} = 5.5 \left(\frac{1}{\tau_{\mathrm{ge}} - \tau_{\mathrm{ge0}}} \right) \tag{3.20}$$

where I define τ_{ge} by the expression

$$\tau_{\mathrm{ge}} = 9.665 M_{\mathrm{core}}^{-1.2}, \tag{3.21}$$

and τ_{ge0} is given by the expression

$$\tau_{\mathrm{ge0}} = \tau_{\mathrm{ge}} \left(1 - \left(\frac{1}{\exp\left(\frac{m_{\mathrm{ge}}}{5.5} \right)} \right) \right). \tag{3.22}$$

This procedure allows the planet core to grow due to accretion of solids after envelope accretion has commenced, and allows the rate of envelope accretion to adjust to the changing core mass. It is well known from the studies of Pollack et al. [1996] and others that the rate of gas envelope accretion is a sensitive function of the core mass, increasing as the core mass increases. Figure 3.2 shows the gas envelope mass evolution in the absence of planetesimal accretion and migration for planets with fixed core mass. These are very similar to the results of detailed 1D giant planet formation calculations displayed in figure 1 of Movshovitz et al. [2010]. Although I have implemented the above equations for
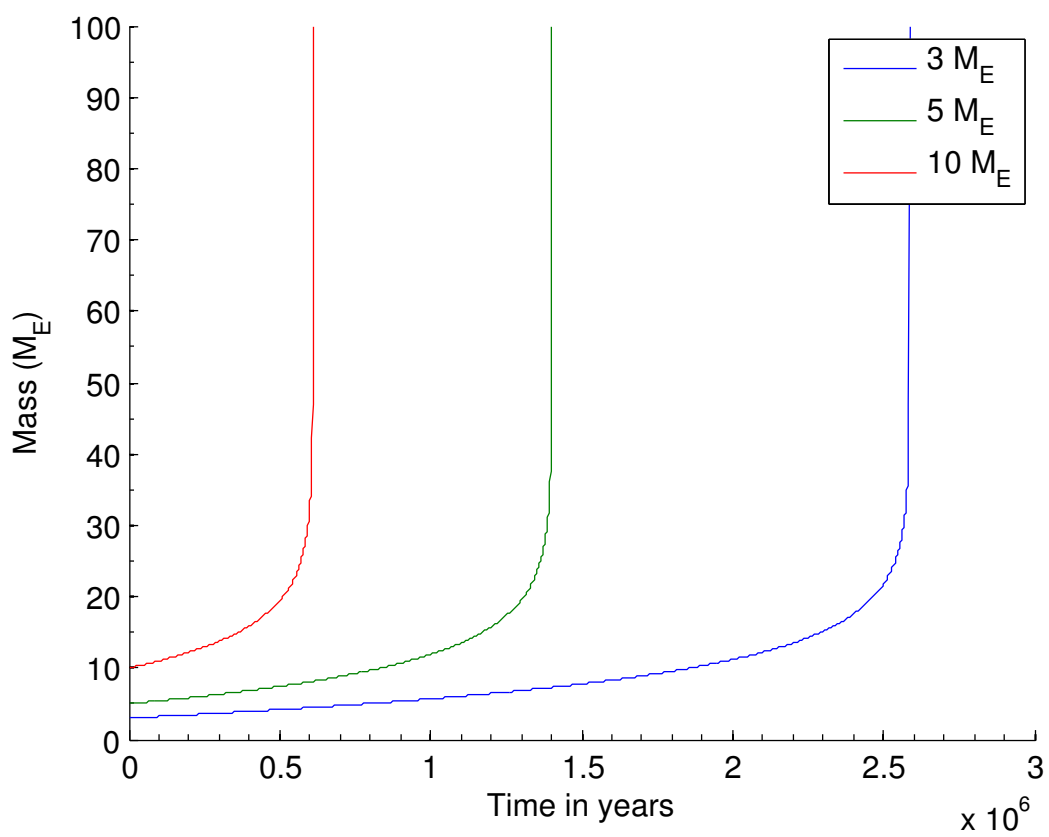
Figure 3.2: Gas accretion onto giant planet cores for 3, 5 and 10 $M_\oplus$ cores against time at 5 AU in a disc with no migration or planetesimal accretion.

gas accretion numerically, I note that they have the analytic solution

$$m_{\text{ge}}(t) = -5.5 \ln \left(1 - \frac{m_{\text{core}}^{1.2}}{9.665} t \right). \tag{3.23}$$

Ideally, I would like to incorporate full 1D models of giant planet formation in my N-body simulations, such that the gas envelope accretion can respond to the changing planetesimal accretion rate and changing conditions in the disc, but such an approach is computationally prohibitive at present. This simplified approach is highly efficient and provides a reasonably good approximation to detailed core nucleated accretion models, enabling me to add a vital missing component to my N-body simulations.

The amount of gas that can accrete rapidly onto a forming giant planet is constrained by the availability of gas in the local feeding zone. Thus I allow giant planets to accrete gas using the procedure described above until the envelope mass approaches the isolation mass, defined to be the gas mass in the feeding zone. I approximate the feeding zone width to be [Lissauer, 1993]

$$r_{\text{c}} = 2\sqrt{3} r_{\text{H}} \tag{3.24}$$

leading to the following expression for the gas isolation mass of the planet

$$m_{\text{g}-\text{iso}} = \int_{a-2\sqrt{3}r_{\text{H}}}^{a+2\sqrt{3}r_{\text{H}}} 2\pi \Sigma_{\text{g}} R \, dR. \tag{3.25}$$

During the growth of the planet, it can begin to open a gap through nonlinear tidal interaction with the disc [Lin and Papaloizou, 1986] and for typical disc parameters this occurs around a Jovian mass [Bryden et al., 1999; Kley, 1999; Nelson et al., 2000]. Consequently, if the isolation mass exceeds the Jovian mass, I limit the mass of the planet that can be obtained during runaway gas accretion to be the Jovian mass.

Once the runaway cut-off mass has been reached, the gas accretion rate switches to the approximate rate that viscosity can supply mass to the planet from the gas disc,

$$\frac{dm_{\text{ge}}}{dt} = 3\pi \nu \Sigma_{\text{g}} \tag{3.26}$$

where ν is the local disc viscosity given by

$$\nu = \alpha_{\mathrm{v}} H^2 \Omega(R) \qquad (3.27)$$

where α_{v} is the viscous parameter (set to 10^{-3} for the purpose of this calculation). Note that this value for the kinematic viscosity is not the same as that obtained by assuming the thermal and viscous diffusion coefficients are equal, as is done to determine the magnitude of the corotation torques acting on a planet (see section 2.5.3). However, the value of α_{v} adopted for the purpose of determining the viscously-driven mass accretion rate is similar to that used in many previous studies of disc-planet interactions [Bryden et al., 1999; Kley, 1999; Nelson et al., 2000], and produces viscous accretion rates within the range observed to occur onto T Tauri stars [Sicilia-Aguilar et al., 2004].

3.2 Initial Conditions

My simulations were performed using the Mercury-6 symplectic integrator [Chambers, 1999], modified to include the physics described in chapter 2 and section 3.1.

In order to model feasibly multiple parameter sets over time scales of 3 Myr, my planetesimal disc consists of super-planetesimals (0.004 $M_{\oplus}$) with effective radius of 10km, representing the averaged orbits of a much larger number of real planetesimals. I set the mass of my protoplanets to be a factor of 5 larger than the planetesimals, giving run times of approximately three cpu weeks for each simulation.

To enable broad coverage of the α and β parameter set, I limited the number of realisations of initial conditions to two runs for each parameter choice, with each member of the pair differing only by the random number seed used to determine initial positions of the planetesimals. My initial suite of simulations included models with enhancements by factors of 3 and 5 above the mass of the MMSN (models labelled 'M'), but I later augmented these with additional models with mass enhancement factors equal to 1 and 2 (models labelled 'R'). I also examined two models where I implemented a reduction in the corotation torques

for protoplanets that develop eccentric orbits (discussed in detail in Sect.3.1.4). These models are labelled 'E'. Test calculations examining the influence of the planetesimal capture radii of protoplanets were also performed.

In order to ensure that the disc mass is locally comparable in models with different surface density profiles, I normalise the disc masses so that they all have the same mass in the region from 2-15 AU that the enhanced MMSN discs would have. This resulted in there being 28 protoplanets, with $\sim$ 4200 and $\sim$ 2500 planetesimals, for mass enhancement factors of 5 and 3, respectively. I limited my selection of the α and β parameter space to models for which outward migration due to corotation torques is possible (the conditions for this can be determined by requiring the entropy-related and vorticity-related horseshoe drag terms in section 2.5.3 to exceed the Lindblad torques). My simulation parameters are detailed in table 3.1.

I set an inner edge to my simulations at 1 AU, and any body that migrates inside this boundary, such that its semimajor axis is less than 1 AU, is removed from the simulation. This radius was chosen to allow for a feasible time step size in the n-body integrations. Information, however, is stored about each body as it crosses this boundary, allowing us to follow the longer term trajectories of individual planets to determine their final stopping location as the gas disc disperses. This procedure is referred to as 'single-body analysis' later in section 3.3.3.1.

3.3   Results

In this section I begin by describing common behaviour seen in many of the simulations. I introduce and discuss the concept of zero-migration lines, and their role in creating convergent migration within a swarm of growing protoplanets. I also discuss the coupling between the mass growth of protoplanets and their migration, and how rapid accretion by protoplanets can lead to migration into the central star.

I then describe the detailed evolution of a selection of individual runs (four runs in total), followed by a summary of results across all of the simulations. This includes the results of single body analysis, where I investigate the evolution of

Table 3.1: Simulation parameters.

Simulation	f_{enh}	α	β	M_{solid}	a_{snow}
M01A, M01B	5	0.5	0.75	173	1.95
M02A, M02B	3	0.5	0.75	104	1.95
M03A, M03B	5	0.5	1	173	1.65
M04A, M04B	3	0.5	1	104	1.65
M05A, M05B	5	0.5	1.25	173	1.49
M06A, M06B	3	0.5	1.25	104	1.49
M07A, M07B	5	0.5	1.5	173	1.39
M08A, M08B	3	0.5	1.5	104	1.39
M09A, M09B	5	0.75	1	173	1.65
M10A, M10B	3	0.75	1	104	1.65
M11A, M11B	5	0.75	1.25	173	1.49
M12A, M12B	3	0.75	1.25	104	1.49
M13A, M13B	5	0.75	1.5	174	1.39
M14A, M14B	3	0.75	1.5	104	1.39
M15A, M15B	5	1	1.25	170	1.49
M16A, M16B	3	1	1.25	107	1.49
M17A, M17B	5	1	1.5	170	1.39
M18A, M18B	3	1	1.5	107	1.39
M19A, M19B	5	1.25	1.5	173	1.39
M20A, M20B	3	1.25	1.5	104	1.39
R01A, R01B	2	0.5	1.25	69.6	1.49
R02A, R02B	1	0.5	1.25	36.6	1.49
R03A, R03B	2	0.5	1.5	69.6	1.39
R04A, R04B	1	0.5	1.5	36.6	1.39
R05A, R05B	2	0.75	1.25	69.6	1.49
R06A, R06B	1	0.75	1.25	36.1	1.49
R07A, R07B	2	0.75	1.5	69.6	1.39
R08A, R08B	1	0.75	1.5	36.1	1.39
E01A, E01B	5	0.5	1.25	173	1.49
E02A, E02B	3	0.5	1.25	104	1.49

bodies lost beyond the inner edge of the simulations (these are treated as isolated bodies, and so the analysis is limited in its ability to provide accurate predictions about the nature of short-period systems).

Finally, I discuss briefly the effects of protoplanet eccentricity on the collective evolution of the system, and present results in which the strength of corotation torques is attenuated when a planet's eccentric orbit induces a radial excursion that is larger than the horseshoe width.

Throughout this section, I define a gas giant as being a planet that has undergone runaway gas accretion, i.e. the sharp increase in mass shown in figure 3.2. This corresponds to a mass of approximately 30 $M_\oplus$.

3.3.1 Common behaviour

3.3.1.1 Migration lines

Consider a planet orbiting in a protoplanetary disc with power-law surface density and temperature profiles. If the planet sits in the inner regions of the disc with high surface density and opacity, such that the horseshoe libration time is significantly *shorter* than the thermal/viscous diffusion time across the horseshoe region, then the corotation torques will saturate and be inoperable. The planet will migrate inward rapidly as its evolution will be determined by Lindblad torques.

Consider the same planet orbiting much further out in the disc where the surface density and opacity are substantially reduced, such that the horseshoe libration time is much *longer* than the thermal/viscous diffusion time. The disc-planet system is now close to the locally isothermal limit, such that corotation torques will be close to their linear value (see section 2.5.3). The migration will again be inward because of the dominance of the Lindblad torques, but at a reduced rate because of the contribution of positive corotation torques.

There exists an intermediate radial location in the disc where the surface density and opacity allow the thermal/viscous diffusion time to be approximately equal to the horseshoe libration time. The corotation torque (horseshoe drag) will be close to its maximum value here, and will possibly drive strong outward migration of the planet if the entropy gradient in the disc is steep enough. As

the planet migrates outward, however, the local disc surface density and opacity decrease, decreasing the thermal diffusion time, and reducing the efficacy of the positive corotation torque. Eventually the planet reaches a location where the corotation and Lindblad torques exactly cancel, such that the planet stops migrating. I refer to this location as the zero-migration line, and these are stable positions in the disc for planets to reside.

Given that the horseshoe libration time is shorter for more massive planets, the zero-migration lines of heavier planets are located further out in the disc where the thermal diffusion times are shorter. Heavier planets that form in inner disc regions will need to migrate out past lower mass bodies to reach their zero-migration lines, leading to convergent migration for protoplanets with different masses. Such planets can shepherd smaller planets, accrete them or scatter them depending on the conditions in the disc and the rate of migration. Furthermore, protoplanets with the same mass try to migrate to the same location in the disc. In principle, this should increase the rate of collisional planetary growth.

The behaviour described above is illustrated in the contour plots shown in figure 3.3, which display the value of the total torque in units of Γ_0/γ (defined in equation 2.24), as a function of planetary mass and orbital position. The four panels correspond to the initial models M05A, M16A, M03B and M07B that are described in Table 3.2. Regions coloured red correspond to strong inward migration (migration dominated by Lindblad torques). Regions coloured dark blue correspond to strong outward migration, and lightly coloured regions correspond to slow or zero migration. In general, rapid outward migration is favoured in discs with relatively flat surface density profiles and steep temperature profiles.

In a steady-state disc, a planet of fixed mass that migrates to its zero-migration line should stay there. Disc dispersal, however, leads to a locally reducing surface density and opacity, progressively shifting the zero-migration line inward. Consequently, as the disc disperses, a planet sitting on a zero-migration line drifts inward on the gas disc dispersal time scale. This behaviour is shown in figures 3.4 and 3.5, which show the migration trajectories of planets of different mass in the two disc models M05A and M03B that are dispersing on time scales of 1 Myr (similar migration trajectories are shown in Lyra et al. [2010]). Planets of a given mass starting at different locations tend to migrate outward and eventu-
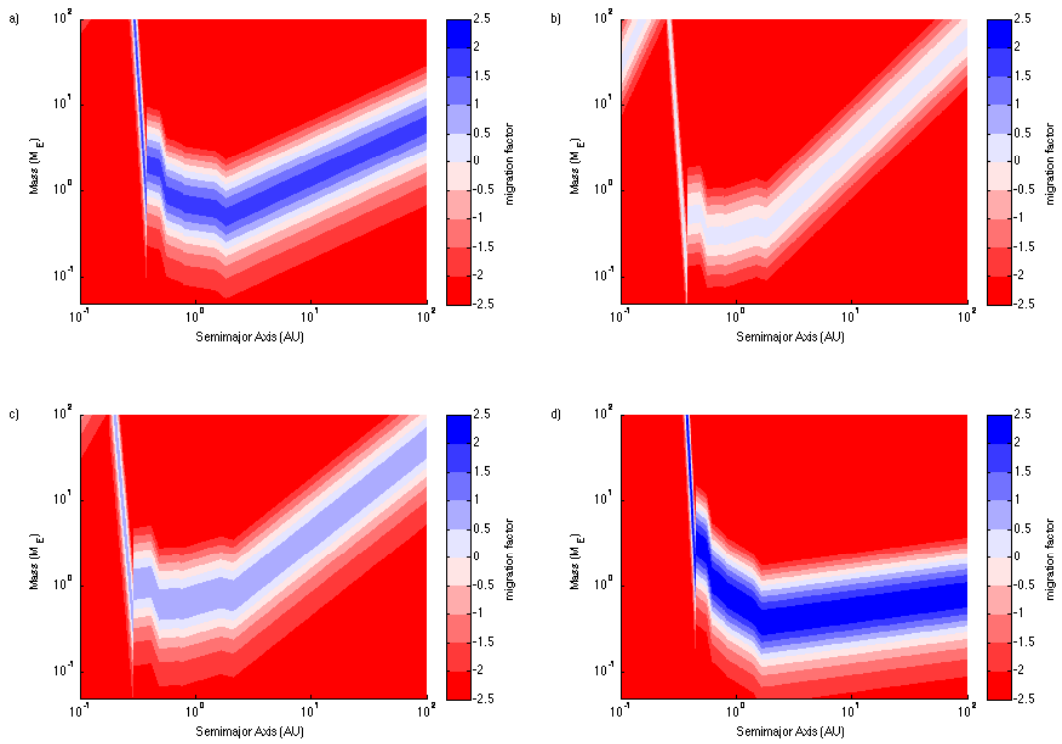
Figure 3.3: Contour plots showing regions of outward and inward migration in the mass–semimajor axis plane for runs M05A (a), M16A (b), M03B (c) and M07B (d).
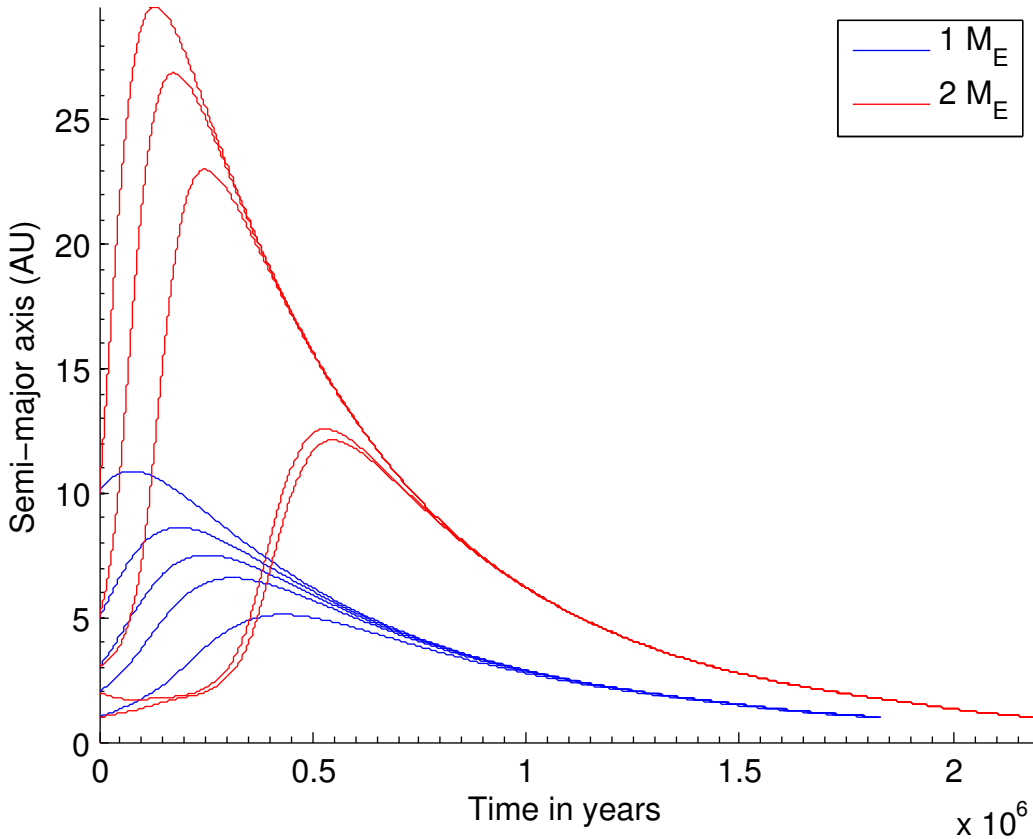
Figure 3.4: Migration lines showing convergent behaviour for 1 and 2 $M_\oplus$ planets in a disc with initial conditions as in M05A.

ally join the same migration line, which then moves inward as the disc disperses. The behaviour of the contours shown in the top left panel of figure 3.3 under the action of disc dispersal are shown in figure 3.6. It is clear that as the disc becomes increasingly optically thin, only heavy planets can sustain outward migration (unless they become too massive and enter the type II migration limit because of gap formation).

3.3.1.2 Influence of mass growth

A planet undergoing mass growth while sitting on a zero-migration line should migrate outward as it accretes, since zero-migration lines for heavier planets lie at larger distances from the central star. However, if the mass growth rate of the
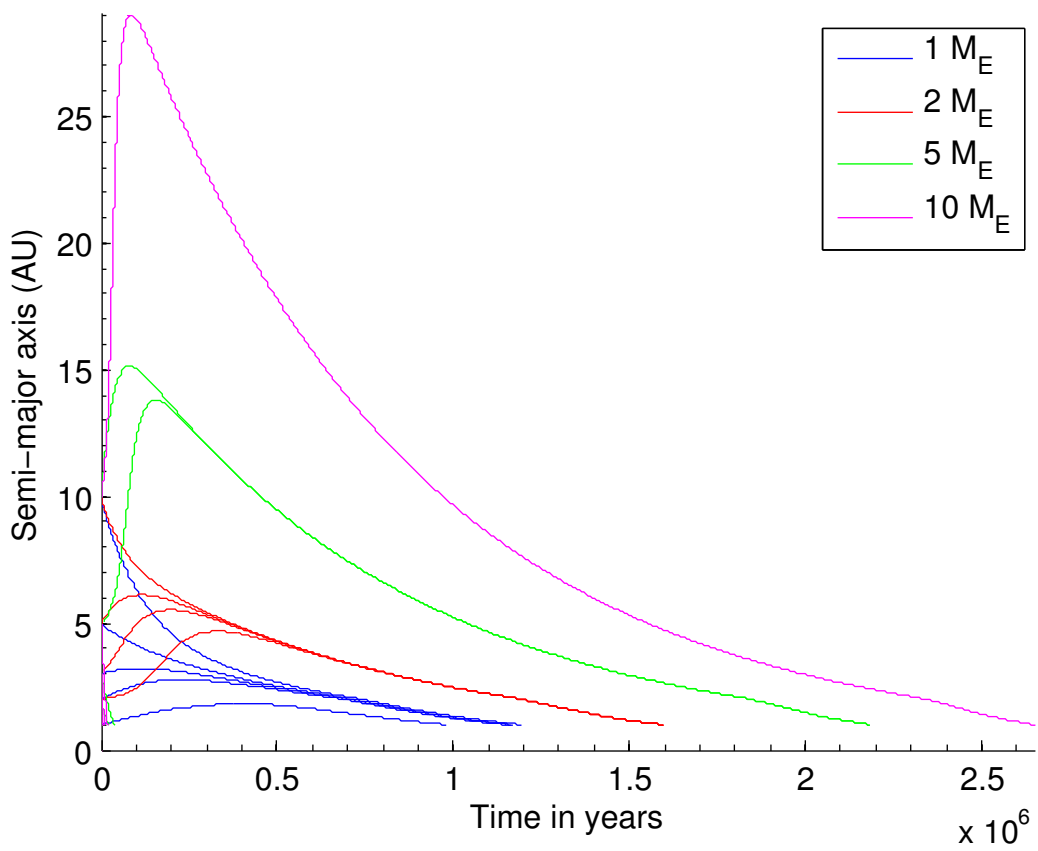
Figure 3.5: Migration lines showing convergent behaviour for planets with varying mass in a disc with initial conditions as in M03B.

Figure 3.6: Contour plots showing regions of outward and inward migration for run M05A at t=0 years (a), t=1,000,000 years (b), t=2,000,000 years (c) and t=3,000,000 years (d).

planet exceeds the outward migration rate due to corotation torques, then a very different fate awaits it. Consider a planet of mass ~ 0.5 M$_\oplus$ sitting at ~ 2 AU in the top left panel of figure 3.6. Rapid growth of the planet up to 10 M$_\oplus$ in less than 1 Myr will put the planet in the regime of rapid inward migration, as its trajectory in the figure will be almost vertical, moving it out of the blue region and into the red one. Very rapid growth of planets, therefore, may not lead to strong outward migration but instead may cause planets to migrate rapidly into the central star. The timing of the growth of planets is crucial in determining their long-term survival.

3.3.2   Individual runs

3.3.2.1   Run M05A

Run M05A has an initial disc mass equivalent to 5 times the MMSN, $\alpha = 0.5$ and $\beta = 1.25$. The initial solids distribution is shown in figure 3.7. The magnitude and sign of migration torques at $t = 0$ are shown in the top left panel of figure 3.3 in comparison to the other runs documented in this section, and the effects of disc dispersal on the migration torques are demonstrated in figure 3.6. It is clear that planets with masses in the range $0.2 \leq M_{\mathrm{p}} \leq 1$ M$_\oplus$, initially located in the disc region 1 – 10 AU, can undergo strong outward migration. Growth of planets to masses of a few M$_\oplus$ may lead to outward migration over distances of tens of AU.

The time evolution of planet masses (top panel), semimajor axes (middle panel) and eccentricities (bottom panel) are shown in figure 3.8. During the first 0.3 Myr, I observe that three planets grow in mass rapidly, and undergo outward migration to ~ 10 AU. The mass growth occurs as a result of planetesimal accretion and planet-planet inelastic collisions, and the rapid growth is assisted by convergent migration within the protoplanet swarm and by the gas envelopes that form within the planet Hill spheres. When the planet masses exceed ~ 20 M$_\oplus$, however, their migration direction changes and they undergo very rapid inward migration through the planetary swarm and interior to 1 AU, the inner boundary of the simulation. During the rapid inward migration, there is very little accretion by these bodies, but they temporarily excite the eccentricities of

Figure 3.7: Initial solid body distribution for run M05A. The blue points mark the locations of the protoplanets, the green line represents the target surface density for a disc of this size and the blue line represents the actual overall solids surface density generated. The semi-periodic fluctuations in surface density is an artefact of my disc model generator routine and the nature of using discrete objects to model a smooth function.
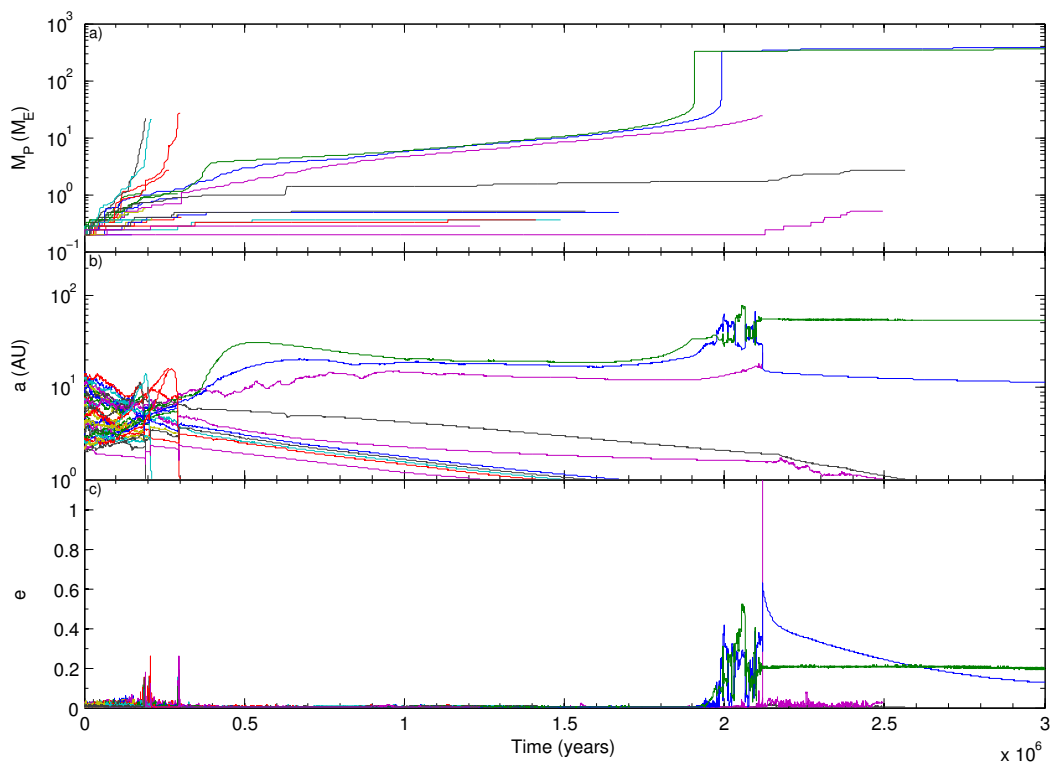
Figure 3.8: Evolution of the masses, semimajor axes and eccentricities of all protoplanets simulation M05A.

the other bodies in the system (see the bottom panel of figure 3.8 between 0.2 – 0.3 Myr).

Between the times 0.3 – 0.5 Myr, three bodies grow to masses larger than 1 $M_\oplus$. The largest of these grows to $\sim$ 4 $M_\oplus$ and migrates outward rapidly to $\sim$ 30 AU, the location of its zero-migration line. I refer to this as "planet A". A second planet ("planet B") grows to a mass $\sim$ 3 $M_\oplus$ by 0.5 Myr, and migrates out to its zero-migration line at $\sim$ 20 AU. A third planet ("planet C") reaches a mass of $\sim$ 2 $M_\oplus$ at 0.5 Myr and migrates out to 10 AU. Although the protoplanet/planetesimal disc of solids is truncated at 15 AU in the initial simulation set-up, outward migration of planets and gravitational scattering transports planetesimals into the outer disc where they are accreted by planets A and B (planet C continues to reside within the original planetesimal disc). Gas accretion ensues once these bodies exceed 3 $M_\oplus$, and their masses grow smoothly up to 20 – 30 $M_\oplus$ between the times 0.5 – 2 Myr. During this time the zero-migration lines move inward (observe the modest inward migration in the middle panel of figure 3.8 between 0.5 – 2 Myr), but continued mass growth helps to counterbalance this effect, and prevents substantial inward migration. At approximately 2 Myr, planets A and B undergo rapid gas accretion and grow to become Jovian-mass giant planets (further gas accretion occurs at the viscous-supply rate). The rapid mass growth induces dynamical instability between planets A and B, causing them to undergo a period of gravitational scattering and eccentricity growth (bottom panel of figure 3.8). The scattering eventually causes planets B and C to collide at 2.1 Myr (when planet C has a mass of 24 $M_\oplus$), leaving two giant planets on eccentric, non-crossing orbits with semimajor axes of 12 and 55 AU. The inner planet has a total mass of 374 $M_\oplus$, and a solid core mass of 27.6 $M_\oplus$, at the end of the simulation. The outer planet has a total mass of 352 $M_\oplus$, and a solid core mass of 10.1 $M_\oplus$.

During the formation of the outer gas giant planets, between time 0.5 – 2.5 Myr, only modest planetary growth occurs in the inner system. An inner resonant convoy, similar to those discussed by McNeil et al. [2005] and Cresswell and Nelson [2006] migrates interior to 1 AU by $\sim$ 1.6 Myr, driven by a more rapidly migrating 0.5 $M_\oplus$ body. This leaves behind two planets that grow to become $\sim$ 3 and 0.4 $M_\oplus$ before migrating interior to 1 AU at $\sim$ 2.5 Myr.

3.3.2.2 Run M16A

Run M16A has a disc mass equivalent to 3 times the MMSN, $\alpha = 1$ and $\beta = 1.25$. The initial solids distribution is shown in figure 3.9. The magnitude and sign of migration torques at $t = 0$ are shown in the top right panel of figure 3.3 in comparison to the other runs documented in this section, and the effects of disc dispersal on the migration torques are demonstrated in figure 3.10. The migration behaviour at $t = 0$ is illustrated by the contours displayed in the top right panel of figure 3.3, and it is clear that outward migration is considerably weaker in this model than in the previously described run M05A. Furthermore, the steepness of the outward migration region as one moves to higher planet masses indicates that the radial extent of outward migration is also reduced relative to model M05A. Placed in the initial disc model, a planet with $M_{\rm p} < 1$ $M_{\oplus}$ orbiting at 1 AU will not undergo outward migration at all, but will instead migrate inward only. Rapid planetary growth is therefore expected to result in much of the solid disc material migrating in toward the star.

The evolution of the planetary masses (upper panel), semimajor axes (middle panel) and eccentricities (bottom panel) are shown in figure 3.11. Protoplanets located initially beyond ~ 2 AU in this disc with masses $\simeq 0.2$ $M_{\oplus}$ (the initial masses of protoplanets in the model) are expected to migrate inward, and looking at the middle panel of figure 3.11, obvious evidence for this migration occurring within the first 0.3 Myr can be seen. Looking at the inner part of the system during the first 0.5 Myr, two examples of resonant, inward migrating convoys being established can be observed. The first to form consists of the six innermost protoplanets in the system. All masses of these planets are < 1 $M_{\oplus}$, except for the outermost body, whose mass has grown to ~ 1 $M_{\oplus}$. The more rapid migration of this body drives the inward migration of the whole convoy. At a time of ~ 0.4 Myr, the next three nearest protoplanets to the central star begin to undergo rapid inward migration, and this is driven by the formation of a ~ 5 $M_{\oplus}$ body who's progenitor protoplanet was located at ~ 4 AU. The growth of this protoplanet induces rapid inward migration, with the system of inner planets being swept interior to 1 AU at $t = 0.55$ Myr.

Three planets initially located at ~ 5 AU become physically detached from

Figure 3.9: Initial solid body distribution for run M16A. The blue points mark the locations of the protoplanets, the green line represents the target surface density for a disc of this size and the blue line represents the actual overall solids surface density generated.
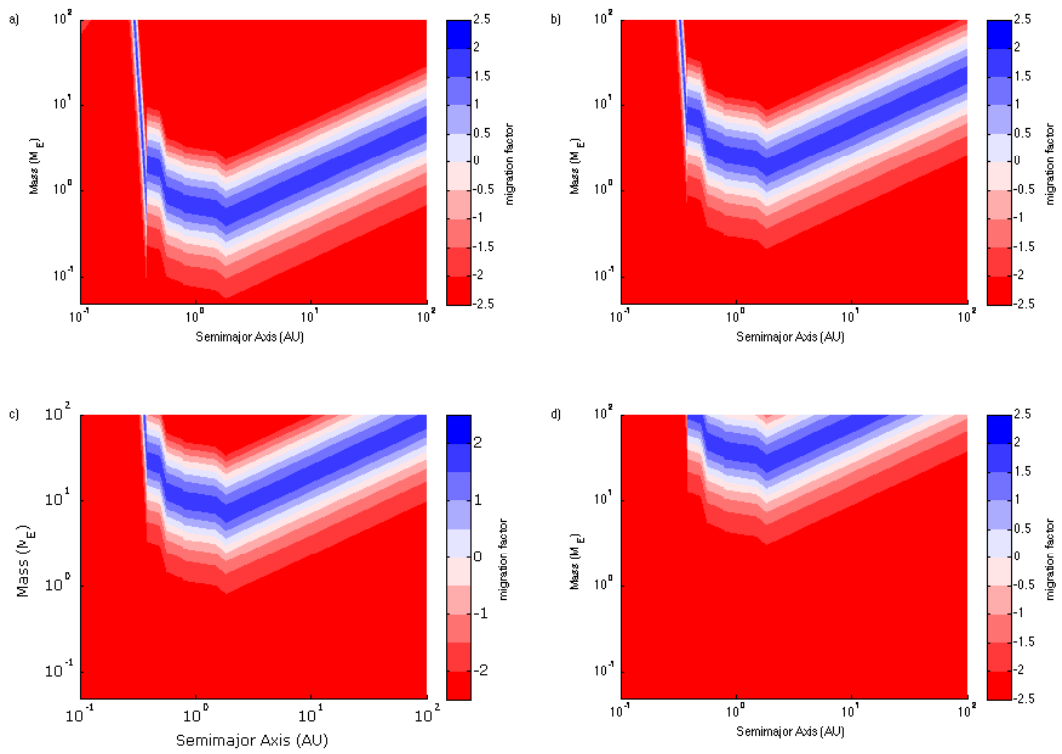
Figure 3.10: Contour plots showing regions of outward and inward migration for run M16A at t=0 years (a), t=1,000,000 years (b), t=2,000,000 years (c) and t=3,000,000 years (d).

Figure 3.11: Evolution of the masses, semimajor axies and eccentricities of all protoplanets in simulation M16A.

the rest of the system after ~ 0.5 Myr, as shown in the middle panel of figure 3.11. These bodies have all grown to masses between $2 - 5$ $M_\oplus$ within this time. The outermost ~ 2 $M_\oplus$ body becomes isolated from planetesimals in the disc such that its mass does not grow after 0.5 Myr. This isolation occurs in large part because the two more massive neighbouring planets accrete the nearby planetesimals. Having achieved masses in excess of 3 $M_\oplus$, these two planets are able to accrete gas. As they do so, they sit on their zero-migration lines and undergo slow inward migration, where the speed of migration is attenuated by the continuing gas accretion and mass growth (the planets try to migrate outward to the zero-migration lines for more massive planets as they grow, at the same time as the zero-migration lines move inward as the gas disc evolves). After ~ 2.6 Myr, the innermost planet reaches a mass of ~ 30 $M_\oplus$ and undergoes rapid gas accretion to become a Saturn-mass gas giant. The rapid mass growth dynamically disturbs the system, as observed in the middle and bottom panels of figure 3.11, causing the outer 2 $M_\oplus$ planet to collide with the middle planet. Shortly after, this merged planet undergoes rapid gas accretion to also become a Saturn-mass gas giant. Saturnian rather Jovian masses are achieved because accretion occurs late in the disc lifetime, such that the gas isolation mass limits the envelope mass to ~ 100 $M_\oplus$.

At the end of the simulation there is an inner planet of total mass 115 $M_\oplus$, with solid core mass 11 $M_\oplus$, orbiting at 2.3 AU, and an outer planet with total mass 127 $M_\oplus$, solid core mass 8.8 $M_\oplus$, orbiting at 3.1 AU.

3.3.2.3 Run M03B

Run M03B has a disc mass equivalent to 5 times that of the MMSN, $\alpha = 0.5$ and $\beta = 1$. The initial solids distribution is shown in figure 3.12. The magnitude and sign of migration torques at $t = 0$ are shown in the bottom left panel of figure 3.3 in comparison to the other runs documented in this section, and the effects of disc dispersal on the migration torques are demonstrated in figure 3.13. The migration behaviour of this model at $t = 0$ is illustrated by the lower left panel in figure 3.3, showing that this disc is intermediate between the two previous models discussed (M05A and M16A) in terms of the strength of outward migration.
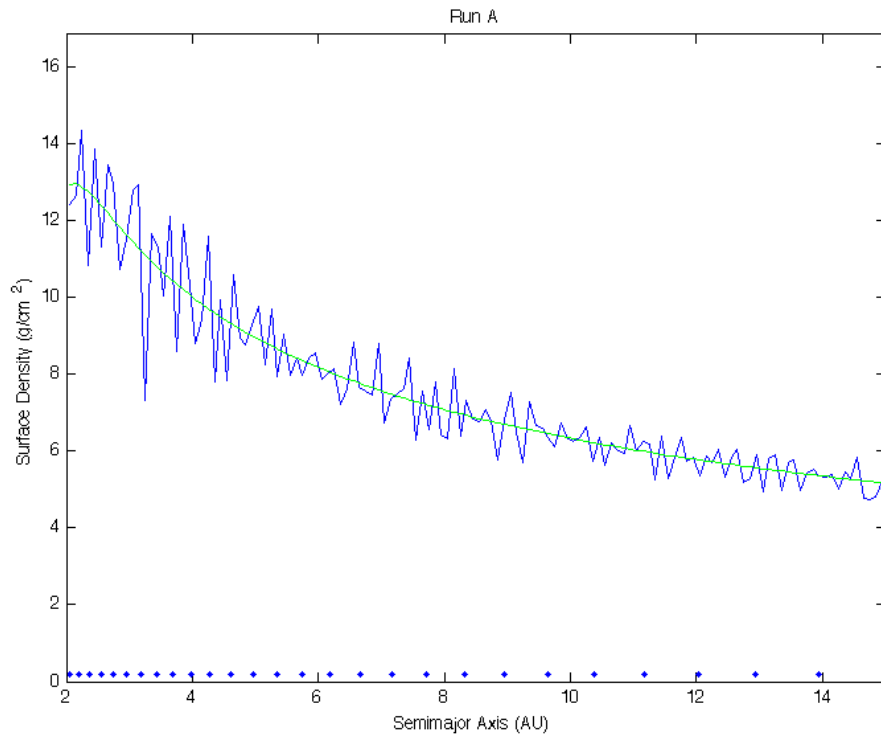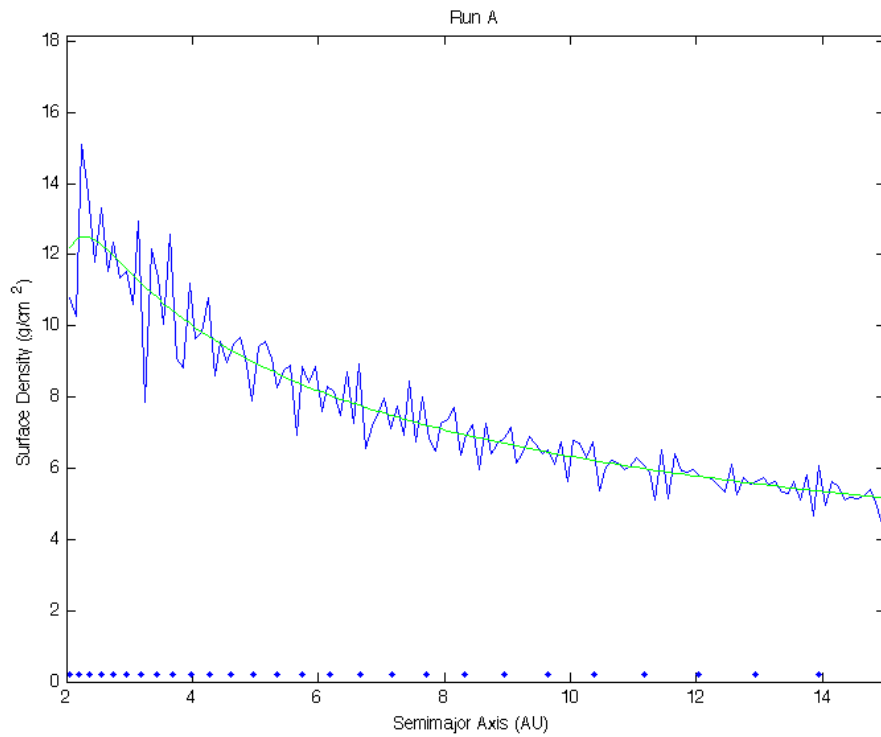
Figure 3.12: Initial solid body distribution for run M03B. The blue points mark the locations of the protoplanets, the green line represents the target surface density for a disc of this size and the blue line represents the actual overall solids surface density generated.
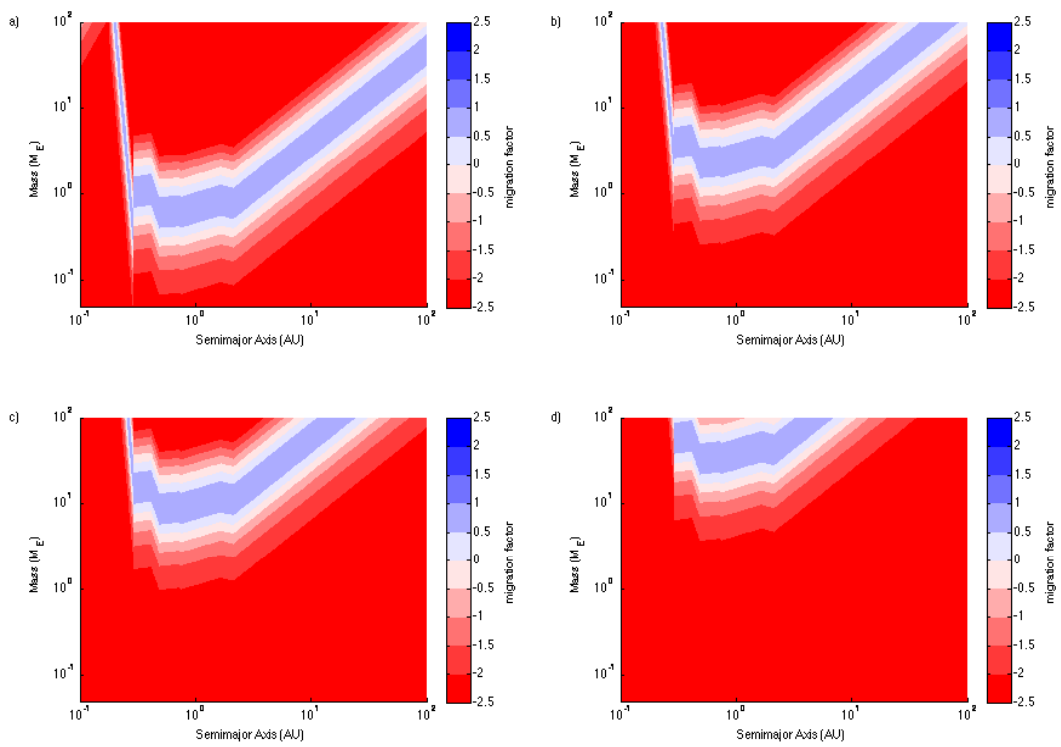
Figure 3.13: Contour plots showing regions of outward and inward migration for run M03B at t=0 years (a), t=1,000,000 years (b), t=2,000,000 years (c) and t=3,000,000 years (d).
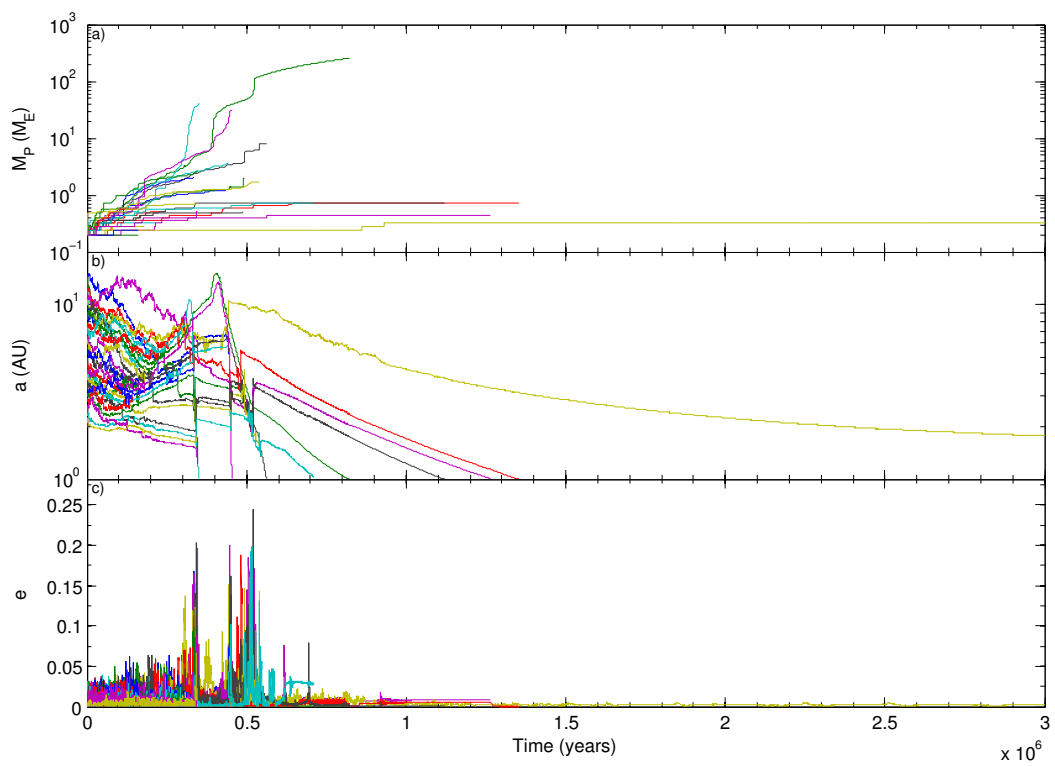
Figure 3.14: Evolution of the masses, semimajor axes and eccentricities of all protoplanets in simulation M03B.

The evolution of the planetary masses (upper panel), semimajor axes (middle panel) and eccentricities (bottom panel) are shown in figure 3.14. As expected from comparing the migration behaviour of the runs M16A and M03B in figure 3.3, the initial stages of run M03B show some similarities to run M16A. Protoplanets initially located in the region of the protoplanet/planetesimal disc between 10 – 15 AU migrate inward to the region centred around 2 – 3 AU. The inner planets, however, do not show a strong tendency to migrate inward (differing in this regard from run M16A), and the convergent migration stimulates substantial growth within the protoplanet swarm, as seen in the upper panel of figure 3.14, where the planet masses are seen to increase during the first 0.5 Myr, and in the middle panel where it is clear that collisional growth reduces the number of planets. The strong planetary growth, however, also leads to rapid inward migration. Bodies that reach masses in excess of 20 $M_{\oplus}$ undergo rapid inward migration through the disc of protoplanets/planetesimals and interior to 1 AU, exciting the eccentricities of the remaining planets as they do so. The bodies that rapidly migrate through the inner boundary at 1 AU would hit the star if their long-term evolution were followed.

One of the quickly migrating planets (shown by the upper green line in the top panel of figure 3.14) grows to be massive enough (approximately 30 $M_{\oplus}$ of solids) to undergo rapid gas accretion during the inward migration. It reaches its gas isolation mass at a mass equal to 114 $M_{\oplus}$, and transitions to type II migration, drifting interior to 1 AU shortly after 0.8 Myr has elapsed. At this point in time, the planet mass is ~ 250 $M_{\oplus}$, and it is undergoing gas accretion from the disc at the viscous-supply rate. I have followed the evolution of this body after it has traversed the inner boundary of the simulation, treating it as an isolated body and neglecting its interaction with other bodies in the system (I refer to this as single-body analysis). The evolution is displayed in figure 3.15, the planet reaches a semimajor axis of 0.25 AU and has a mass of 524 $M_{\oplus}$ after 3 Myr, making it an excellent candidate for a hot Jupiter.

No other planets grow substantially during the evolution of this run. Figure 3.14 shows that only a single planet with mass ~ 0.35 $M_{\oplus}$ survives beyond 1 AU, coming to rest at a semimajor axis of ~ 1.9 AU.
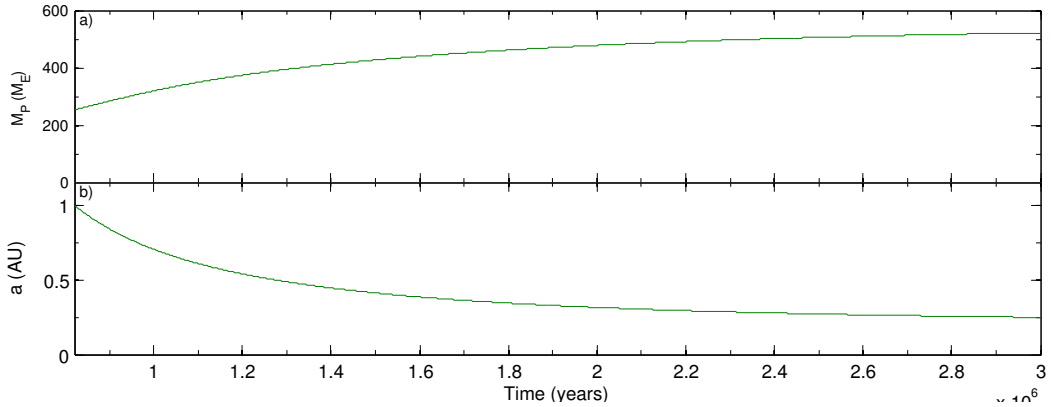
Figure 3.15: Evolution of mass and semimajor axis of single body extension run for the hot Jupiter in simulation M03B starting at 0.821 Myr.

3.3.2.4 Run M07B

The final run I describe in detail is M07B, which has a mass equivalent to 5 times the MMSN, $\alpha = 0.5$ and $\beta = 1.5$. The initial solids distribution is shown in figure 3.16. The magnitude and sign of migration torques at $t = 0$ are shown in the bottom right panel of figure 3.3 in comparison to the other runs documented in this section, and the effects of disc dispersal on the migration torques are demonstrated in figure 3.17. The steep temperature gradient and relatively shallow surface density gradient allow this disc model to support strong outward migration over a large radial extent, as illustrated by the contours in the bottom right panel of figure 3.3. This plot demonstrates clearly that sub-Earth mass bodies orbiting in the vicinity of 1 AU will experience strong outward migration, possibly out beyond 100 AU.

The evolution of planetary masses (top panel), semimajor axes (middle panel) and eccentricities (bottom panel) are shown in figure 3.18. The initial growth and outward migration of protoplanets in the inner region of the swarm leads to strongly convergent migration, and rapid growth of a number of bodies up to $\sim 10\ M_\oplus$ within the first 0.3 Myr. As observed in the previously described runs, this leads to rapid inward migration of these planets because the horseshoe libration time becomes much shorter than the thermal/viscous diffusion time for these bodies. After 0.5 Myr, there are only three bodies left in the simulation:
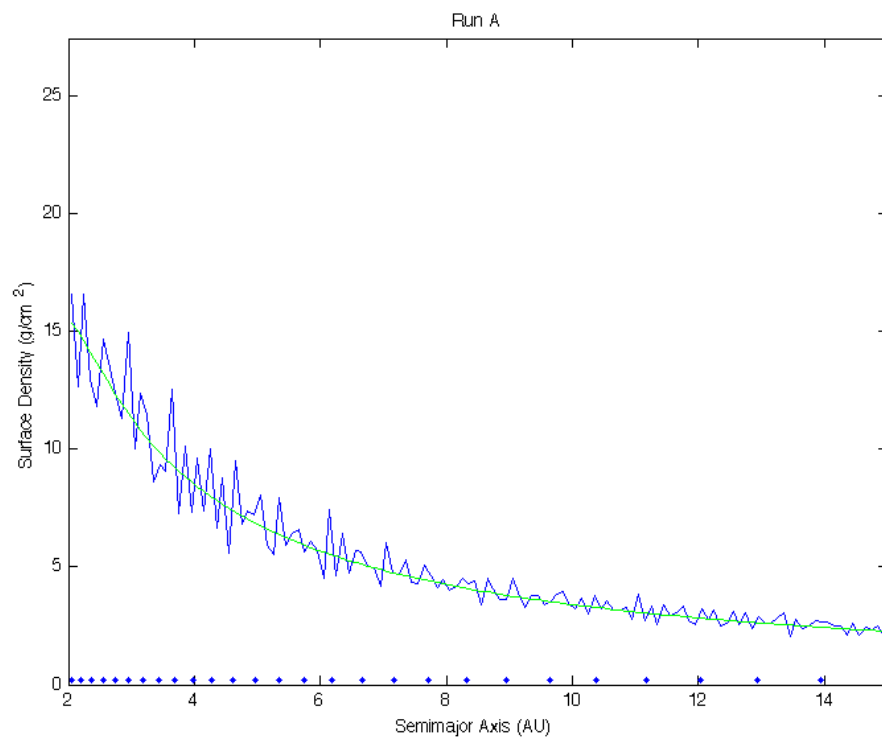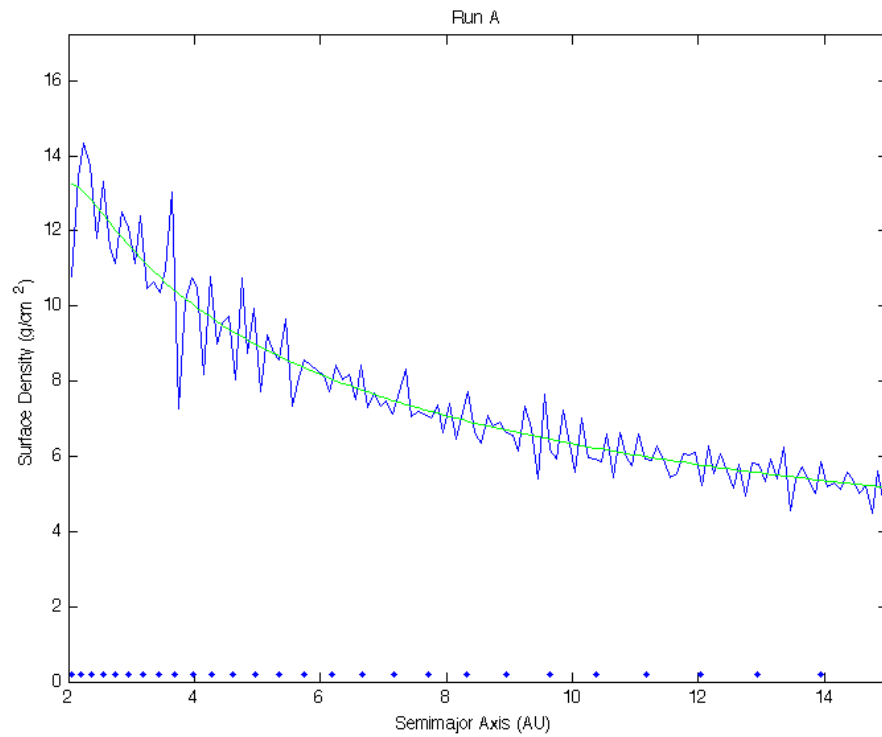
Figure 3.16: Initial solid body distribution for run M07B. The blue points mark the locations of the protoplanets, the green line represents the target surface density for a disc of this size and the blue line represents the actual overall solids surface density generated.
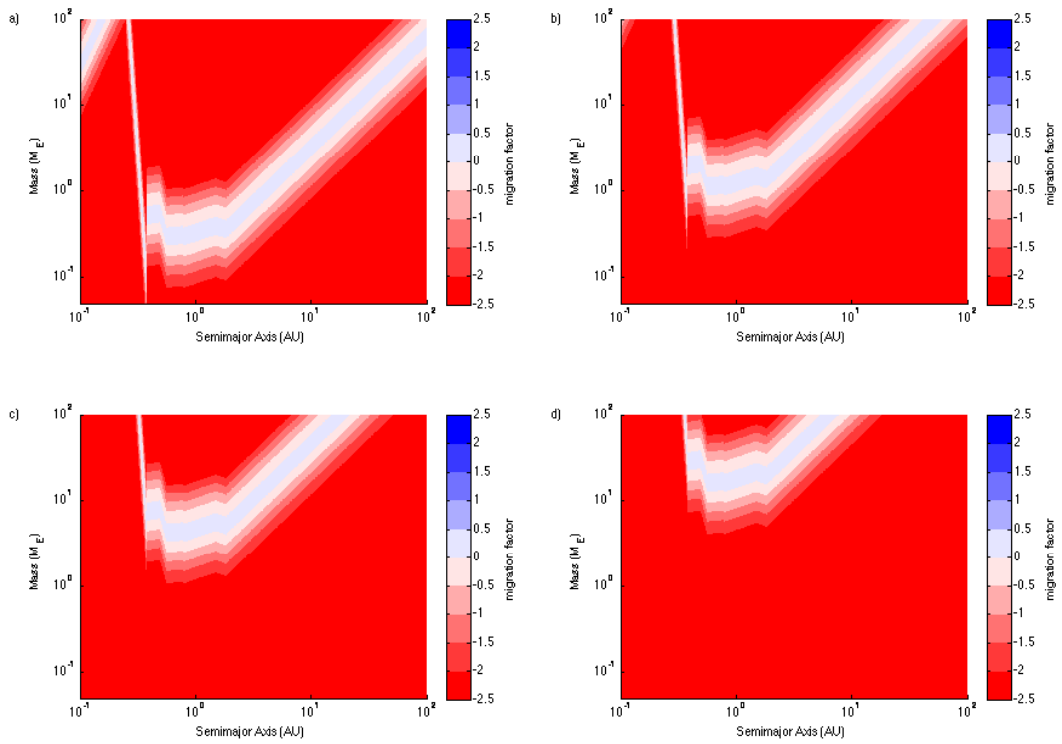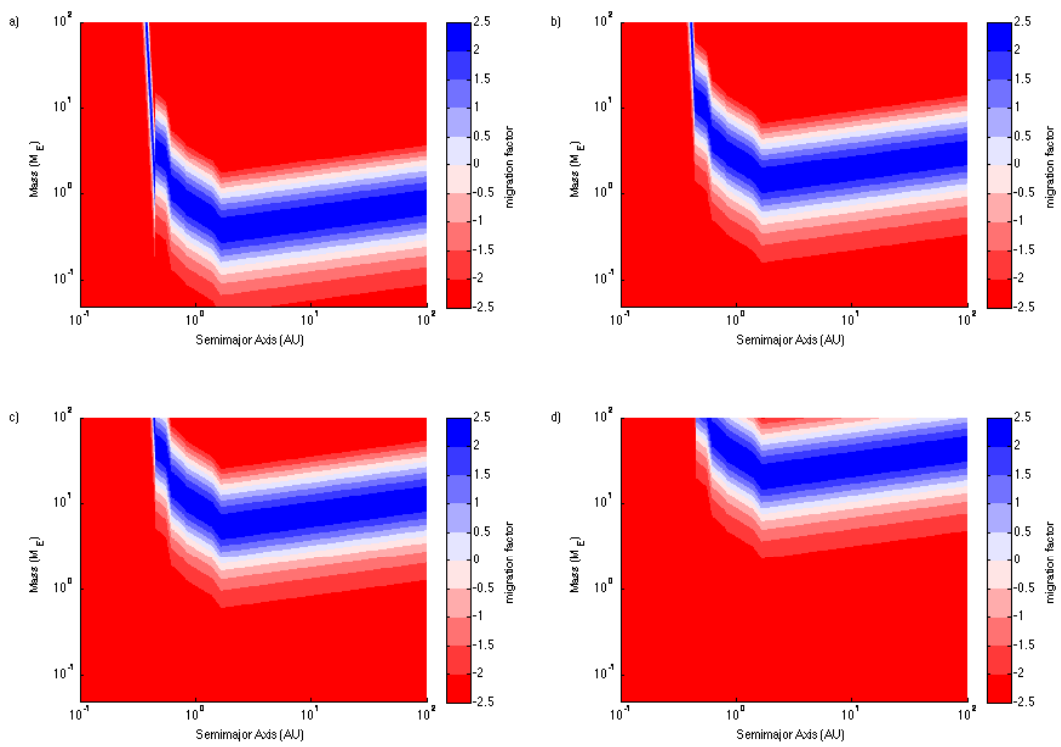
Figure 3.17: Contour plots showing regions of outward and inward migration for run M07B at t=0 years (a), t=1,000,000 years (b), t=2,000,000 years (c) and t=3,000,000 years (d).
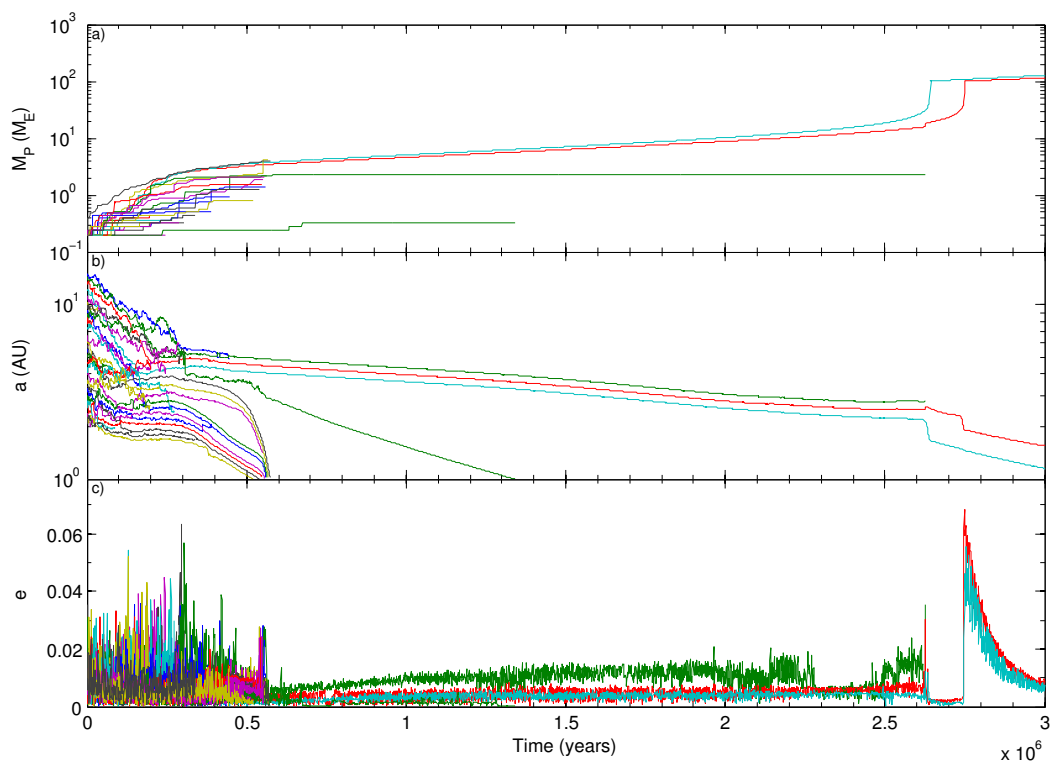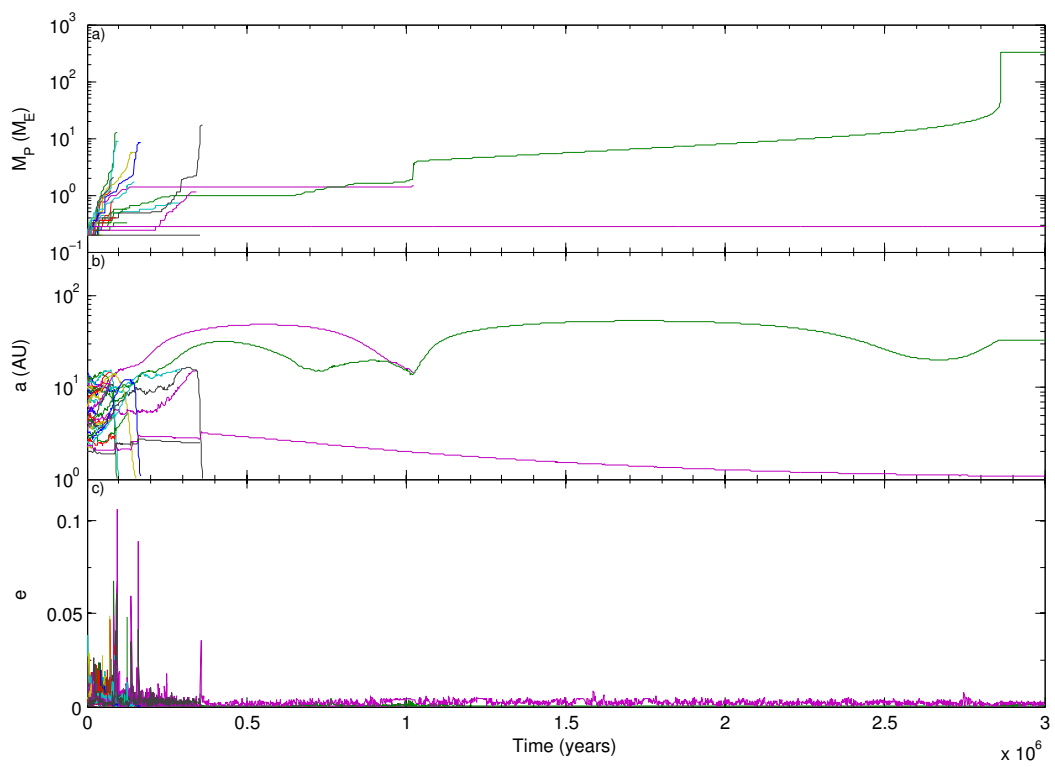
Figure 3.18: Evolution of masses, semimajor axes and eccentricities of all proto-planets in simulation M07B.

two planets orbiting at ~ 15 AU each with masses ~ 2 M$_\oplus$; one protoplanet with mass ~ 0.3 M$_\oplus$ orbiting at ~ 2 AU. The two outer bodies collide shortly after 0.5 Myr, and the resulting planet undergoes slow gas accretion, migrating outward as it does so. After 2.8 Myr it undergoes rapid gas accretion and becomes a Jovian mass (319 M$_\oplus$) gas giant planet, with a 5.2 M$_\oplus$ solid core, orbiting at ~ 33 AU. As in model M05A, I find that gas giant planets can be formed at large radius from the central star by the migration and gas accretion onto a solid core. In both of these models (and others not discussed in detail), the mode of formation is one in which an initial generation of massive protoplanets form and migrate in toward the central star, followed by a second generation of more isolated lower mass cores that can migrate out slowly and accrete gas at the same time. Such a model may provide a natural explanation for the massive planets orbiting at large distance from their host stars, such as HR 8799 [Marois et al., 2010], Fomalhaut [Kalas et al., 2008], and Beta Pictoris [Lagrange et al., 2010], that are being discovered by direct imaging surveys.

3.3.3 Summary of all runs

I ran 40 simulations covering two random-number seed realisations of runs with $f_\mathrm{enh} = 5$ or 3, surface density power-law indices in the range $0.5 \leq \alpha \leq 1.25$, and temperature power-law indices satisfying $0.75 \leq \beta \leq 1.5$. In total 19 gas giant planets were formed in these runs, and their properties are summarised in figure 3.19 and table 3.2. The giant planet masses range from 115 to 670 M$_\oplus$, and have solid core masses in the range 3.6 – 39 M$_\oplus$. Looking at the upper panel of figure 3.19, most giant planets are grouped within the mass range 320 to 400 M$_\oplus$, and this is very likely to be an artefact of my gas accretion procedure that limits the planet mass obtained during rapid gas accretion to be the Jovian mass. A more sophisticated procedure would be sensitive to local conditions in the disc, and result in a broader spread of planet masses, and this is clearly one future improvement that I will need to implement in my modelling procedure. Nonetheless, I do also obtain giant planets outside of this mass range. Run M03B formed a 523.8 M$_\oplus$ planet, as discussed in section 3.3.2.3, due to a gas giant forming within the first 0.5 Myr, and subsequently accreting viscously and
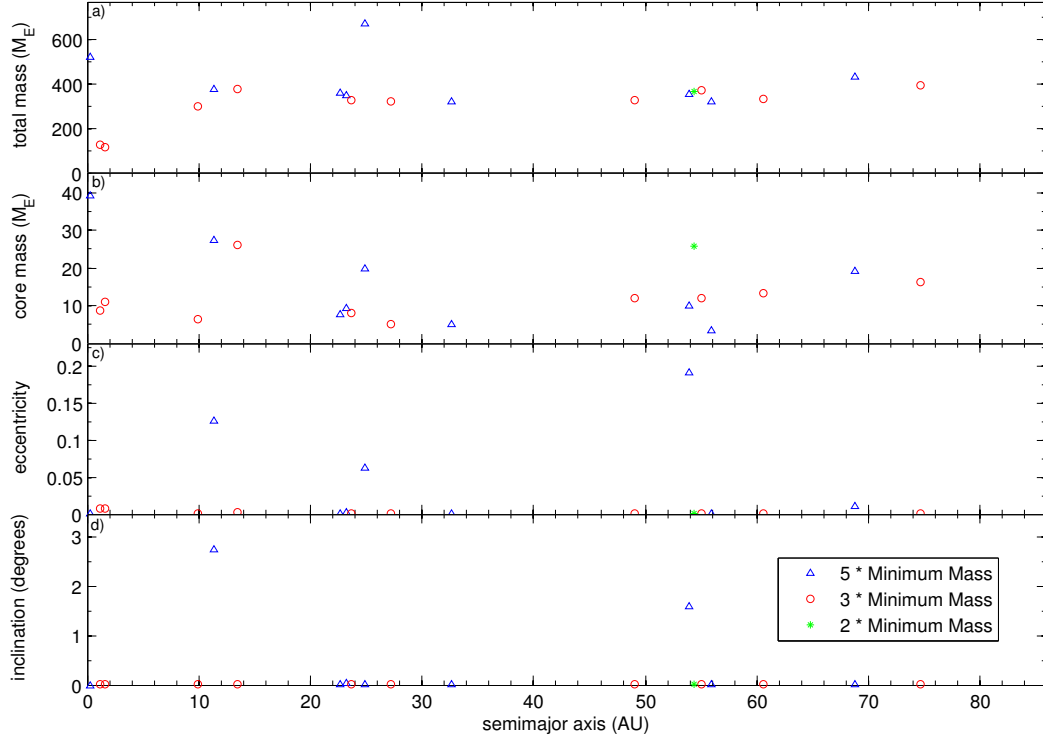
Figure 3.19: Summary of total masses, core masses, eccentricity and inclination against semimajor axis for all gas giant planets formed.

migrating via type II migration to its final location at 0.25 AU. The heaviest planet formed during run M11A, and this was the result of two gas giant planets colliding, having each formed at between 20 and 30 AU from the central star due to their cores migrating outward. Employing a pure hit-and-stick prescription for planetary collisions, however, probably leads to an overestimate of the final mass of this planet. Three planets were formed with masses below the imposed Jovian-mass limit. Run M12B produced a 296 $M_\oplus$ planet orbiting at 9.8 AU, and as described in section 3.3.2.2, run M16A produced a pair of Saturn-mass objects orbiting at 1.15 and 1.55 AU. These planets formed late in the disc lifetime, such that their gas isolation masses were below the Jovian mass.

Most of the giant planets formed at semimajor axes substantially beyond 10 AU. Indeed, only 4 out of 19 giant planets formed interior to 10 AU. The reason for this is that the most common mode of gas giant planet formation in
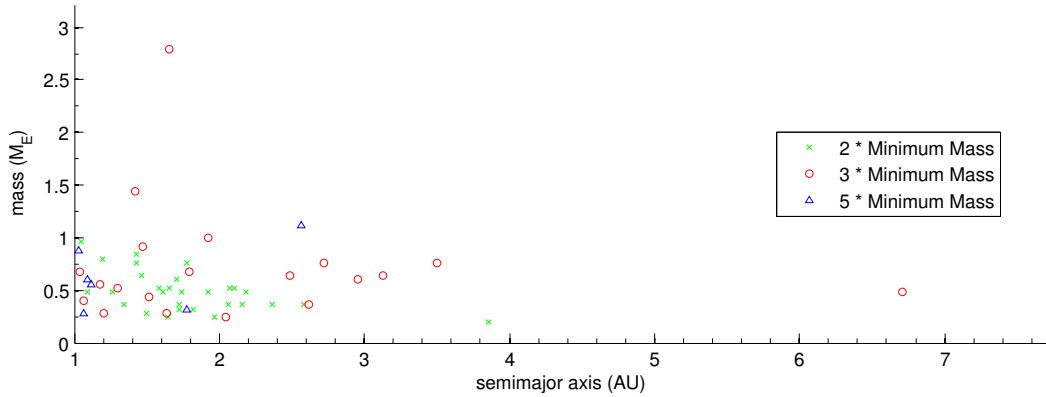
Figure 3.20: Summary of masses against semimajor axis for all small surviving planets outside 1 AU.

the simulations was the formation of a core of modest mass in the interior disc, that then migrates outward over large distances before accreting a gas envelope. Many massive cores formed during the early stages of the disc life times in the simulations, and were able to undergo gas accretion. Their rapid inward migration, however, prevented them from surviving. Giant planets that form closer to the star and survive tend to be in disc models (M03B and M16A) that generate weaker corotation torques.

There are three simulations that lead to the formation of surviving multiple giant planets. Run M05A produces a pair of Jovian mass planets orbiting at 11.4 and 53.9 AU, as described in section 3.3.2.1, and M05B also produced a pair of Jovian mass objects orbiting at 23.3 and 68.8 AU. Note that these runs were identical apart from the random number seed used to generate initial conditions. Run M16A produced a pair of Saturn-mass planets orbiting at 1.15 and 1.55 AU. Almost all giant planets formed in the simulations are on circular, non-inclined orbits. The only planets with significant eccentricities are those in run M05A, where gravitational scattering during the formation caused the growth of eccentricity.

One surprising result to come out of the simulations is the lack of correlation between initial disc mass and the frequency of giant planet formation. Discs with $f_{\mathrm{enh}} = 5$ formed 9 giants and those with $f_{\mathrm{enh}} = 3$ formed 10. This led us to

question whether less massive discs might be able to form gas giants. To examine this, I performed additional simulations (labelled 'R' in table 3.1) based on the most successful models in the $f_{\mathrm{enh}} = 3$ and 5 runs. All bar one failed to produce any gas giants. Run R07B, a $f_{\mathrm{enh}} = 2$ disc, did produce a single Jovian mass gas giant (shown in figure 3.19).

In addition to the giant planets discussed above, the simulations also resulted in the formation and survival of lower mass bodies beyond 1 AU in the disc. These are shown in figure 3.20. The rapid growth of cores, followed by rapid inward migration, has the effect of clearing much of the solid material from beyond 1 AU, and the outward migration of modest sized cores that evolve into gas giants also clears this region. Nonetheless, terrestrial mass bodies do form and survive in the simulations, although figure 3.20 shows that these tend to be in the lower mass discs. One noticeable and interesting observation about the simulation results is the lack of super-Earth and Neptune mass planets. The rapid formation of massive cores that undergo fast inward migration is a major cause of this (driven by efficient capture of planetesimals and convergent migration), but a contributing factor is the fact that planets with masses greater than 3 $\mathrm{M}_\oplus$ can begin to undergo gas accretion in my models. A higher threshold for gas accretion would probably allow some of the giant planets that formed to have maintained lower masses. These observations provide a useful guide to the types of modifications that the modelling procedure requires in order to form planets with the same characteristics as those which are contained in the extrasolar planet observational database.

3.3.3.1 Single-body analysis

The inner edge of my simulations was set at 1 AU. I ran single body runs for each object that was lost beyond this inner edge so as to identify any bodies that would have become short period gas giants, and to obtain an estimate of the distribution of smaller bodies in this inner region. These runs are effectively continuation runs, but with a smaller time step size, and a smaller inner boundary at 0.1 AU. It is important to note that these single body runs did not include the influence of any other planets in the system, and did not account for any material

Table 3.2: Summary of gas giants formed.

Simulation	f_{enh}	α	β	a (AU)	e	i (degrees)	mass ($M_\oplus$)	core mass ($M_\oplus$)
M03B	5	0.50	1.00	0.24818	0.000001	0.0000	523.79	39.39
M05A	5	0.50	1.25	11.39435	0.125762	2.7366	374.36	27.57
M05A	5	0.50	1.25	53.91049	0.191585	1.5949	352.20	10.11
M05B	5	0.50	1.25	23.26593	0.003140	0.0299	351.47	9.51
M05B	5	0.50	1.25	68.79704	0.011044	0.0195	433.61	19.18
M06A	3	0.50	1.25	54.99131	0.000684	0.0026	369.38	12.11
M06B	3	0.50	1.25	74.69739	0.000847	0.0012	392.50	16.10
M07A	5	0.50	1.50	55.91612	0.000897	0.0006	319.86	3.60
M07B	5	0.50	1.50	32.59897	0.000980	0.0057	319.24	5.19
M08A	3	0.50	1.50	13.41661	0.001873	0.0106	374.61	26.13
M08B	3	0.50	1.50	60.55699	0.000785	0.0021	333.38	13.35
M11A	5	0.75	1.25	24.93238	0.063072	0.0053	669.88	19.7
M11B	5	0.75	1.25	22.70169	0.000959	0.0069	361.13	7.79
M12B	3	0.75	1.25	9.87598	0.000726	0.0022	296.43	6.47
M14A	3	0.75	1.50	27.22201	0.000179	0.0046	323.17	5.00
M14B	3	0.75	1.50	49.00695	0.000497	0.0036	328.24	12.07
M16A	3	1.00	1.25	1.55415	0.008245	0.0008	114.91	10.95
M16A	3	1.00	1.25	1.15495	0.007372	0.0008	126.85	8.83
M18B	3	1.00	1.50	23.61206	0.000516	0.0111	325.91	7.95
R07B	2	0.75	1.50	54.41991	0.000599	0.0016	367.30	25.77

that would have been present between 0.1 – 1 AU during the early evolution of the system. As such, the results merely provide a guide to the planets that can survive within this radial range.

Figure 3.21 shows a summary of all non-giant planets left remaining in the 0.1 to 1 AU region from all the $f_{\text{enh}} = 3$ and 5 models. Objects with masses less than 1 $M_\oplus$ are clearly more common than those with larger masses because of their reduced migration rates. Also, smaller semimajor axes seem the more likely outcome. All objects included in this figure have masses below 3 $M_\oplus$ and have not been able to undergo gas accretion. The only gas giant to survive in the region 0.1 – 1 AU is the one described already in section 3.3.2.3.

A large number of bodies are lost beyond 0.1 AU, ranging from the smallest protoplanets all the way up to Jupiter sized gas giants, potentially providing the central star with a significant enrichment of heavy elements. These bodies are summarised in figure 3.22, which shows the masses of the planets as they cross the boundary at 1 AU in the lower panel, and their masses as they cross the boundary at 0.1 AU in the upper panel. The horizontal axes show the time of loss through the boundary at 0.1 AU. It is clear that a number of the massive cores that migrate
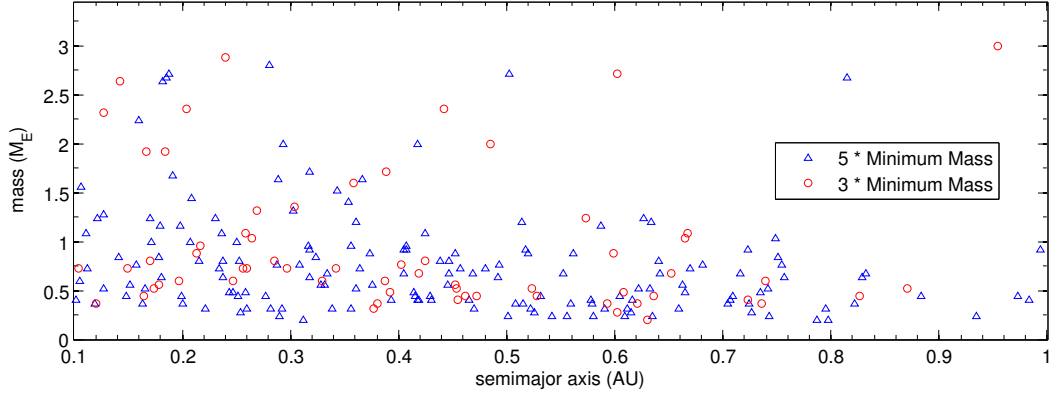
Figure 3.21: Summary of masses against semimajor axis for all small surviving planets interior to 1 AU. Note that these data were obtained using the single-body analysis described in the text.

through the 1 AU boundary accrete gas and become gas giants, although their masses normally reach values between $100 - 200$ $M_\oplus$ because the gas isolation mass is below the Jovian-mass in the inner disc. Type II migration drives them through the boundary at 0.1 AU. It is also clear that a number of bodies migrate inside 1 AU with masses in the range $4 - 10$ $M_\oplus$ and grow through gas accretion to masses between $30 - 50$ $M_\oplus$. Type I migration, however, forces these bodies to migrate into the star before they can become giants. Their corotation torques are saturated, and so rapid inward migration is driven by Lindblad torques.

Some of the bodies passing through the 0.1 AU boundary at late times could have survived. I ran extended single body runs for the five planets with masses greater than 25 $M_\oplus$ lost beyond 0.1 AU in the last 500,000 years of simulation time. Two collided with the central body at ~ 2.75 Myr, but the other three survived at 0.086, 0.0428 and 0.016 AU with masses 344, 164 and 550 $M_\oplus$, respectively. I have not included these results along with the other gas giants since their simulation conditions were overly simplified compared to the rest. All three bodies entered the 1 AU zone with just a few Earth masses, and so would in reality have interacted with other bodies and planetesimals formed there which were not modelled. Also, the body ending up at 0.016 AU would most likely have been accreted by the central star a short while later.
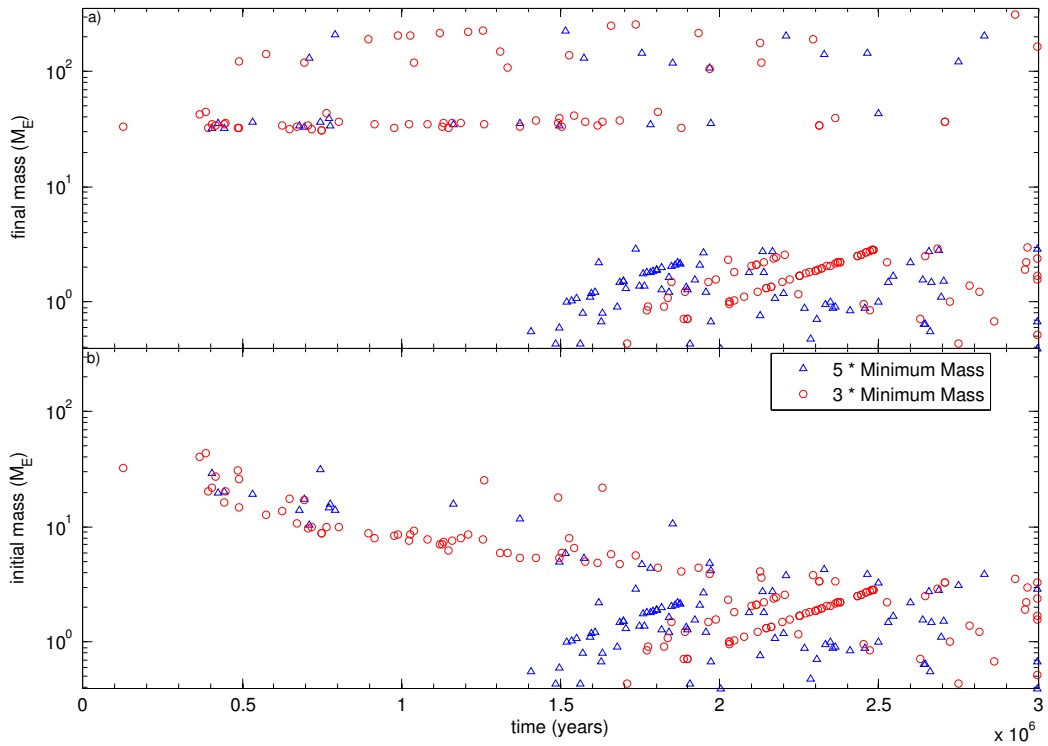
Figure 3.22: Summary of final masses and initial masses against time of loss for all planets that were lost beyond 1 AU that have been evolved via single body analysis and then lost beyond 0.1 AU. The initial mass corresponds to the mass of planets as they cross 1 AU and single body analysis begins. The final mass corresponds to the mass of planets as they cross 0.1 AU.

The survivability of these giant planets formed in single body analyses between 1 and 0.1 AU depends on exactly how the gas disc dissipates. The exponential dissipation of gas provides a reasonable approximation for the bulk of the gas dissipation when it is dominated by viscous evolution [Fogg and Nelson, 2007], but at later times the structure of a viscously evolving disc that is being photo evaporated by UV radiation from the central star changes substantially [Clarke et al., 2001] with a low density inner cavity being formed. Clearly such a model needs to be incorporated into the simulation procedure outlined here to make reasonable predictions about the nature of surviving short-period planets.

3.3.4 Eccentricity modulation of corotation torques

Recent numerical simulations [Bitsch and Kley, 2010] indicate that corotation torques are substantially reduced in their effectiveness when a planet develops an eccentric orbit. In particular, one would expect the corotation torque to be effectively quenched when the radial excursion associated with the eccentric orbit exceeds the width of the horseshoe region. In order to simulate this effect, I have run a few simulations (labelled 'E' in Table 3.1) where the eccentricity modulation function in equation 3.12 is switched on.

The effect of this was as one might expect: growth was significantly stunted compared to the corresponding runs without this reduction factor (runs M05A/B compare to eccentricity damping runs E01A/B and M06A/B compare to E02A/B). Nearly all protoplanets were lost beyond the inner edge by approximately 1 Myr and most protoplanets were lost within half this time. Only one planet survived to run completion out of all four of the simulations and its final position is shown in figure 3.23, which shows a summary of surviving planets from the 'E' runs, as well as those discussed below in which the enhanced planetesimal capture radii are switched off. A plot showing the time evolution of this particular simulation is given in figure 3.24, where I have plotted the eccentricity in the bottom panel as e/x_s. It is clear that planet-planet interactions maintain values of $e/x_s \geq 1$ throughout the simulation, until it is depleted of planets through their inward migration. This result suggests that closer investigation of the role of planetary eccentricity in regulating the strength of corotation torques needs to
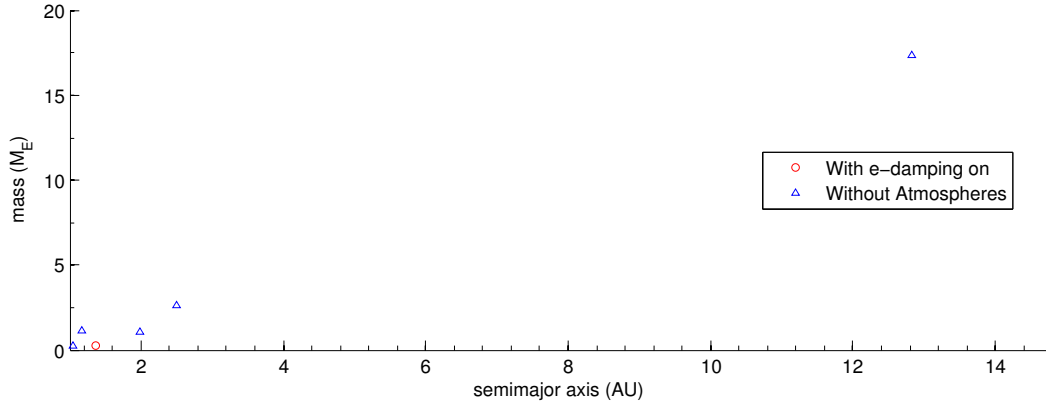
Figure 3.23: Summary of masses against semimajor axis for all small surviving planets outside 1 AU for both runs where eccentricity damping was turned off and where enhanced capture radii due to atmospheric drag were turned off.

be undertaken, since the modest evidence I have accumulated suggests that mutual encounters between planets may remove the benefits provided by corotation torques in enhancing the formation and survival of planets. Similar conclusions have been reached in a recent study by McNeil & Nelson (In preparation) that examines the formation of hot Neptunes and super-Earth planets in radiatively inefficient discs.

3.3.5 Capture radii enhancement switched off

A common outcome within my simulations has been the rapid formation and growth of planetary cores, and their subsequent rapid migration inward. One reason for this rapid growth is my adoption of an enhanced capture radius for planetesimals arising because of a putative gaseous envelope settling onto protoplanets during their formation.

I re-ran the simulations described in section 3.3.2 without enhanced capture radii. Growth was noticeable slower as expected in all four runs. Two runs, however, (corresponding to the M03B and M07B non-atmosphere runs) did manage to form one gas giant planet each.

The time evolution of run M03B-NA (non-atmosphere) is shown in figure 3.25. A planet grows slowly to just over 3 $M_{\oplus}$ by approximately 500,000 years. It sits
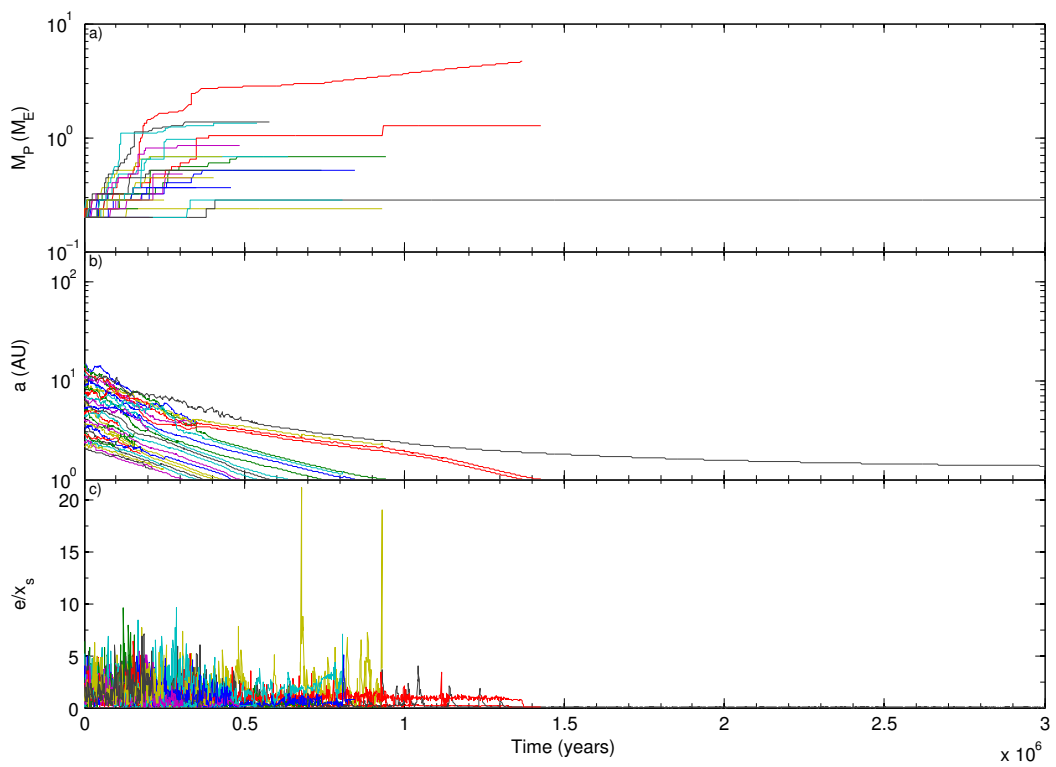
Figure 3.24: Evolution of masses, semimajor axes and eccentricities of all proto-planets in simulation E02B.
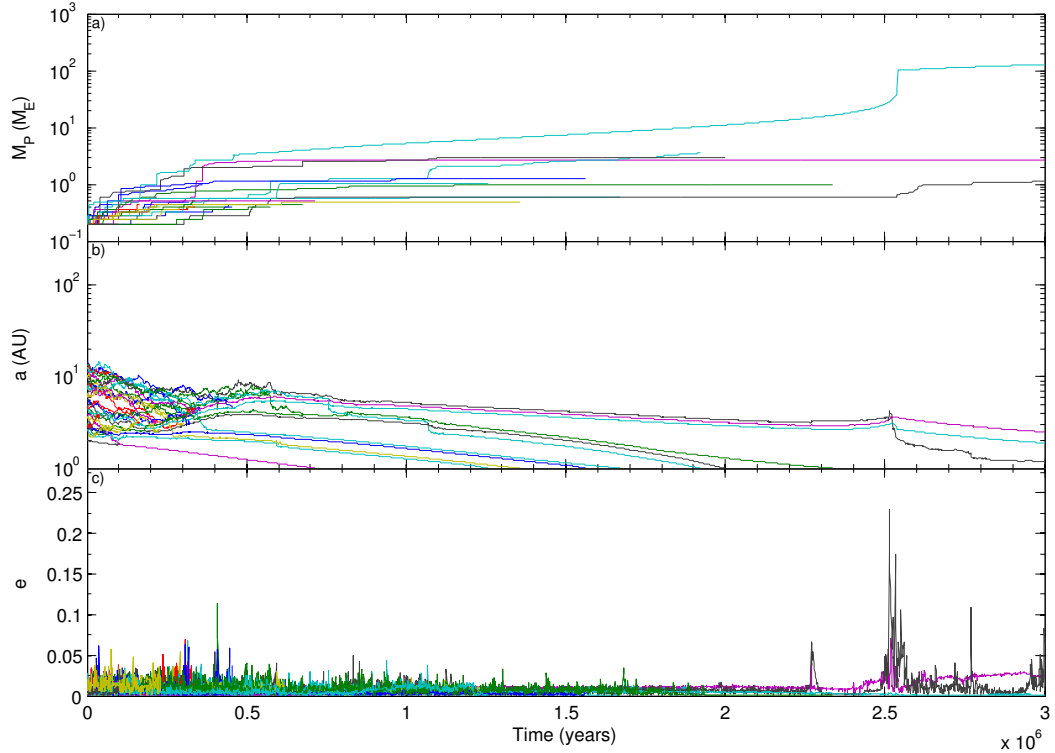
Figure 3.25: Evolution of masses, semimajor axes and eccentricities of all proto-planets in simulation M03B-NA.

in an area of the disc largely cleared of solid material by other protoplanets and slowly accretes gas before eventually undergoing runaway gas accretion at 2.5 Myr and ends up at 2 AU with a mass of 126 $M_\oplus$.

Run M07B-NA forms a gas giant by means of three 1-1.5 $M_\oplus$ bodies migrating out to large semimajor axes, and then merging to form a 3.5 $M_\oplus$ body at 40 AU which slowly accretes gas until runaway gas accretion occurs at 2.8 Myr. The planet ends up at 50 AU with a mass of 319 $M_\oplus$. The lower mass planets that survived in these runs are shown in figure 3.23. Interestingly, one of these is a Neptune-sized planet.

Figure 3.26: Mass vs semimajor axis plot comparing observed extrasolar planets with my simulation results.
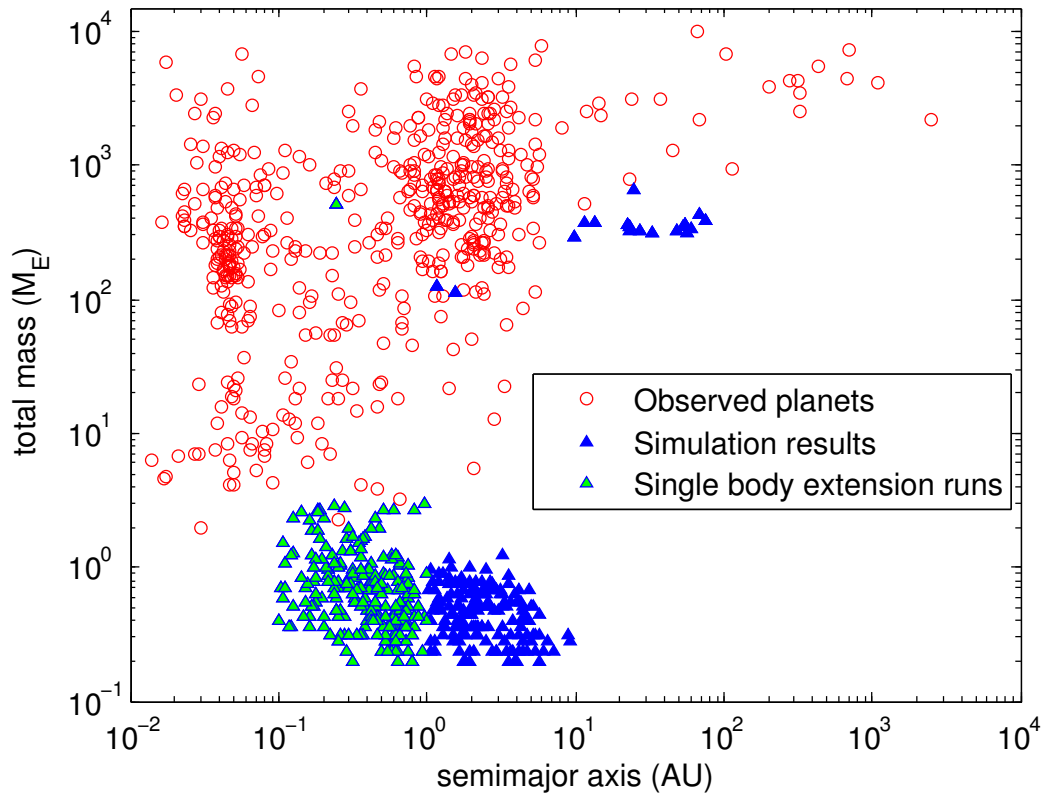
3.4 Comparison with observations

The work presented in this chapter is not intended to be a serious attempt at planetary population synthesis modelling, unlike the work presented by Ida et al. [2008] and Mordasini et al. [2009b]. Instead it is aimed at exploring the consequences of having strong corotation torques operating during the oligarchic growth stage of planetary systems formation, and understanding how planetary growth, migration and planet-planet interactions combine to form planetary systems. Nonetheless, it is of interest to examine how well the simple models that I have presented compare with the observational data on extrasolar planets.

Figure 3.26 shows a mass-period diagram with my results overlaid on all current observed exoplanets (sourced from www.exoplanet.eu). My shorter period giant planets lie well in the range of already detected exoplanets both in terms of mass and semimajor axis. My longer period planets, however, lie in an area that is sparsely populated with observational results. It is worth noting, however, that this region of parameter space is much more problematic for the detection of planets, as observations rely on direct imaging methods rather than radial velocity or transit observations.

A clear failing of my results is in the formation of super-Earths and Neptune-mass bodies. One reason for this appears to be the gas accretion routine that I have adopted, that allows planets to accrete gas once their masses exceed 3 $M_\oplus$. An additional issue is the adoption of atmosphere-induced enhanced capture radii for planetesimal accretion onto protoplanets. The very rapid growth of planets due to this often causes them to migrate rapidly toward the central star, an outcome that is reduced in models where enhanced capture radii are not included.

3.5 Discussion and Conclusions

Although the models presented in this study include a broad range of physical processes relevant to planet formation (migration; planetary growth through mutual protoplanet collisions; accretion of planetesimals and gas; planet-planet gravitational interactions), I have adopted a number of assumptions and simplifications that inevitably affect the realism of the simulations and their results.

These include:

1. *Simulation domain.* Even though I have modelled a relatively wide semi-major axis domain with my initial solid matter disc compared to previous N-body work on planetary formation, it is clear that accurate modelling of discs in which significant corotation torques arise requires as wide a domain as possible. Protoplanets move significantly in the disc with some forming at 2 - 3 AU and migrating out to 70 - 80 AU. Similarly, planets migrate inward and ought to traverse the terrestrial planet region which I have not modelled. Planets forming in the terrestrial region might also migrate out into the regions that I have investigated. In short, the migration behaviour observed in the simulations presented in this paper indicates that all regions of the disc are coupled during planet formation, and it is no longer sensible to think in terms of a "terrestrial planet region" or a "giant planet region". As such, a suitable model would involve a domain ranging from as far in as 0.1 AU out to approximately 50 AU. Such a simulation is beyond current modelling techniques because of the required numbers of protoplanets and planetesimals, even for the method presented by McNeil and Nelson [2009, 2010] which utilises multiple time steps in a parallel symplectic integrator. Instead, such global models of planetary formation are probably going to require efficient use of modern GPU technology. In the study documented in chapter 4, I have extended the region initially populated by solid material to cover 1-20 AU but the inner edge of the simulation is at only 0.15 AU in order to try to address this shortcoming.

2. *Gas disc model.* I currently model the gas disc as having fixed power-laws in surface density and temperature, with the disc mass undergoing exponential decay to mimic its viscous and photo evaporative evolution. In reality, the disc is heated by the central star and through local viscous dissipation, and it cools through radiative emission. A significant improvement to the model that has been implemented in my study documented in chapter 4 is a model that evolves the disc surface density and temperature explicitly using a 1D numerical solution. This approach is similar to that described in Fogg and Nelson [2009] and references therein, and allows gap formation and type II

migration to be simulated directly, along with UV photoevaporation of the disc during its final stages of dispersal.

3. *Planetary atmosphere model and enhanced capture radii.* As described in the preceding sections, rapid planetary growth is assisted by the enhanced accretion of planetesimals through implementation of a model for planetary atmospheres that increases the effective accretion cross section [Inaba and Ikoma, 2003]. Although this model works well when accretion is dominated by planetesimals, it is probably inaccurate when accretion includes giant impacts between protoplanets. In particular, a planetary atmosphere can be completely liberated from a planet when it is impacted by a body whose mass is similar to that of the atmosphere, and my implementation of the atmosphere model does not account for this effect. The atmosphere model would clearly be improved in its accuracy if it responded to giant impacts as well as planetesimal accretion rates.

4. *Gas envelope accretion.* My model for gas accretion during the formation of gas giants is very rudimentary, although it serves the purpose of allowing gas giant planets to form in my simulations. While a full accretion model for each planet similar to those presented in Pollack et al. [1996] and Movshovitz et al. [2010] would be ideal, this is computationally beyond the reaches of an N-body code that can model planetary systems formation over Myr time scales. However, there are improvements that can be made that will allow local conditions in the disc to influence the gas accretion rate onto a planet. Coupled with a more sophisticated disc model that allows explicit modelling of gap formation and gas accretion, such an approach would alleviate the requirement to set an artificial upper limit for the planet mass that can form through runaway gas accretion. Such modifications are included in my study documented in chapter 4.

I have presented the results of simulations that include recent torque formulae for type I migration (including Lindblad and corotation torques), with gas envelope accretion, enhanced capture radii due to gas atmospheres, and planet-planet gravitational dynamics included. I have surveyed a range of disc models which

all allow for outward migration driven by corotation torques. The main results that I have obtained may be summarised as follows:

- Convergent migration of protoplanets, and the rapid accretion of planetesimals, can cause the rapid growth of planetary cores to masses in excess of 10 $M_\oplus$ within 0.5 Myr in most disc models. This leads to rapid inward migration of these bodies, driven by Lindblad torques, when the horseshoe libration time scale becomes significantly shorter than the thermal/viscous diffusion time scale and the corotation torques saturate.

- Formation of planetary cores with a few Earth masses ≥ 0.5 Myr after the simulations are initiated can lead to their migration into the outer regions of the disc (30 - 50 AU). Steady mass growth through gas accretion onto the planet can counterbalance the slow inward migration that occurs as the gas disc mass reduces, and long-term survival in the outer disc can lead to gas giant planet formation there when runaway gas accretion ensues. This mode of giant planet formation was found to be a common outcome in my simulations, especially those with disc models that generate strong outward migration, leading to numerous gas giant planets being formed between semimajor axes 10 - 60 AU. Models such as these could potentially explain the long-period giant planets discovered recently through direct imaging [Kalas et al., 2008; Lagrange et al., 2010; Marois et al., 2010].

- Out of 40 simulations that used disc models whose masses were either 3 or 5 times more massive than the MMSN, 19 gas giant planets were formed. Most of these are similar in mass to Jupiter (in part because of the gas accretion prescription that was adopted in the models), and are formed at large distances from the star. Short period Jovian mass planets were also formed, however, along with a pair of Saturn-mass bodies at intermediate (~ 1 AU) orbit distances. These latter systems were formed in discs that generate weaker corotation torques than those that tend to generate the longer-period giant planets.

- Multiplanet systems containing more than one giant planet were found to be a rare outcome (3 out of 40 simulations produced two giant planets

each), and this has the additional effect of producing systems with very small eccentricities and inclinations due to the low rate of occurrence of planet-planet scattering events. In fact, the only planets to be formed with significant eccentricities were a pair of closely separated Jovian-mass objects that underwent significant dynamical interaction.

- My simulations completely fail to produce super-Earth or Neptune-mass planets. This appears to arise because of very rapid inward migration of planets that grow early in the disc lifetime and undergo rapid inward migration, combined with the switching-on of gas accretion that converts planets of intermediate mass into gas giants at later times. Modification of the planetary atmosphere and gas accretion prescriptions will probably result in more surviving planets with intermediate masses. Numerous planets in the Earth mass range were formed in the simulations, however. The 'desert' of super-Earths and Neptunes is similar to that reported in the planetary population synthesis models of Ida et al. [2008], and occurs for much the same reasons as theirs (rapid gas accretion and migration).

- Simulations performed where the corotation torque is attenuated when planet eccentricities grow to become larger than the dimensionless horseshoe width appear to produce results quite different from those in which this effect is neglected (i.e. all the runs described above). In particular the growth and survival of planets is reduced because mutual encounters between protoplanets maintains the typical eccentricities above the critical value for which corotation torques diminish. In these latter simulations, no gas giant planets were formed at all. Further work is required to establish the influence of corotation torques on planet formation *via* oligarchic growth, where planet-planet interactions maintain finite values of the eccentricity.

Chapter 4

N-body and 1D Disc Models Combined

4.1 Model Description

In the following section and subsections I give details about the physics of my model, the numerical methods I have used and modifications and improvements over the work done in the previous chapter.

In my previous study, the disc was modelled with a very simplistic approach. The local surface density in the disc was calculated as being

$$\Sigma_{\text{g}}(R, t) = \Sigma_{\text{g}}\left(1\,\text{AU}\right)\left(\frac{R}{1\,\text{AU}}\right)^{-\alpha}\exp\left(-t/\tau_{\text{disc}}\right) \tag{4.1}$$

and the temperature in the disc was taken to be

$$T(R) = T\left(1\,\text{AU}\right)\left(\frac{R}{1\,\text{AU}}\right)^{-\beta}. \tag{4.2}$$

I defined α and β to be within a range of values that allowed the potential for outward migration due to horseshoe torques. Gas planet accretion was independent of the local surface density although accretion was limited in the runaway phase to an estimate of the total amount of gas mass in the local feeding zone, the gas isolation mass (equation 3.25) or a Jovian mass, whichever was smaller. Accretion after this was set by the rate at which viscosity could supply gas from

92

the disc.

4.1.1 Finite differencing model

In this study, the complexity of the gas disc model is substantially improved by modelling the local surface density in detail throughout the disc. The surface density of an accretion disc can be modelled using the 1D diffusion equation Pringle [1981],

$$\frac{d\Sigma}{dt} = \frac{1}{r}\frac{d}{dr}\left(3r^{1/2}\frac{d}{dr}\left(\nu\Sigma r^{1/2}\right)\right). \tag{4.3}$$

Here r is the radial distance from the central star, ν is the viscosity and t is time.

In order to solve this computationally in my model, I split the disc into a number of concentric rings of equal thickness and utilise a finite differencing method to model the grid cells.

Rewriting 4.3 with $A = \nu\Sigma r^{1/2}$, I get

$$\frac{d\Sigma}{dt} = \frac{3}{r}\frac{d}{dr}\left(r^{1/2}\frac{dA}{dr}\right) \tag{4.4}$$

which can be expanded as

$$\frac{d\Sigma}{dt} = \frac{3}{2}r^{-3/2}\frac{dA}{dr} + 3r^{-1/2}\frac{d^2A}{dr^2}. \tag{4.5}$$

Approximating this so that it uses finite differences instead of derivatives yields

$$\Sigma_{t+1} = \Sigma_t + \Delta t\left(\frac{3}{2}r^{-3/2}\frac{dA}{dr} + 3r^{-1/2}\frac{d^2A}{dr^2}\right) \tag{4.6}$$

where Σ_{t+1} is the surface density at a very small time Δt after Σ_t.

The first derivative of A is given by

$$\frac{dA}{dr} \approx \frac{A_{i+1} - A_i}{\Delta r} \tag{4.7}$$

or

$$\frac{dA}{dr} \approx \frac{A_i - A_{i-1}}{\Delta r} \tag{4.8}$$

depending on whether forward or backward differencing is used i.e. for upwind or downwind derivatives which is dependent on which direction material in the disc is flowing. Here i is the grid cell number.

The second differential of A is given by

$$\frac{d^2 A}{dr^2} \approx \frac{A_{i+1} - 2A_i + A_{i-1}}{(\Delta r)^2}. \tag{4.9}$$

Up until now, this finite differencing method has not included the effects of planets within the disc. As discussed in section 3.1.5, large enough planets can clear a gap in the disc. Such gap clearing planets apply a torque to the disc and conversely, the disc applies a torque to the planet which causes the planet to migrate [Lin and Papaloizou, 1986].

The 1D model for the gas disc is assumed to be circular symmetric. Allowing this to remain the case for discs that are perturbed by a planet (which is reasonable as the viscous evolution timescale of the disc is significantly longer than the timescale for a planet's orbit), then we can modify equation 4.3 to include this torque, yielding

$$\frac{d\Sigma}{dt} = \frac{1}{r}\frac{d}{dr}\left(3r^{1/2}\frac{d}{dr}\left(\nu\Sigma r^{1/2}\right) - \frac{2\Lambda\Sigma r^{3/2}}{(GM_\odot)}\right) \tag{4.10}$$

where Λ is the disc/planet torque and is given by

$$\Lambda(r) = \begin{cases} \frac{r - R_p}{|r - R_p|}\frac{q^2 GM_\odot}{2r}\left(\frac{r}{|\Delta p|}\right)^4, & \text{if } |r - R_p| > h, \\ \frac{r - R_p}{h}\frac{q^2 GM_\odot}{2r}\left(\frac{r}{|\Delta p|}\right)^4, & \text{if } |r - R_p| \leq h. \end{cases} \tag{4.11}$$

Here q is the ratio of planet mass versus the mass of the central star, R_p is the distance from the central star to the planet and $|\Delta p|$ is given by

$$|\Delta p| = max\left(h, r - R_p\right) \tag{4.12}$$

and is a measure of the distance that a planet has influence over. The two forms

for Λ allows the equation to be continuous at $r = R_{\mathrm{p}}$.

Rewriting 4.12 with $B = \frac{2\Lambda\Sigma r^{3/2}}{(GM_\odot)}$ lets us write a new diffusion equation,

$$\Sigma_{\mathrm{t+1}} = \Sigma_{\mathrm{t}} + \Delta t \left(\frac{3}{2} r^{-3/2} \frac{dA}{dr} + 3 r^{-1/2} \frac{d^2 A}{dr^2} - \frac{1}{r} \frac{dB}{dr} \right). \tag{4.13}$$

The derivatives of B are given by

$$\frac{dB}{dr} \approx \frac{B_{\mathrm{i+1}} - B_{\mathrm{i}}}{\Delta r} \tag{4.14}$$

or

$$\frac{dB}{dr} \approx \frac{B_{\mathrm{i}} - B_{\mathrm{i-1}}}{\Delta r} \tag{4.15}$$

depending on forward or backward differencing.

4.1.1.1 Boundary conditions and time step size calculation

The boundary conditions of the model are set such that material in the inner most grid cell is removed and considered to be accreted by the central star and the radial velocity of the outermost grid cell is set to zero.

The time step for each grid cell is calculated as the minimum between the time step for a steady state disc,

$$\Delta t_{\mathrm{steadystate}} = \frac{2}{3} \frac{r}{\nu} \Delta r \tag{4.16}$$

and that due to the diffusion equation, 4.13,

$$\Delta t_{\mathrm{diffusion}} = \frac{\Delta r}{2\Lambda \sqrt{\frac{r}{GM_\odot}} - 3\frac{dA}{dr} (r\Sigma)^{-1/2}}. \tag{4.17}$$

4.1.1.2 Finding the temperature

The thermodynamics of a disc can be given by the steady state equation [D'Angelo and Marzari, 2012],

$$Q_\nu + Q_{\mathrm{irr}} - Q_{\mathrm{cool}} = 0, \tag{4.18}$$

where Q_ν is the viscous heating, Q_{irr} is the radiative heating of the disc by the central star and Q_{cool} is the radiative cooling of the disc.

The energy flux due to viscous dissipation is given by Mihalas and Weibel Mihalas [1984] as

$$Q_\nu = \nu \Sigma \left(\frac{d\Omega}{dr} \right)^2 . \tag{4.19}$$

In the case of a Keplerian rotating disc as is considered here, this becomes

$$Q_\nu = \frac{9}{4} \nu \Sigma \Omega^2, \tag{4.20}$$

giving the first term in equation 4.18.

The cooling related energy flux, Q_{cool} is given by [Hubeny, 1990]

$$Q_{\mathrm{cool}} = 2\sigma T^4 \left(\frac{3}{8} \tau_{\mathrm{R}} + \frac{1}{2} + \frac{1}{4\tau_{\mathrm{p}}} \right)^{-1} \tag{4.21}$$

where σ is the Stefan-Boltzmann constant, T is the mid plane temperature of the disc and τ_{R} and τ_{p} are the Rosseland and Planck mean opacities. This gives us the second term in 4.18. The factor of 2 is due to the disc having two sides that cool.

The energy flux related to the heating of the disc via stellar irradiation is given by

$$Q_{\mathrm{irr}} = 2\sigma T_{\mathrm{irr}}{}^4 \left(\frac{3}{8} \tau_{\mathrm{R}} + \frac{1}{2} + \frac{1}{4\tau_{\mathrm{p}}} \right)^{-1} \tag{4.22}$$

T_{irr} is the effective temperature caused by irradiation and, following Menou and Goodman [2004], is taken as

$$T_{\mathrm{irr}}^4 = T_{\mathrm{S}}^4 \left(1 - \epsilon \right) \left(\frac{R_{\mathrm{S}}}{r} \right)^2 W_{\mathrm{G}} \tag{4.23}$$

where ϵ is the disc's albedo, the fraction of energy reflected by the disc (taken here to be 0.5), T_{S} is the stellar temperature due to the internally generated luminosity of the star (taken to be 4280 Kelvin) and R_{S} is the radius of the star (taken to be 2 Solar radii). W_{G} is a geometrical factor that depends on how much

of the disc's surface is intercepting the emitted solar radiation, which depends on the vertical shape of the disc.

However, this is only true for a non-accreting star. In an accreting disc, this equation becomes [Hartmann et al., 2011]

$$T_{\text{irr}}^4 = \left(T_{\text{S}}^4 + T_{\text{acc}}^4\right)(1 - \epsilon)\left(\frac{R_{\text{S}}}{r}\right)^2 W_{\text{G}} \tag{4.24}$$

where T_{acc} is the effective temperature due to accretion. This can be estimated by considering the accretion luminosity,

$$L_{\text{acc}} = \frac{GM_{\text{S}}\dot{M}_{\text{S}}}{2R_{\text{S}}}, \tag{4.25}$$

where $\dot{M}_S$ is the accretion rate of material through the inner edge of the disc onto the star and is calculated as

$$\dot{M} = 2\pi R\Sigma v_{\text{r}}\left(R\right) \tag{4.26}$$

where R is the inner edge of the disc and $v_{\text{r}}\left(R\right)$ is the radial velocity at the inner edge. Using equation 4.25, we can obtain the accretion flux:

$$F_{\text{acc}} = \frac{GM_{\text{S}}\dot{M}_{\text{S}}}{8\pi R_{\text{S}}^3}. \tag{4.27}$$

This gives us the effective temperature due to accretion as:

$$T_{\text{acc}}^4 = \frac{GM_{\text{S}}\dot{M}_{\text{S}}}{8\pi R_{\text{S}}^3\sigma}. \tag{4.28}$$

The geometrical factor, W_{G} is given by Chiang and Goldreich [1997] as

$$W_{\text{G}} = 0.4\left(\frac{R_{\text{S}}}{r}\right) + \frac{H}{r}\left(\frac{\partial lnH}{\partial lnr} - 1\right) \tag{4.29}$$

where

$$\frac{\partial lnH}{\partial lnr} = \frac{r}{H}\frac{dH}{dr} \tag{4.30}$$

and H is the scale height of the disc. The first half of equation 4.29 is due to

illumination of the disc close to the star and the second term is for illumination far from the star. If disc geometry is such that it is self shadowing, then the second term is negative and should be dropped. For simplicity, I follow D'Angelo and Marzari [2012] and use the following approximation:

$$W_{\mathrm{G}} = 0.4 \left(\frac{R_{\mathrm{S}}}{r} \right) + \frac{H}{r} \frac{2}{7} \tag{4.31}$$

In order to find the temperature in each grid cell in the disc model, I use a bisection search method to solve equation 4.18 to find T. For the first time step, I use the mass accretion rate for a steady state disc in place of equation 4.26, which is given by:

$$\dot{M} = 3\pi\nu\Sigma. \tag{4.32}$$

4.1.1.3 Opacities

I use the Rosseland mean opacities for both the Rosseland and the Planck opacities for simplicity as these are comparable for the temperatures relevant to this work. As in section 3.1.1.2, I follow the Bell and Lin [1994] and Bell et al. [1997] prescriptions although I solve for each transition temperature this time to obtain

98

a more precise result.

$$\kappa[\text{cm}^2/\text{g}] = \begin{cases} 10^{-4}\,T^{2.1} & T < 132.39\,\text{K} \\ 3\,T^{-0.01} & 132.39\,\text{K} \leq T < 170.47\,\text{K} \\ 1^{-2}T^{1.1} & 170.47\,\text{K} \leq T < 377.16\,\text{K} \\ 5\times 10^4\,T^{-1.5} & 377.16\,\text{K} \leq T < 389.44\,\text{K} \\ 0.1\,T^{0.7} & 389.44\,\text{K} \leq T < 579.28\,\text{K} \\ 2\times 10^{15}\,T^{-5.2} & 579.28\,\text{K} \leq T < 681.29\,\text{K} \\ 0.02\,T^{0.8} & 681.29\,\text{K} \leq T < T_{\text{crossover},1} \\ 2\times 10^{81}\,\rho\,T^{-24} & T_{\text{crossover},1} \leq T < T_{\text{crossover},2} \\ 10^{-8}\,\rho^{2/3}\,T^3 & T_{\text{crossover},2} \leq T < T_{\text{crossover},3} \\ 10^{-36}\,\rho^{1/3}\,T^{10} & T_{\text{crossover},3} \leq T < 10000\,\text{K} \end{cases} \tag{4.33}$$

The last three crossover temperatures, $T_{\text{crossover},1-3}$, are dependent on the local gas density, which evolves throughout the simulation and so cannot be pre-calculated. They are calculated during the simulation using the local gas density as:

$$\begin{aligned} T_{\text{crossover},1} &= \left(1\times 10^{83}\rho\right)^{1/24.8} \\ T_{\text{crossover},2} &= \left(5\times 10^{-90}\rho^{-1/3}\right)^{-1/27} \\ T_{\text{crossover},3} &= \left(1\times 10^{28}\rho^{-1/3}\right)^{-1/7} \end{aligned} \tag{4.34}$$

The nature of this equation for opacity is illustrated in figure 4.1 where ρ has been taken to be 1×10^{-9} gcm^{-1}.

4.1.1.4 Disc solid component

The disc solid component is composed, as in chapter 3, initially of protoplanets and planetesimals where the planetesimals are modelled as super-planetesimals with a much larger mass than typical planetesimals but with an effective radius
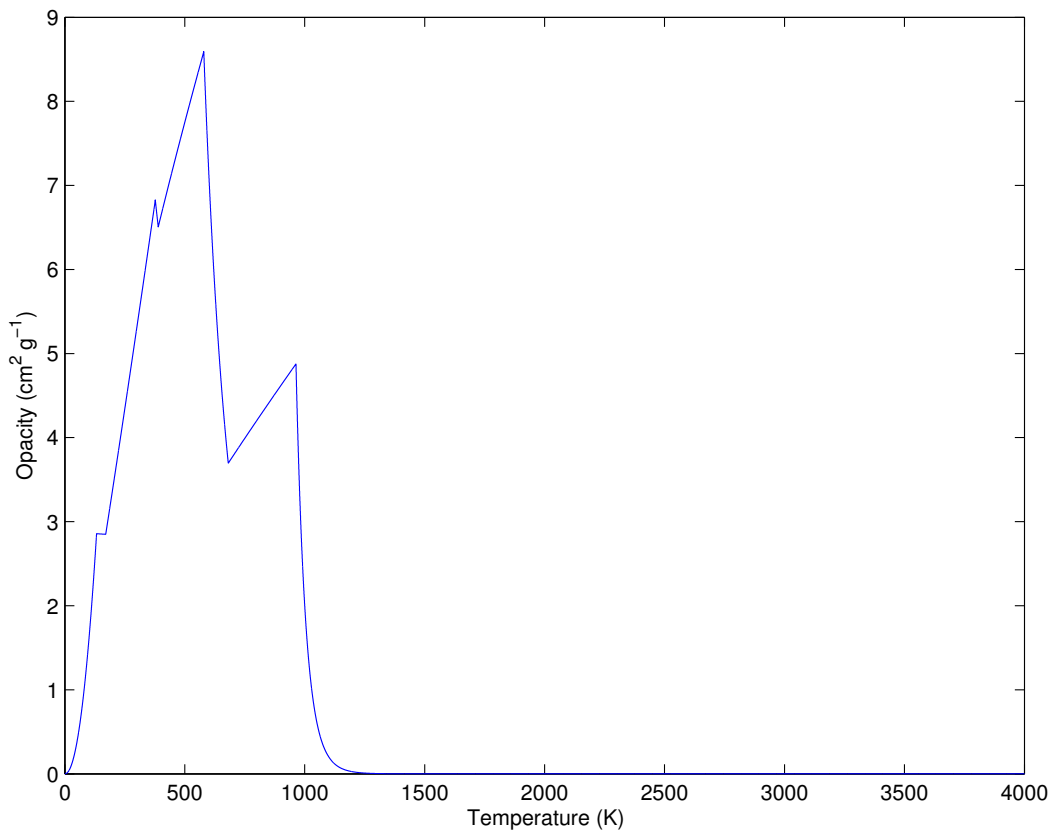
Figure 4.1: The Bell Rosseland mean opacity function illustrated against temperature. The gas density for the purpose of this plot was taken to be 1×10^{-9} gcm^{-1}.

of a realistic planetesimal (1 or 10 km) so that they experience the appropriate gas drag force.

Protoplanets are initially spaced by 10 mutual Hill radii and planetesimals are scattered throughout the disc such that the total solids content follows the surface density power law prescribed for the gaseous component. As in Thommes et al. [2003], planetesimals are distributed according to a Rayleigh distribution and have RMS values of the eccentricity $e = 0.01$ and inclination $i = 0.005$ radians, respectively.

The surface density of solids is enhanced beyond the snow line, whose position R_{snow} is determined by the location where the temperature falls below 170 K. The snow line discontinuity is spread over a distance ~ 1 AU:

$$\Sigma_{\mathrm{s},0}(R) = \left\{ \Sigma_1 + (\Sigma_2 - \Sigma_1) \left[\frac{1}{2} \left(\frac{R - R_{\mathrm{snow}}}{0.5\,\mathrm{AU}} \right) + \frac{1}{2} \right] \right\} \left(\frac{R}{1\,\mathrm{AU}} \right)^{-\alpha} \qquad (4.35)$$

I set the surface density enhancement due to the snowline to $(\Sigma_2/\Sigma_1) = 30/7.1$ as in Thommes et al. [2003]. Planetesimal densities are set at 3 g/cm^3 throughout the disk. Protoplanet densities are set at 3 g/cm^3 inside the snowline and 1.5 g/cm^3 beyond, as defined by Thommes et al. [2003]. The mass of the protoplanets at $t = 0$ is $m_{\mathrm{p}} = 0.02$ M$_\oplus$, and the mass of the superplanetesimals is 0.002 M$_\oplus$.

As the location of the snow line is dependent on the radial temperature in the disc, which is no longer defined simply by a power law function as in chapter 3, I first evolve the gas component of the disc for one time step so as to calculate the initial temperatures throughout the disc according the method described in section 4.1.1.2. This gives me the initial location of the snow line and allows me to generate the solid component of the disc appropriately.

4.1.2 Disc photoevaporation

At the surface of a protoplanetary disc, the temperature can become very high due to absorption of stellar radiation such that the gas temperature can exceed that of the local dust temperature. The warm gas at the surface can then flow off the disc and escape the star and disc's gravity [Dullemond et al., 2007]. The

rate at which photoevaporation removes gas mass from the protoplanetary disc is

$$\frac{d\Sigma}{dt} = 1.16 \times 10^{-11} G_{\text{fact}} \sqrt{f_{41}} \left(\frac{1}{r - r_{\text{g}}} \right)^{3/2} \left(\frac{M_{\odot}}{\text{AU}^2 \text{yr}} \right) \qquad (4.36)$$

where G_{fact} is a scaling factor and is defined as

$$G_{\text{fact}} = \begin{cases} \left(\dfrac{r_{\text{g}}}{r} \right)^2 e^{0.5(1-(r-r_{\text{g}}))} & r \leq (r - r_{\text{g}}), \\ \left(\dfrac{r_{\text{g}}}{r} \right)^{5/2} & r > (r - r_{\text{g}}), \end{cases} \qquad (4.37)$$

Here r_{g} is the radius beyond which gas is unbound which I set this value to 10 AU and f_{41} is the rate of extreme ultraviolet ionising photons emitted by the star in units of 10^{41} s^{-1}.

4.2 Updates to migration model

As in chapter 3, I incorporate the Paardekooper et al. [2011] torques (equation 2.26),

$$\begin{aligned} \Gamma_{\text{tot}} = \quad & \Gamma_{\text{LR}} + \Gamma_{\text{VHS}} F_{\text{v}} G_{\text{v}} + \Gamma_{\text{EHS}} F_{\text{v}} F_{\text{d}} \sqrt{G_{\text{v}} G_{\text{d}}} \\ + \quad & \Gamma_{\text{LVCT}} (1 - K_{\text{v}}) + \Gamma_{\text{LECT}} (1 - K_{\text{v}})(1 - K_{\text{d}}). \end{aligned} \qquad (2.26)$$

However, as I now model the disc via a series of cells and allow the disc surface density and temperature to change, the overall surface density and temperature profiles (α and β) are no longer constant. These values are used in the component torques in equation 2.26. Instead, I calculate the local surface density and temperature profiles by averaging out the profiles in each grid cell over a distance of each planet's horseshoe width, x_{s} given by equation 3.13 or three cells width, whichever is greater.

4.2.0.1 Eccentricity and inclination reduction factor

In the previous study, I performed some runs where I included an eccentricity cutoff factor for the co-rotational torque, following work by [Bitsch and Kley, 2010]. Effectively, planets on eccentric orbits move radially inside and out of the

horseshoe region in a disc as the horseshoe regions are circular in the disc. The horseshoe regions become smaller due to the gravitational field of an eccentric planet being weakened, reducing the effective planet mass. These runs showed that high eccentricities led to a shutdown of the co-rotational torques which negates the outward migration. However, I did not previously include the effect of inclination induced reduction of corotation torques. Inclined planets spend some of their orbits towards the upper and lower surface of the gas disc where the gas is more tenuous which has the result that over their orbit they interact with less of the gas material. Furthermore, when planets are at such locations, they are further away from the bulk mass of the disc. In order to include such effects in this updated model, I use the following torque equation:

$$
\begin{aligned}
\Gamma_{\text{tot}} \;=\;& E_i\Gamma_{\text{LR}} + \Big\{\Gamma_{\text{VHS}}F_{\text{v}}G_{\text{v}} + \Gamma_{\text{EHS}}F_{\text{v}}F_{\text{d}}\sqrt{G_{\text{v}}G_{\text{d}}} \\
+\;& \Gamma_{\text{LVCT}}(1 - K_{\text{v}}) + \Gamma_{\text{LECT}}(1 - K_{\text{v}})(1 - K_{\text{d}})\Big\} E_e
\end{aligned}
\tag{4.38}
$$

The factor E_e is an updated version of the previous study's E term and represents the attenuation of the corotation torques due to both eccentricity and inclination driven radial and vertical excursions that exceed the width of the horseshoe region and the disc height respectively. I define E_{e} as

$$
E_{\text{e}} = (1 - \tanh{(e/x_{\text{s}})})(1 - \tanh{(i/h)}).
\tag{4.39}
$$

where x_{s} is the dimensionless horseshoe width given by equation 3.13, h is the disc thickness ($H = h/r$) and the inclination is in radians.

The factor E_{i} in equation 4.39 corresponds to the reduction in efficacy of the Lindblad torques when planets are on eccentric and/or inclined orbits [Cresswell and Nelson, 2008]. At apocentre an eccentric planet can move slower than the surrounding gas material which means that this gas material is pulled around and focused by the gravity of a planet giving yield to a high density region that leads the planet and a positive torque. At pericentre the opposite occurs, local gas material is slower, so material is bent behind a planet's orbit which pulls the planet back, producing a negative torque. The sum total of these torques depends on the local surface densities at pericentre and apocentre and typically

this will lead to a reversal of the Lindblad torques.

E_i is defined following [Cresswell and Nelson, 2008] as:

$$E_i = \left[P(e) + \left(\frac{P(e)}{|P(e)|} \right) \times \left\{ 0.070 \left(\frac{i}{h} \right) + 0.085 \left(\frac{i}{h} \right)^4 - 0.080 \left(\frac{e}{h} \right) \left(\frac{i}{h} \right)^2 \right\} \right]^{-1}$$
(4.40)

where $P(e)$ is defined as:

$$P(e) = \frac{1 + \left(\frac{e}{2.25h} \right)^{1/2} + \left(\frac{e}{2.84h} \right)^6}{1 - \left(\frac{e}{2.02h} \right)^4}$$
(4.41)

4.2.1 Type II-Migration

The torques for type II viscous driven migration are now calculated within the disc model with equation 4.11. However, the perturbations that low mass planets apply to the surface density in a disc are carried away by spiral density waves which are locally damped so I limit the ability of planets to perturb the disc until their mass is such that they are considered to be gap forming.

A planet is considered to be gap forming if it can satisfy two criteria. The first is that the spiral waves generated by a planet's interaction with a disc become non-linear. I take the criterion for this switchover to be

$$\left(\frac{M_p}{M_\odot} \right)^{1/3} \left(\frac{H}{a_p} \right)^{-1} > 0.72$$
(4.42)

where M_p and a_p are a planet's mass and semi-major axis respectively. This is calibrated so that for an $H/R = 0.05$ disc, the switchover mass is 30 Earth masses.

The second criterion for gap formation is that a planet needs to exert a torque on the disc that exceeds the viscous torque. For this, I take

$$\left(\frac{M_p}{M_\odot} \right) > 40\nu \left(\frac{H}{a_p} \right)^2.$$
(4.43)

As both criteria need to be satisfied in order for gap formation and thus switchover to type II migration to occur, the switchover mass for a given planet

is

$$M_{\text{p,switch}} = max\left(40\nu\left(\frac{H}{a_{\text{p}}}\right)^2 M_\odot, 0.72^3\left(\frac{H}{a_{\text{p}}}\right)^3 M_\odot\right). \qquad (4.44)$$

Once a planet's switchover mass is reached, the switchover mass is locked down (as it varies over time) and type I migration is switched off gradually over a 5 Earth mass range following:

$$0.5 - 0.5 * tanh\left(\frac{(M_{\text{p}}/M_\oplus) - (M_{\text{p,switch}}/M_\oplus) + 2.5}{1.5}\right). \qquad (4.45)$$

4.2.2   Gas Accretion Model

Once a protoplanet has accreted enough planetesimals such that it is large enough to begin accreting gas from the disc (a limit I set to be 3 Earth masses as in chapter 3), I allow a planet to accrete mass following my approximation to the growth demonstrated in Movshovitz et al. [2010] (equation 3.20).

I allow this to continue until the runaway gas accretion phase, which occurs when a planet's gas mass is approximately equivalent to its solid mass. I take this to occur when a planet's total mass is 30 Earth masses.

4.2.2.1   Viscous evolution driven accretion

Once a planet is sufficiently massive so as to allow runaway gas accretion, I switch to a viscous driven gas accretion model. At this point, a planet is assumed to have created a circum*planetary* accretion disc from which the planet accretes mass. I set the mass accretion rate to be

$$\frac{dM_{\text{p}}}{dt} = \frac{M_{\text{ad}}}{\tau_{\nu_{\text{p}}}} \qquad (4.46)$$

where M_{ad} is the mass within a planet's accretion disc and $\tau_{\nu_{\text{p}}}$ is the viscous timescale for the planet's circumplanetary disc. I take the radius of a planet's accretion disc to be that of the planet's Hill sphere radius.

To calculate the mass in such a disc, I first evaluate the mass contained within the gap forming region around a planet. I specify that the gap forming region

around a planet in a disc consists of a ring extending a distance of

$$r_{\mathrm{gap}} = Q_{\mathrm{gap}} r_H \tag{4.47}$$

either side of the planet. Thus the mass within the gap forming region is

$$M_{\mathrm{gap}} = \int_{R_{\mathrm{p}} - r_{\mathrm{gap}}}^{R_{\mathrm{p}} + r_{\mathrm{gap}}} 2\pi r \Sigma\left(r\right) dr. \tag{4.48}$$

The parameter Q_{gap} specifies the width of the gap. I use a value of $Q_{\mathrm{gap}} = 3$ for my simulations as I found this to give good agreement with the physical gaps formed in the disc via the type II torques.

I then take the mass of a planet's accretion disc to be

$$M_{\mathrm{ad}} = 10 M_{\mathrm{gap}} F_{\mathrm{gap}} \tag{4.49}$$

where F_{gap} is the ratio of the accretion disc's area to that of the total gap area,

$$F_{\mathrm{gap}} = \frac{r_{\mathrm{gap}}^2}{\left(R_{\mathrm{p}} + r_{\mathrm{gap}}\right)^2 - \left(R_{\mathrm{p}} - r_{\mathrm{gap}}\right)^2}, \tag{4.50}$$

and the factor of 10 is due to the density enhancement that a planet's accretion disc would have over the background protoplanetary disc.

To obtain $\tau_{\nu_{\mathrm{p}}}$, the viscous timescale of the planet's accretion disc, I consider

$$\tau_{\nu_{\mathrm{p}}} = \frac{r_{\mathrm{ad}}^2}{\nu_{\mathrm{p}}}. \tag{4.51}$$

Here ν_{p} is the viscosity of the circumplanetary disc and is given by

$$\nu_{\mathrm{p}} = \alpha c_{\mathrm{s}}\left(R_{\mathrm{p}}\right) H_{\mathrm{ad}} \tag{4.52}$$

where α is the disc viscosity, $c_{\mathrm{s}}\left(R_{\mathrm{p}}\right)$ is the sound speed of the disc at the location of the planet and H_{ad} is the effective thickness of the circumplanetary disc at the edge of its radius. This is given by

$$H_{\mathrm{ad}} = \frac{r_{\mathrm{ad}} c_{\mathrm{s}}\left(R_{\mathrm{p}}\right)}{v_{\mathrm{ad}}} \tag{4.53}$$

where v_{ad} is the Keplerian velocity a distance of r_{gap} around the planet which is

given by

$$v_{\mathrm{ad}} = \sqrt{\frac{GM_{\mathrm{p}}}{r_{\mathrm{ad}}}}. \tag{4.54}$$

Putting these together, we obtain the viscous timescale of the planet's accretion disc,

$$\tau_{\nu_{\mathrm{p}}} = \frac{r_{\mathrm{ad}} v_{\mathrm{ad}}}{\alpha c_{\mathrm{s}}^2 (R_{\mathrm{p}})} \tag{4.55}$$

and thus the mass accretion rate of a planet due to viscous evolution:

$$\frac{dM_{\mathrm{p}}}{dt} = \frac{M_{\mathrm{ad}} \alpha c_{\mathrm{s}}^2 (R_{\mathrm{p}})}{r_{\mathrm{ad}} v_{\mathrm{ad}}}. \tag{4.56}$$

4.2.2.2 Gas removal due to accretion

Both gas accretion regimes remove gas from the disc. To facilitate this, I remove mass from the disc up to a hill radius away from the planet, removing a greater proportion of mass from the planet's immediate vicinity. To do this, I spread the mass removal over the local area by using a spline function (Nelson and Papaloizou [1993] equation 30):

$$W(u, r_{\mathrm{h}}) = \frac{1}{\pi r_{\mathrm{h}}^3} \begin{cases} 1 - \frac{3}{2}\left(\frac{u}{r_{\mathrm{h}}}\right)^2 + \frac{3}{4}\left(\frac{u}{r_{\mathrm{h}}}\right)^3 & 0 \leq u/r_{\mathrm{h}} < 1 \\ \frac{1}{4}\left(2 - \left(\frac{u}{r_{\mathrm{h}}}\right)\right)^3 & 1 \leq u/r_{\mathrm{h}} < 2 \\ 0 & u/r_{\mathrm{h}} \geq 2 \end{cases} \tag{4.57}$$

where $u = |r - R_{\mathrm{p}}|$ is the separation between a grid cell and the accreting planet.

If there is insufficient mass in the accreting area to supply the mass specified by the gas accretion routines then gas driven accretion is halted.

4.2.3 Other features modelled

Eccentricity and inclination damping, planetesimal gas drag and enhanced capture radius due to nascent atmospheres on protoplanets are all calculated in the same manner as the study in chapter 3, modified to use the new disc model.

4.3 Initial Conditions

I performed my simulations again using the Mercury-6 symplectic integrator [Chambers, 1999], modified to include the physics described in chapter 2 and section 4.1 and also modified to include the finite differencing based disc model described in section 4.1.1.

As is usual in n-body models of planetary growth, I model my planetesimals as super-planetesimals that are a tenth (0.02 $M_\oplus$) of the initial mass of the protoplanets (0.2 $M_\oplus$) and assign them an effective radius of either 1 or 10 km. Rather than limit the run length time to a fixed duration as in my previous study where I ran simulations to 3 Myr in simulation time, I have allowed simulations to continue running over a period approximately two months in real time. The computational complexity scales with the disc mass size as the number of planetesimals is greater in heavier disc models. Using this approach, smaller mass discs have the opportunity to evolve further in the computational timescale I've had available.

In my suite of runs, I have included a range of disc masses (1 - 6 MMSN), two metallically factors (1, 2), two effective planetesimal size (1, 10 km) and three EUV photo-evaporation rates (1, 10, 100 10^{41} s^{-1}). To enable this broad coverage of parameters, I limited the number of realisations of initial conditions to two runs for each parameter choice, with each pair of realisations differing only by the random number seed used to determine the initial position of planetesimals.

As the surface density and temperature of the disc are no longer dependent on radial power laws, I initiate each disc according to the MMSN with an initial surface density power law of 3/2. The magnitude of the disc mass is multiplied depending on the disc mass and metallicity. The model self-calculates the temperature in the disc as described in section 4.1.1.2 and the surface density in the disc self-adjusts over approximately the first 100,000 yr to a self consistent state for the given disc mass and disc properties.

The solid component of the disc is spread out between 1 - 20 AU. This resulted in there being 41 protoplanets in each disc model and the number of planetesimals ranged from $\sim$ 1700 for a 1 times MMSN disc up to $\sim$ 12000 for a 6 times MMSN disc - the greater than 6 times enhancement in this number due to the snow line

location being further out in the disc.

The gas component of the disc is modelled in a series of rings 0.01 AU thick from 0.1 to 40 AU. The inner edge of my simulations is set at 0.015 AU such that any body that migrates inside this boundary is removed from the simulation. Information is stored for all planets that cross 0.75 AU where the expected computational accuracy begins to drop so that they can be extended in single body runs if necessary.

My simulation parameters are detailed in table 4.3.

4.4 Results

In this section I begin by describing the model and planet classification system I have used to group and evaluate my models and their results. I then describe the detailed evolution of a selection of individual runs (four runs in total) followed by a summary of results across all the simulations including final snapshots for each simulation.

4.4.1 Model and planet classifications

In terms of the simulation progression, I classify the results as 'early', 'intermediate' and 'late' stage runs. This has been necessary as, depending on the initial parameters, some runs have been able to evolve to a greater extent than others. More massive discs have a larger number of planetesimals which increases the computational complexity of simulations. Furthermore, since the minimum timescale necessary for disc computations to be accurate depends directly on the radial velocity of grid cells, simulations that have developed deep gaps have timesteps of up to two orders of magnitude smaller than without - this is particularly an issue with short period giant planets.

My simulations are thus classified as follows:

- *Early stage runs* are simulations that are relatively unevolved. They still have a large proportion of disc mass still present at the end of the run.

Table 4.1: Simulation parameters.

Simulation	f_{enh}	met	f_{41}	r_{pp}	M_{solid}	a_{snow}
P01A, P01B	1	1	1.00	10	42.36	2.73
P02A, P02B	2	1	1.00	10	84.42	3.68
P03A, P03B	3	1	1.00	10	126.5	4.39
P04A, P04B	4	1	1.00	10	168.7	4.97
P05A, P05B	5	1	1.00	10	210.8	5.47
P06A, P06B	6	1	1.00	10	252.8	5.92
P07A, P07B	1	2	1.00	10	84.42	3.17
P08A, P08B	2	2	1.00	10	168.8	4.27
P09A, P09B	3	2	1.00	10	253.0	5.09
P10A, P10B	1	1	10.0	10	42.36	2.73
P11A, P11B	2	1	10.0	10	84.42	3.68
P12A, P12B	3	1	10.0	10	126.5	4.39
P13A, P13B	4	1	10.0	10	168.7	4.97
P14A, P14B	5	1	10.0	10	210.8	5.47
P15A, P15B	6	1	10.0	10	252.8	5.92
P16A, P16B	1	2	10.0	10	84.42	3.17
P17A, P17B	2	2	10.0	10	168.8	4.27
P18A, P18B	3	2	10.0	10	253.0	5.09
P19A, P19B	1	1	100.	10	42.36	2.73
P20A, P20B	2	1	100.	10	84.42	3.68
P21B, P21B	3	1	100.	10	126.5	4.39
P22A, P22B	4	1	100.	10	168.7	4.97
P23A, P23B	5	1	100.	10	210.8	5.47
P24A, P24B	6	1	100.	10	252.8	5.92
P25A, P25B	1	2	100.	10	84.42	3.17
P26A, P26B	2	2	100.	10	168.8	4.27
P27A, P27B	3	2	100.	10	253.0	5.09
P28A, P28B	1	1	1.00	1.	42.36	2.73
P29A, P29B	2	1	1.00	1.	84.42	3.68
P30A, P30B	3	1	1.00	1.	126.5	4.39
P31A, P31B	4	1	1.00	1.	168.7	4.97
P32A, P32B	5	1	1.00	1.	210.8	5.47
P33A, P33B	6	1	1.00	1.	252.8	5.92
P34A, P34B	1	2	1.00	1.	84.42	3.17
P35A, P35B	2	2	1.00	1.	168.8	4.27
P36A, P36B	3	2	1.00	1.	253.0	5.09
P37A, P37B	1	1	10.0	1.	42.36	2.73
P38A, P38B	2	1	10.0	1.	84.42	3.68
P39A, P39B	3	1	10.0	1.	126.5	4.39
P40A, P40B	4	1	10.0	1.	168.7	4.97
P41A, P41B	5	1	10.0	1.	210.8	5.47
P42A, P42B	6	1	10.0	1.	252.8	5.92
P43A, P43B	1	2	10.0	1.	84.42	3.17
P44A, P44B	2	2	10.0	1.	168.8	4.27
P45A, P45B	3	2	10.0	1.	253.0	5.09
P46A, P46B	1	1	100.	1.	42.36	2.73
P47A, P47B	2	1	100.	1.	84.42	3.68
P48A, P48B	3	1	100.	1.	126.5	4.39
P49A, P49B	4	1	100.	1.	168.7	4.97
P50A, P50B	5	1	100.	1.	210.8	5.47
P51A, P51B	6	1	100.	1.	252.8	5.92
P52A, P52B	1	2	100.	1.	84.42	3.17
P53A, P53B	2	2	100.	1.	168.8	4.27
P54A, P54B	3	2	100.	1.	253.0	5.09

- *Intermediate stage runs* are simulations that have already lost the bulk of their gas mass and thus gas driven migration effects have less of an effect. I consider a system to have reached an intermediate stage when less than a half of the mass of an MMSN is present.

- *Late stage runs* are simulations where the gas disc has dissipated and evaporated and thus for the purpose of gas driven migration are considered 'complete'. I consider a system to have reached this stage once there is less than 100 Earth masses of nebula gas present.

Depending on the conditions within the disc when planets are formed, a wide variety of planets can be formed. When considering planets formed, I classify them into five groups:

- *Gas giant planets* have greater than 50% gas content and have a mass greater than 50 $M_\oplus$.

- *Gas planets* have greater than 50% gas content but with masses lower than 50 $M_\oplus$.

- *Neptune-like planets* have greater than 5% gas content but less than 50% gas content.

- *Super-earth planets* have masses greater than 2.5 $M_\oplus$ but gas content less than 5%.

- *Terrestrial planets* have masses greater than 0.75 $M_\oplus$ but lower than 2.5 $M_\oplus$.

4.4.2 Individual Runs

4.4.2.1 Run P02A

Run P02A has an initial disc mass equivalent to 2 times the MMSN. The disc metallicity factor is 1, the f_{41} EUV photoevaporation is 1 and the planetesimal size is 10 km. The initial solids distribution is shown in figure 4.2. Snapshots of the simulation conditions showing protoplanet locations, planetesimal surface
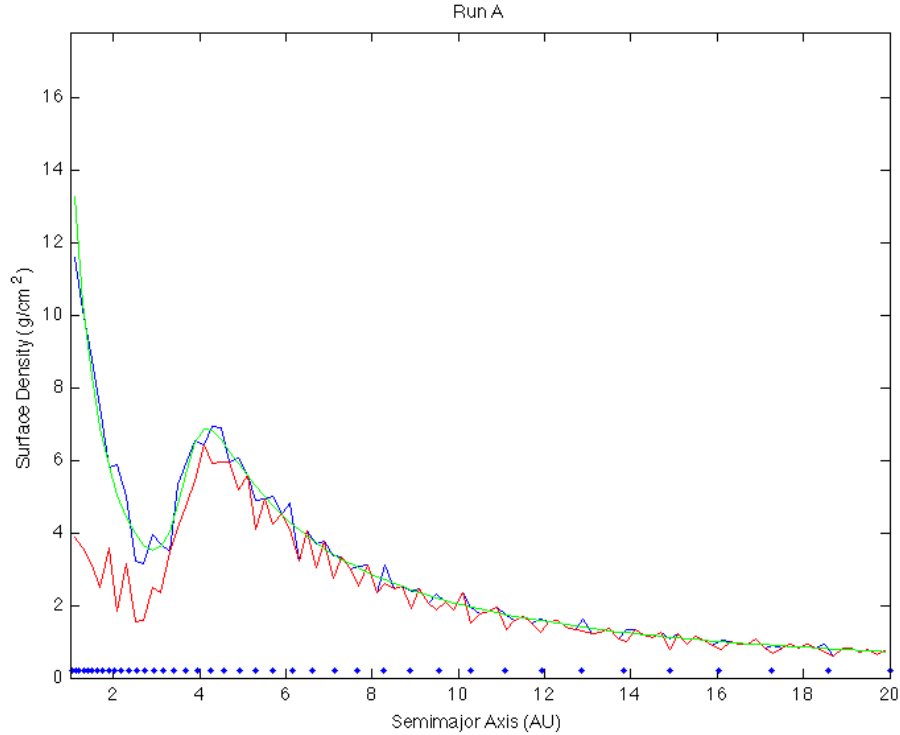
Figure 4.2: Initial solid body distribution for run P02A. The blue points mark the locations of the protoplanets, the red line denotes the planetesimal based surface density, the green line represents the target surface density for a disc of this size and the blue line represents the actual overall solids surface density.

density and gas disc surface density are shown in figure 4.3, disc temperature in figure 4.4 and torque magnitudes in figure 4.5. The time evolution of the planet masses, semi-major axes, eccentricities and inclinations for all the planets as well as the gas disc and planetesimal disc masses are shown in figure 4.6.

Mass growth as a result of planetesimal accretion and planet-planet inelastic collisions is initially slow as the solid disc mass is comparatively low. During the first 0.5 Myr, no planets greater than 1 Earth mass have formed and gas driven migration is not the driving factor for planetary motions due to its weak affect on small planets.

By 1.5 million years, the gas disc mass has halved. Some terrestrial sized
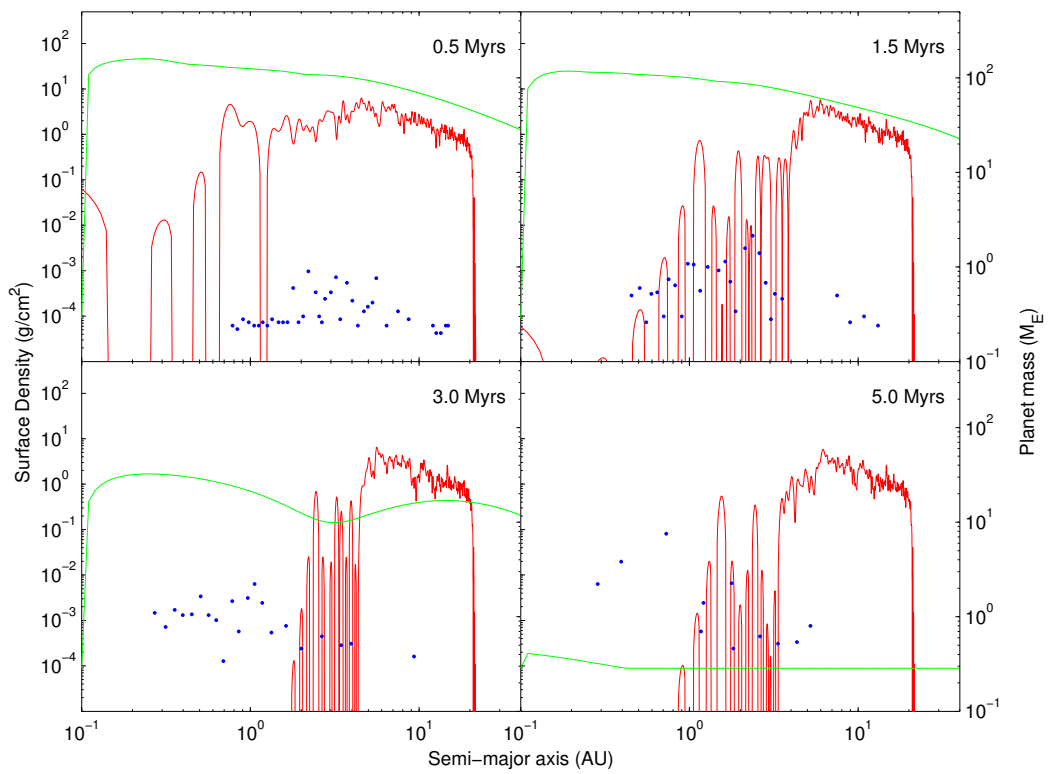
Figure 4.3: The locations and masses of the planets (blue dots) in run P02A plotted against the planetesimal (red line) and gas (green line) surface densities at various times. Plotted gas surface densities are reduced by a factor of 10 to allow concurrent plotting.
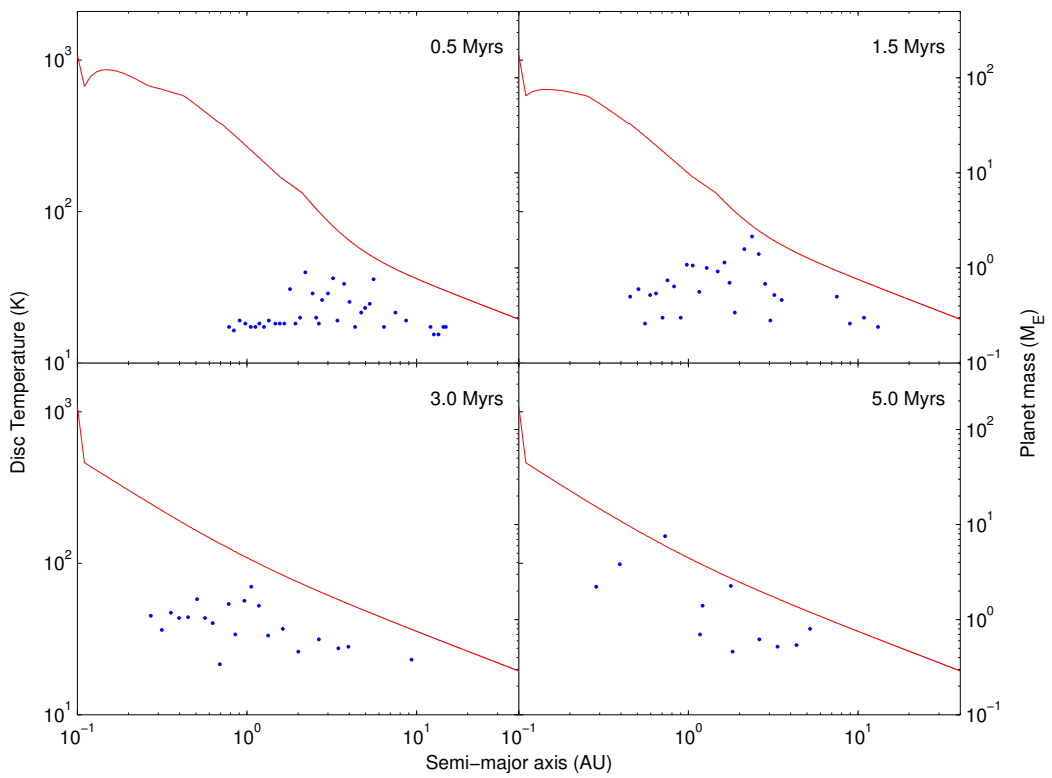
Figure 4.4: The locations and masses of the planets (blue dots) in run P02A plotted against the gas disc temperature (red line) at various times.
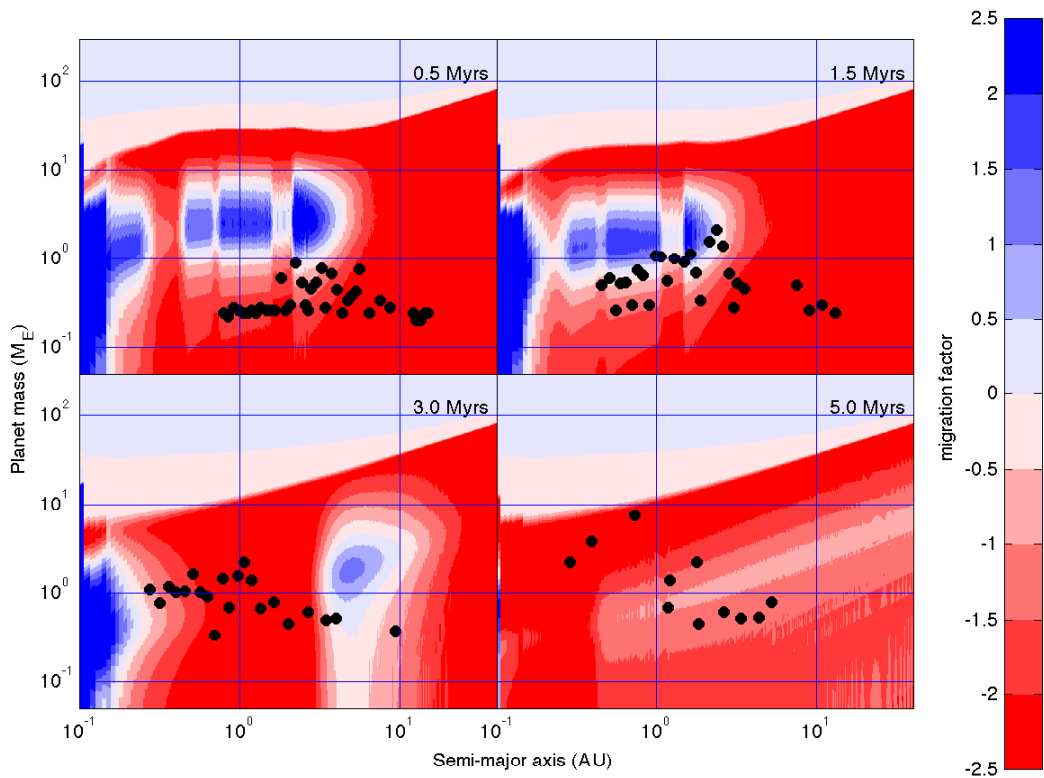
Figure 4.5: Contour plots showing regions of outward and inward migration for run P02A at various times. Regions of outward migration are shaded blue while regions of inward migration are shaded red. Planets are illustrated as black circles. Planets are illustrated as black circles.
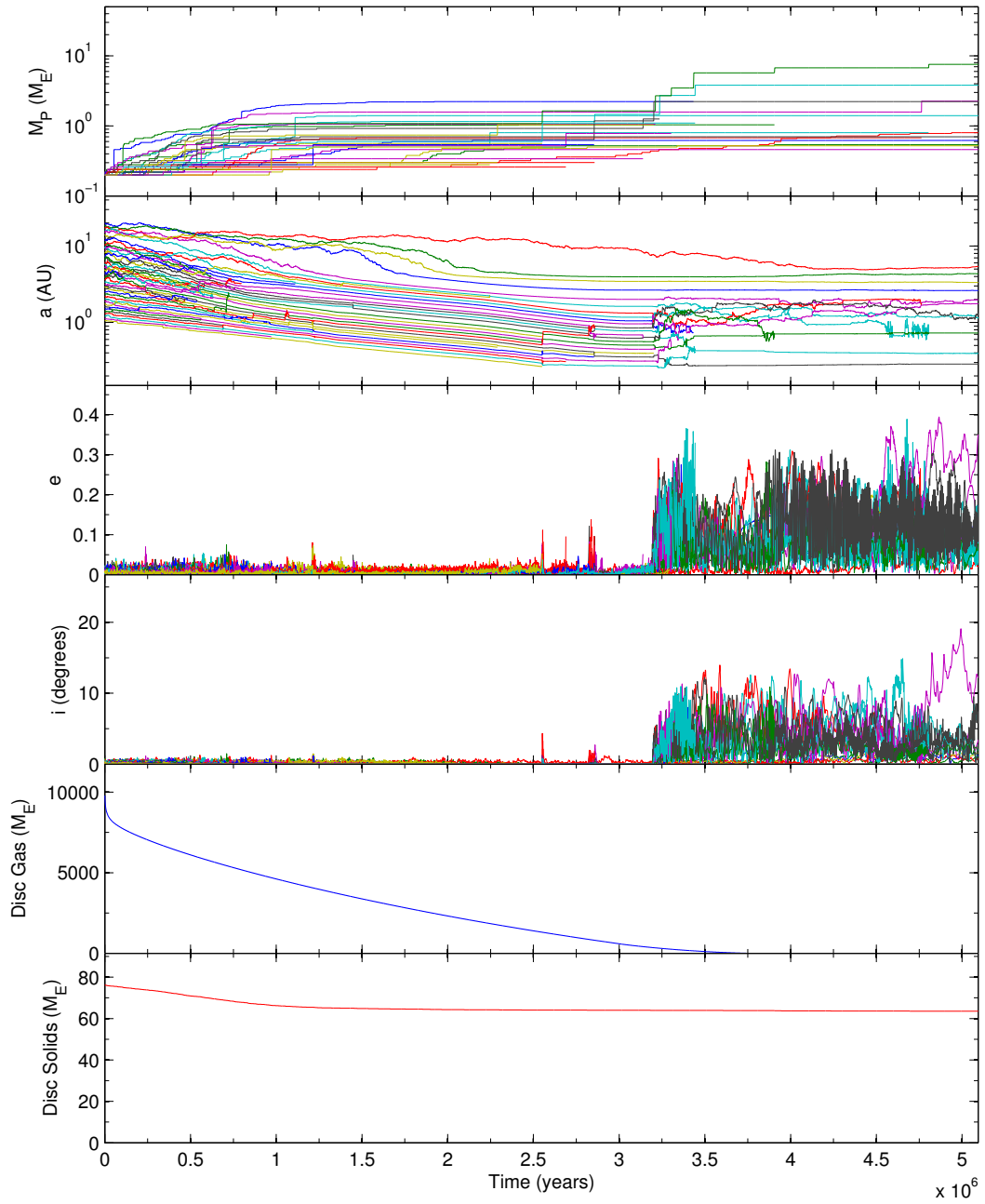
Figure 4.6: The evolution of masses, semimajor axes, eccentricities and inclinations for all protoplanets and the total gas disc mass and total planetesimal disc mass for simulation P02A.

planets have now formed and have moved so that they lie in areas of zero net torques. The reasoning for this was discussed in section 3.3.1.1 in chapter 3. For a given planet mass, there exist regions in the disc where the surface density and opacity allow the thermal and viscous diffusion times to be approximately equal to the horseshoe libration time thus giving a maximal value to the corotation torque - strong enough to overcome the Lindblad torques that drive inward migration. A planet in such a region will thus migrate outwards. However, as it does so, the surface density and opacity in the disc decreases so that there is a point where the corotation and Lindblad torques effectively cancel. Planets outside of such regions will tend to migrate inwards towards them and planets inside will tend to migrate outwards. In the contour plots presented in this study, this region corresponds to the terminus between blue and red areas where the blue area is inwards of a red area. This is observable in the top right plot in figure 4.5 where a number of bodies straddle this region.

These planets do not grow substantially over the following 1.5 million years but remain in areas of zero migration and move inwards as the gas disc dissipates which reduces the gas surface densities and opacities effectively moving the areas of zero migration inwards. By 3 million years, the disc has almost completely dissipated. Note the characteristic dip in disc surface density in the lower left plot of figure 4.3 due to the effect of photo-evaporation as seen in Dullemond et al. [2007]. This dip soon grows into a wide hole in the disc after which the remainder of the gas in the disc rapidly dissipates.

After the disc is completely dissipated (which occurs at approximately 3.25 Myr), planetary evolution is entirely driven by solid body interactions. Accretion is limited to planet-planet inelastic collisions and planetesimal accretion. As the eccentricities and inclinations of bodies can no longer be damped by the gas disc, a sharp increase in these quantities is observed from this point onwards.

This run failed to produce any gas giant or gas planets - indeed, as no planets grew larger than 3 $M_\oplus$ (i.e. the criterion I take above which gas accretion can occur) during the lifetime of the gas disc, none of the final planets have accreted any gas whatsoever. However, a number of terrestrial and super-earth type planets are formed with the largest being a super-Earth with a mass of 7.5 $M_\oplus$ located at 0.73 AU.

All remaining planets lie between 0.4 and 6.4 AU. There is still a large amount of solid material left in the disc in the form of planetesimals. A minority of this is left scattered amongst the formed planets suggesting the planets in this region will grow little in size over a long term evolution period. The outermost planets do lie in a planetesimal rich portion of the disc though and are likely to grow in size. Nevertheless, a dense disc of planetesimals remains between 3 and 20 AU. In reality, such a region is unlikely to form as once protoplanets have moved out of a dense planetesimal region, it is likely that the region would revert to a period of runaway solid body growth such that a fresh batch of protoplanets would emerge from the planetesimal swarm. As the gas disc has completely dissipated in this run, it is considered to be a late stage or completed run.

4.4.2.2 Run P06A

Run P06A has an initial disc mass equivalent to 6 times the MMSN. The disc metallicity factor is 1, the f_{41} EUV photoevaporation is 1 and the planetesimal size is 10 km. The initial solids distribution is shown in figure 4.7. Snapshots of the simulation conditions showing protoplanet locations, planetesimal surface density and gas disc surface density are shown in figure 4.8, disc temperature in figure 4.9 and torque magnitudes in figure 4.10. The time evolution of the planet masses, semi-major axes, eccentricities and inclinations for all the planets as well as the gas disc and planetesimal disc masses are shown in figure 4.11.

Initial growth progresses slightly faster in this model than in run P02A due to the tripling of solids disc mass. By 0.5 Myr, several planets are getting close to the outward migration region shown in figure 4.10. The convergent nature of these outward migration zones leads to the creation of two larger bodies of 4.2 and 6.6 $M_{\oplus}$ at 1.8 and 2.1 AU respectively. The larger and further out of these lies on a zero migration line while the inner planet is kept inside of its zero migration line due to the presence of the larger planet. These two planets are in a 4:5 resonance. They both accrete material slowly and move inwards as the zero migration area for the larger planet moves in with the disc dispersal until around 2 million years when the larger planet accretes enough mass to detach from its zero migration line. These planets then migrate inwards in a resonant convoy -

Figure 4.7: Initial solid body distribution for run P06A. The blue points mark the locations of the protoplanets, the red line denotes the planetesimal based surface density, the green line represents the target surface density for a disc of this size and the blue line represents the actual overall solids surface density.
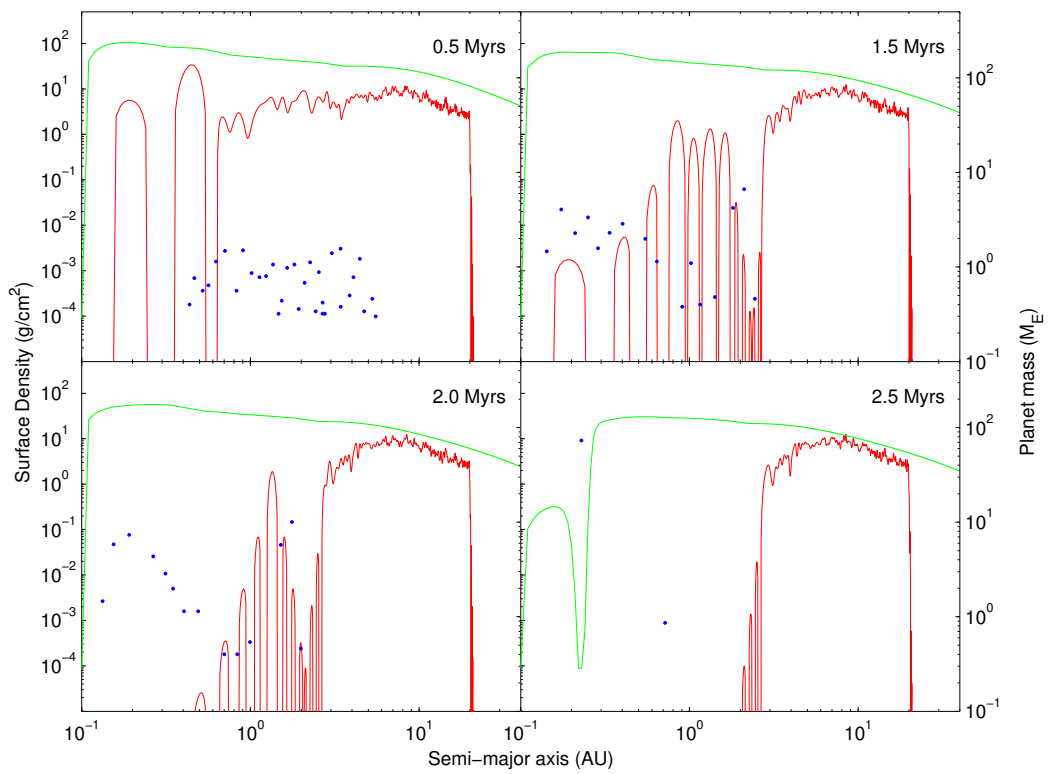
Figure 4.8: The locations and masses of the planets (blue dots) in run P06A plotted against the planetesimal (red line) and gas (green line) surface densities at various times. Plotted gas surface densities are reduced by a factor of 10 to allow concurrent plotting.
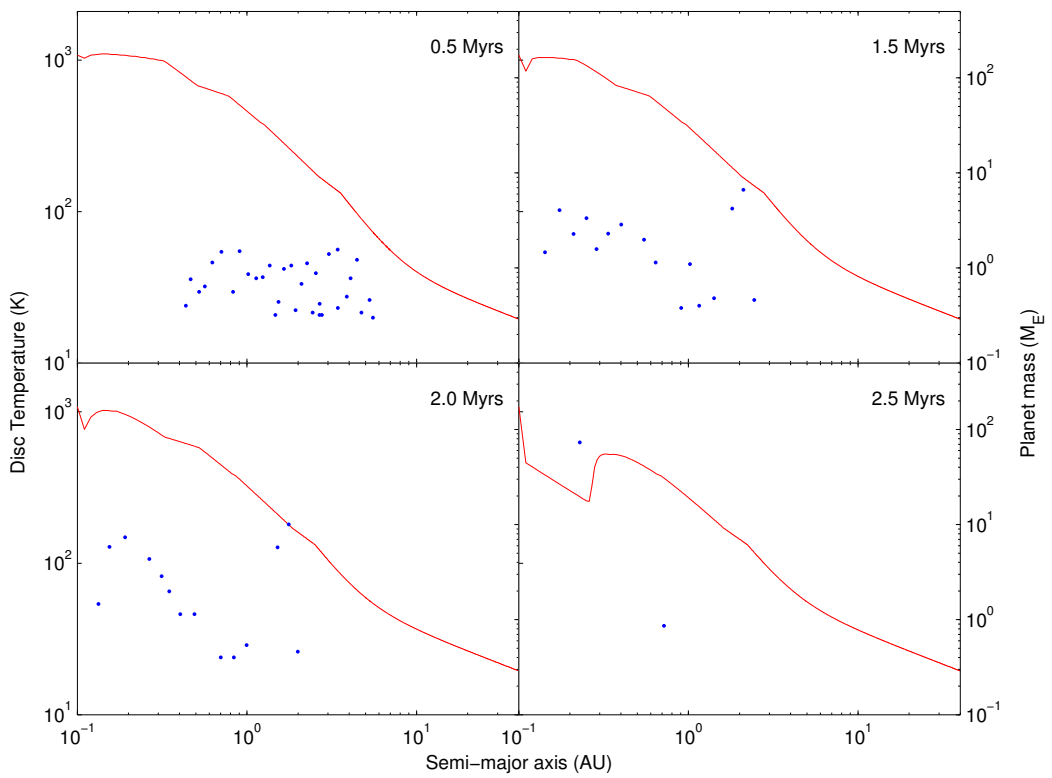
Figure 4.9: The locations and masses of the planets (blue dots) in run P06A plotted against the gas disc temperature (red line) at various times.
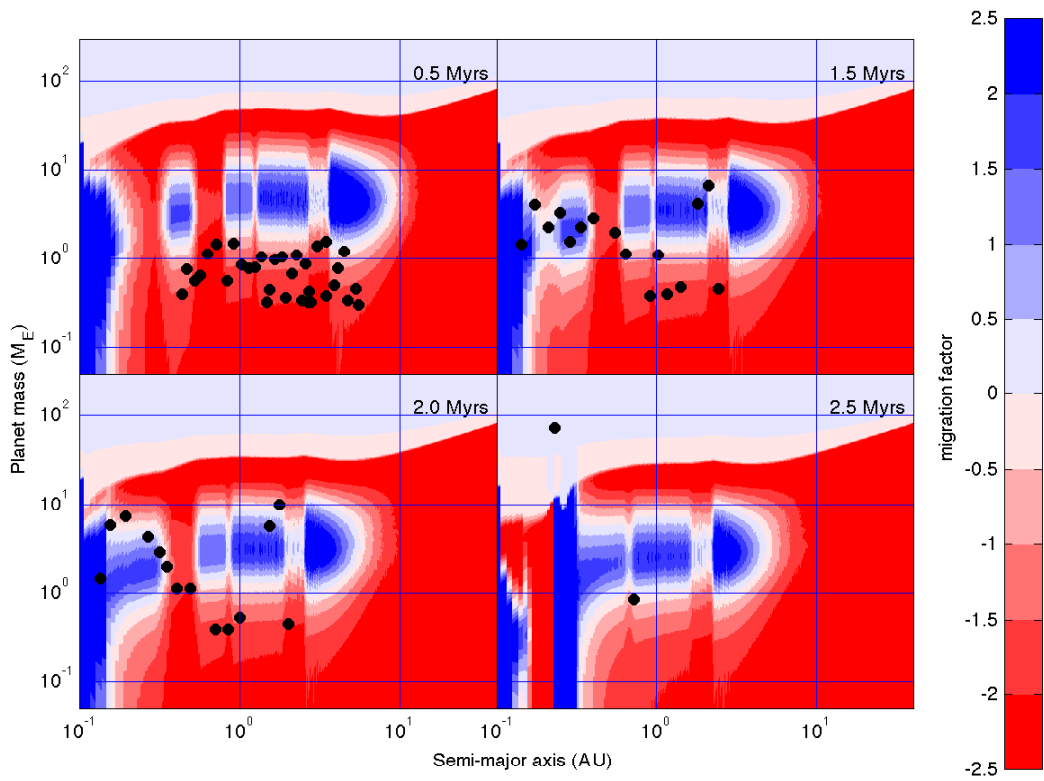
Figure 4.10: Contour plots showing regions of outward and inward migration for run P06A at various times. Regions of outward migration are shaded blue while regions of inward migration are shaded red. Planets are illustrated as black circles.
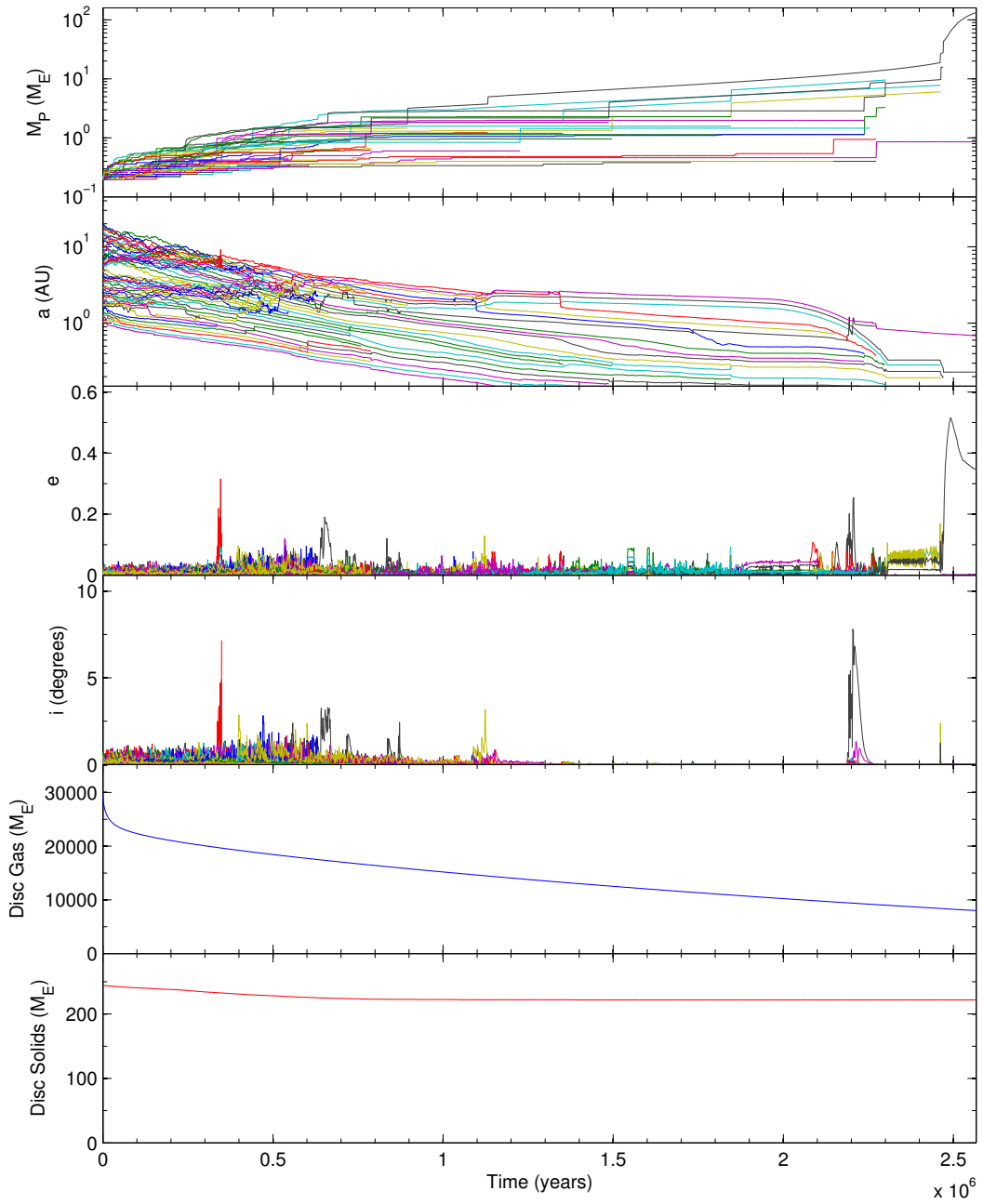
Figure 4.11: The evolution of masses, semimajor axes, eccentricities and inclinations for all protoplanets and the total gas disc mass and total planetesimal disc mass for simulation P06A.

the smaller planet being forced inwards despite being in a region of the disc that would suggest it should migrate outwards.

At 2.3 million years, they have migrated in to the inner region of the disc where two other planets that have now grown to 5.4 and 8.4 $M_\oplus$ have remained in outward migration zones at 0.20 and 0.24 AU respectively. These halt the inward migration of the outer two planets until shortly before 2.5 Myrs, the outer two planets merge, creating a new planet that is large enough to form a gap in the disc. This merger creates a domino effect such that the inner two planets merge themselves within 2000 years and in under 10000 years from the original merger, all of the four original planets have merged into one body which is rapidly accreting gas mass. The gap formed can be seen in the lower right plots in figures 4.8 and 4.10. In the contour plot, this is evident as the thick vertical blue band around the planet. The contour plots only display torque magnitude, which is why although this region is coded blue to signify a zone of outward migration, the disc is this region is depleted so no migration of any form would occur here.

By the end of the simulation run, at 2.57 Myr, this planet has grown to become a gas giant with a total mass of 139.4 $M_\oplus$, core mass of 28.1 $M_\oplus$ and at 0.23 AU. At the end point of this simulation, there is still a significant portion of disc mass remaining - equivalent to approximately 1.5 MMSN nebula which suggests that a significant amount of disc-related evolution is yet to come. However, the limits applied to minimum time step size in the simulation due to such a large planet with such a short period has truncated the possible simulation time. This planet is likely to migrate inwards further although in reality, an inner cavity may exist in such discs due to a strong magnetic field of the central star [Lin et al., 1996]. As in run P02A, there is a large amount of solid material in the form of planetesimals remaining between 2 and 20 AU which in reality would likely have reverted to runaway protoplanet growth. Since there is more than the equivalent of a 1/2 MMSN remaining, this run is considered an 'early' run.

4.4.2.3   Run P21B

Run P21B has an initial disc mass equivalent to 3 times the MMSN. The disc metallicity factor is 1, the f_{41} EUV photoevaporation is 100 and the planetesimal
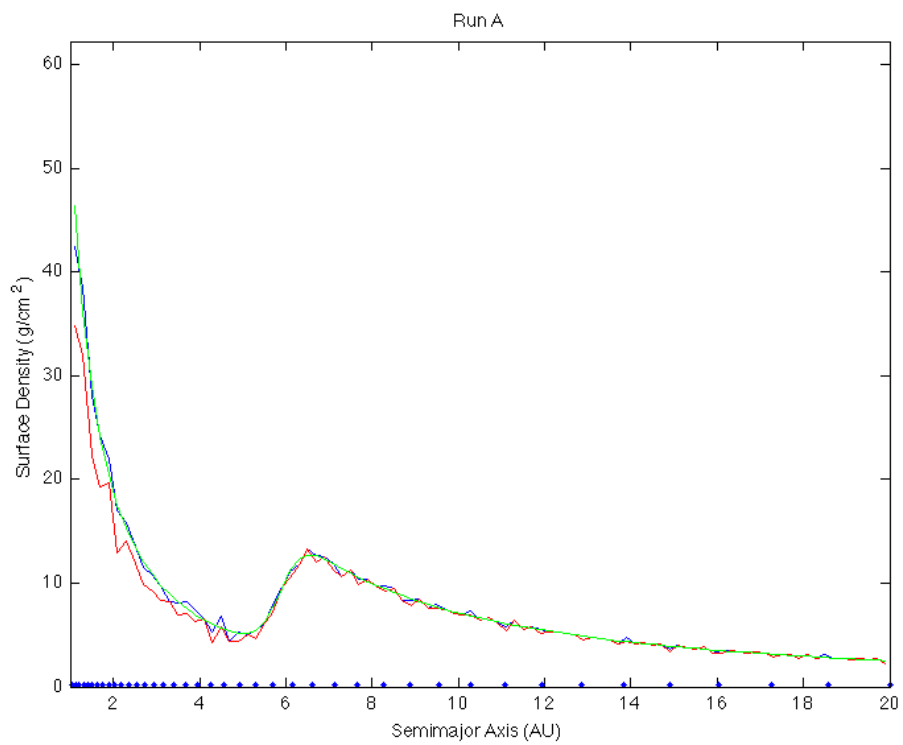
Figure 4.12: Initial solid body distribution for run P21B. The blue points mark the locations of the protoplanets, the red line denotes the planetesimal based surface density, the green line represents the target surface density for a disc of this size and the blue line represents the actual overall solids surface density.

size is 10 km. The initial solids distribution is shown in figure 4.12. Snapshots of the simulation conditions showing protoplanet locations, planetesimal surface density and gas disc surface density are shown in figure 4.13, disc temperature in figure 4.14 and torque magnitudes in figure 4.15. The time evolution of the planet masses, semi-major axes, eccentricities and inclinations for all the planets as well as the gas disc and planetesimal disc masses are shown in figure 4.16.

Growth is slightly slower than for run P06A due to the smaller disc mass but by 0.5 Myrs there are a few planets already in zero migration zones. By 1 Myrs there are even more, with a number of $\sim 2M_{\oplus}$ planets now present between 1.5 and 3 AU. Amongst the remaining smaller planets, the outermost planet - a 0.4
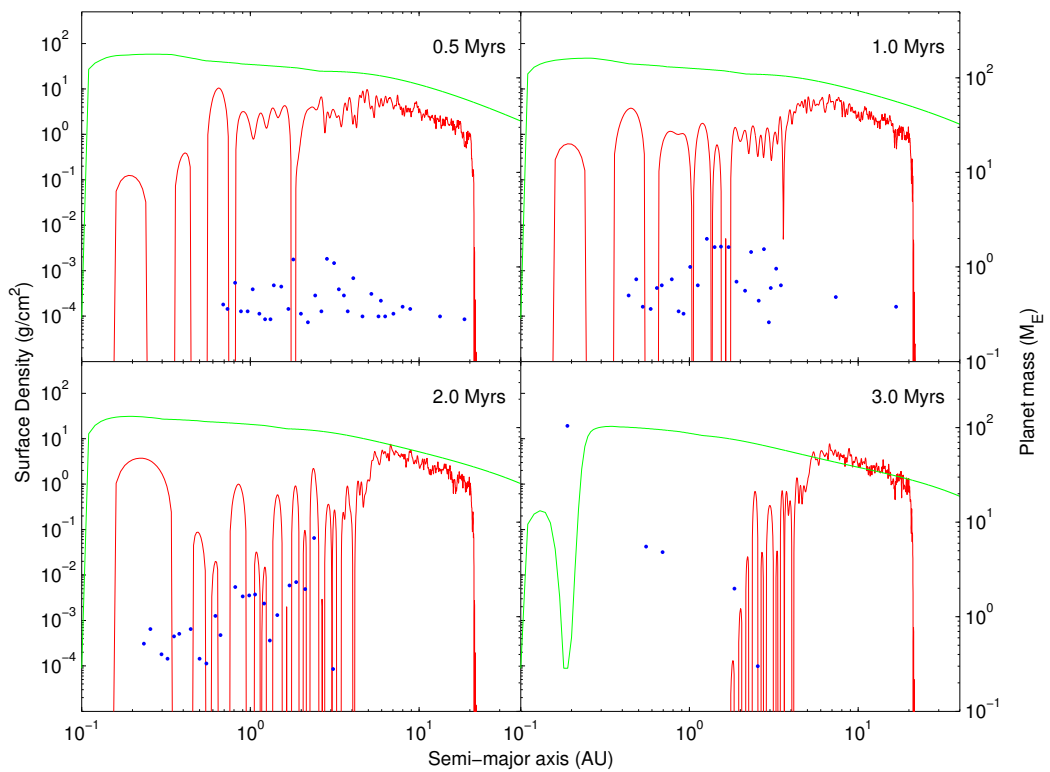
Figure 4.13: The locations and masses of the planets (blue dots) in run P21B plotted against the planetesimal (red line) and gas (green line) surface densities at various times. Plotted gas surface densities are reduced by a factor of 10 to allow concurrent plotting.

Figure 4.14: The locations and masses of the planets (blue dots) in run P21B plotted against the gas disc temperature (red line) at various times.

Figure 4.15: Contour plots showing regions of outward and inward migration for run P21B at various times. Regions of outward migration are shaded blue while regions of inward migration are shaded red. Planets are illustrated as black circles.
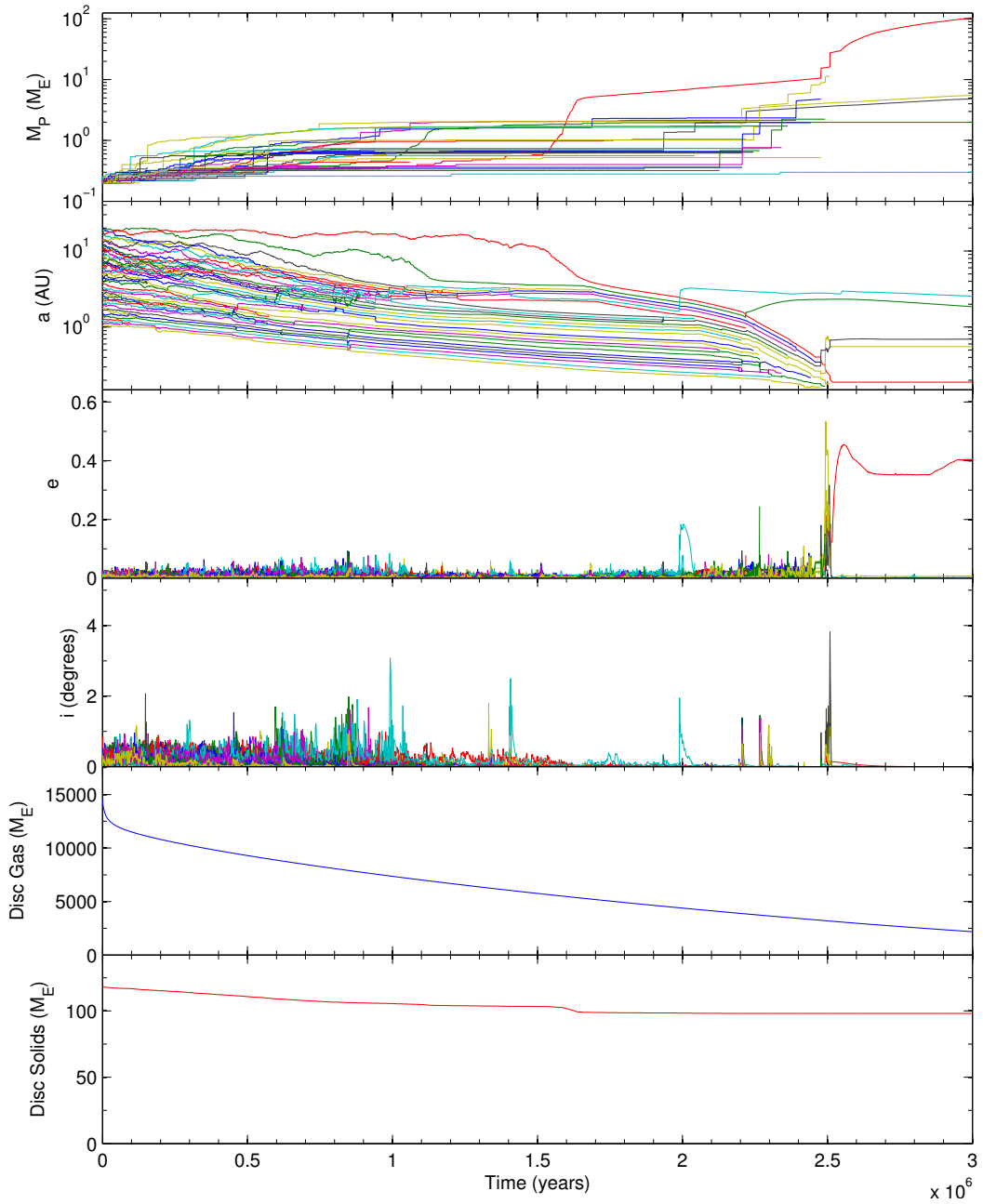
Figure 4.16: The evolution of masses, semimajor axes, eccentricities and inclinations for all protoplanets and the total gas disc mass and total planetesimal disc mass for simulation P21B.

$M_\oplus$ planet at 11 AU sits in a region that is rich in planetesimals but without any competing protoplanets - its only neighbour is 4.5 AU interior of it. Over the following 1 Myrs it gradually accretes planetesimals in isolation and slowly migrates inward due to its low mass and relative weakness of disc torques on such planets. After ~ 1.5 Myrs, the planet's mass increases to $\sim 1 M_\oplus$ and both its inward migration rate and mass accretion rate increase. By ~ 1.6 Myrs, it hits its region of zero migration at ~ 4 AU.

Over the next 0.5 Myrs, this planet continues to accrete material and slowly migrates in as its zero migration zone moves inward with disc dissipation. Meanwhile, it shepherds the now smaller planets interior of it so that they cannot migrate out to their typical zero migration lines. At 2.2 MYrs when it is 8.0 $M_\oplus$ and at 1.5 AU, it detaches from its area of zero migration due to its mass becoming too large. It then migrates inward, forcing most of the smaller bodies interior inwards as well.

Around 2.5 Myrs, when it is 10.6 $M_\oplus$ and at 0.41 AU, it merges with a 4 $M_\oplus$ body meaning that within a few thousand years, it is massive enough at 15.7 $M_\oplus$ to form a gap in the disc. Within 10,000 years, it has also accreted the remaining bodies interior to it and is now 27.6 $M_\oplus$ and at 0.21 AU. Over the following 0.5 Myrs, it continues eating gas mass and slowly moves in along with the disc as it gradually dissipates.

By the end of the simulation run at 3.0 Myrs, the planet has grown to a gas giant with a mass of 104.1 $M_\oplus$. Although there is still a portion of nebula gas still present (the equivalent to 0.44 MMSN), this planet is unlikely to migrate much further in before the gas disc dissipates entirely. As in the previous two runs, there is a large amount of solid material in the form of planetesimals remaining in the disc between 4 and 20 AU which in reality would likely have reverted to runaway protoplanet growth. Since there is less than the equivalent to a 1/2 MMSN nebula remaining, this run is considered an 'intermediate' run.

4.4.2.4   Run P30A

Run P30A has an initial disc mass equivalent to 3 times the MMSN. The disc metallicity factor is 1, the f_{41} EUV photoevaporation is 100 and the planetesimal
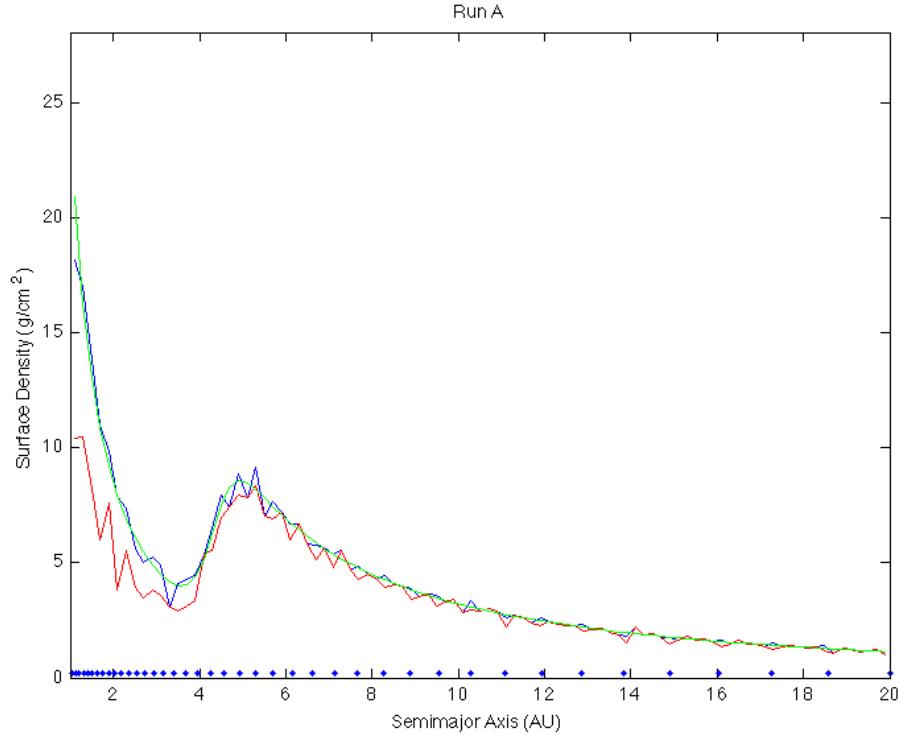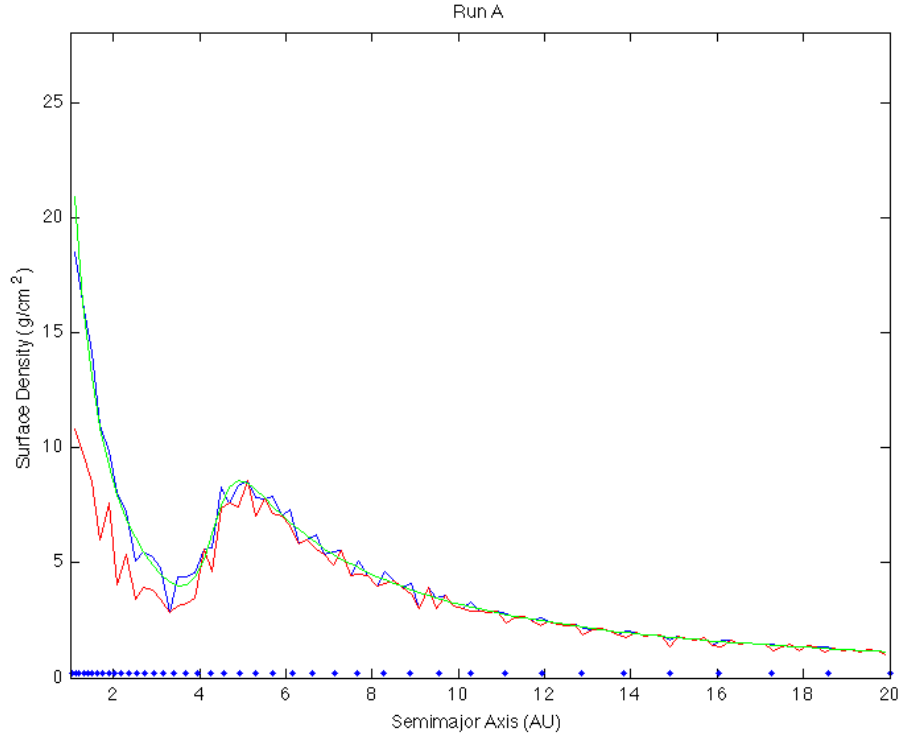
Figure 4.17: Initial solid body distribution for run P30A. The blue points mark the locations of the protoplanets, the red line denotes the planetesimal based surface density, the green line represents the target surface density for a disc of this size and the blue line represents the actual overall solids surface density.

size is 1 km. The initial solids distribution is shown in figure 4.17. Snapshots of the simulation conditions showing protoplanet locations, planetesimal surface density and gas disc surface density are shown in figure 4.18, disc temperature in figure 4.19 and torque magnitudes in figure 4.20. The time evolution of the planet masses, semi-major axes, eccentricities and inclinations for all the planets as well as the gas disc and planetesimal disc masses are shown in figure 4.21.

Despite only having a disc equivalent to 3 MMSN, growth is significantly faster than in the previous runs discussed here due to a smaller planetesimal size which increases accretion. Smaller planetesimals leads to a thinner planetesimal disc due to their exhibiting stronger damping of random velocities. This increases
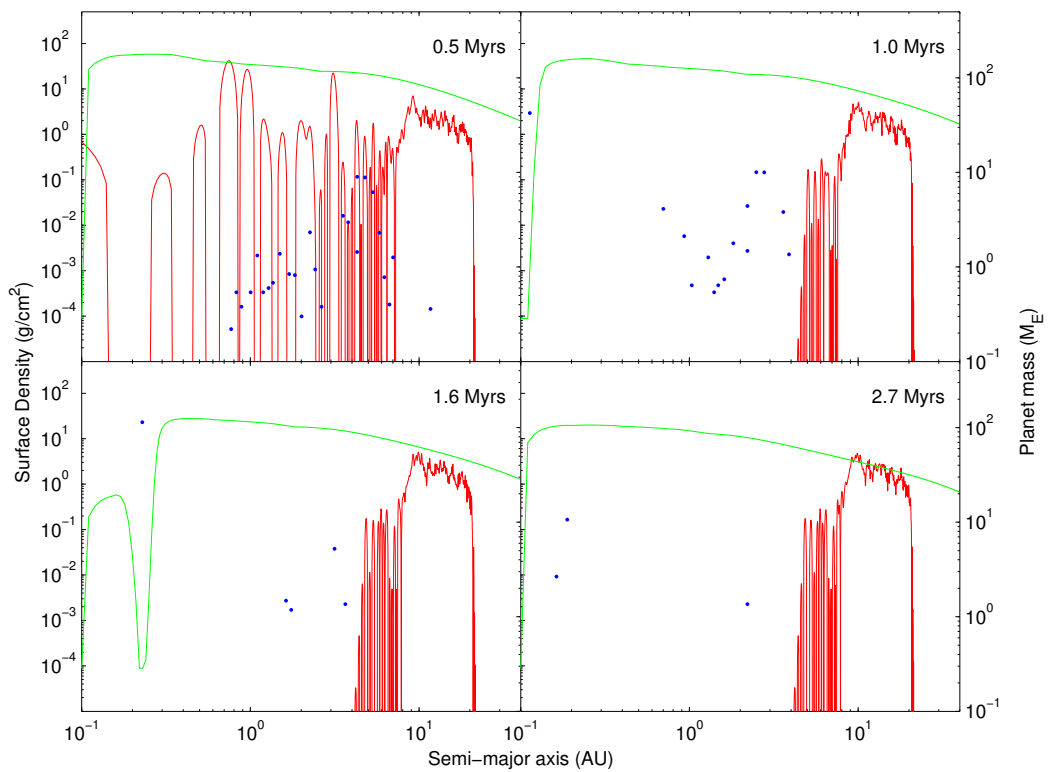
Figure 4.18: The locations and masses of the planets (blue dots) in run P30A plotted against the planetesimal (red line) and gas (green line) surface densities at various times. Plotted gas surface densities are reduced by a factor of 10 to allow concurrent plotting.
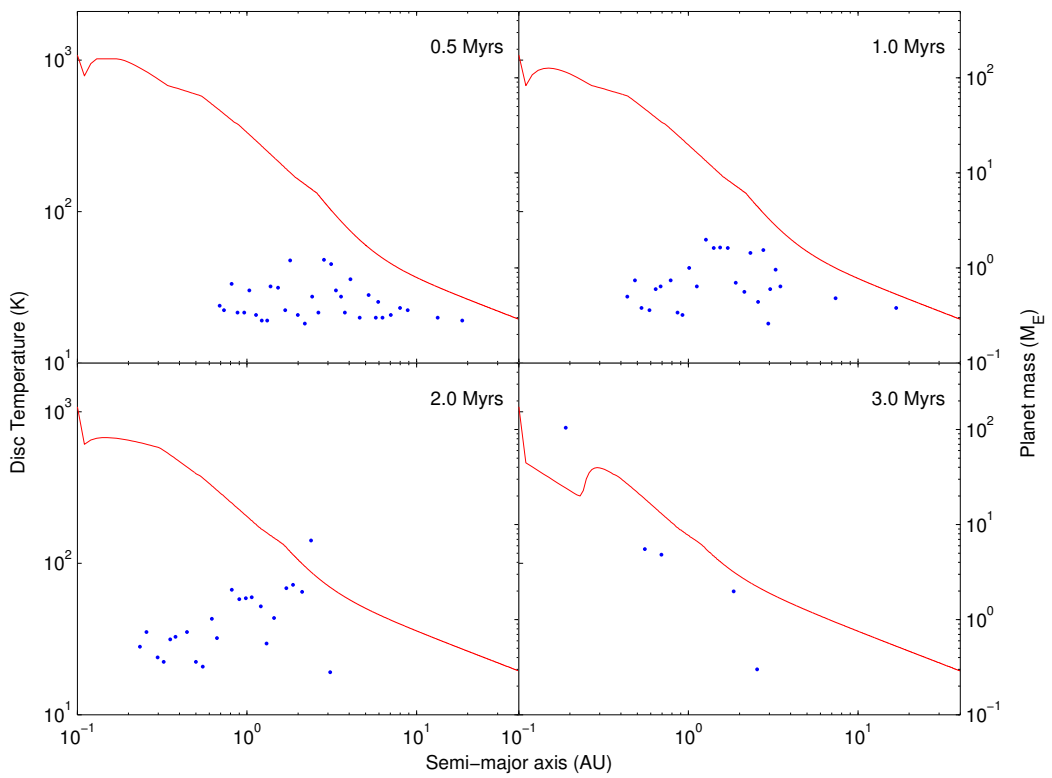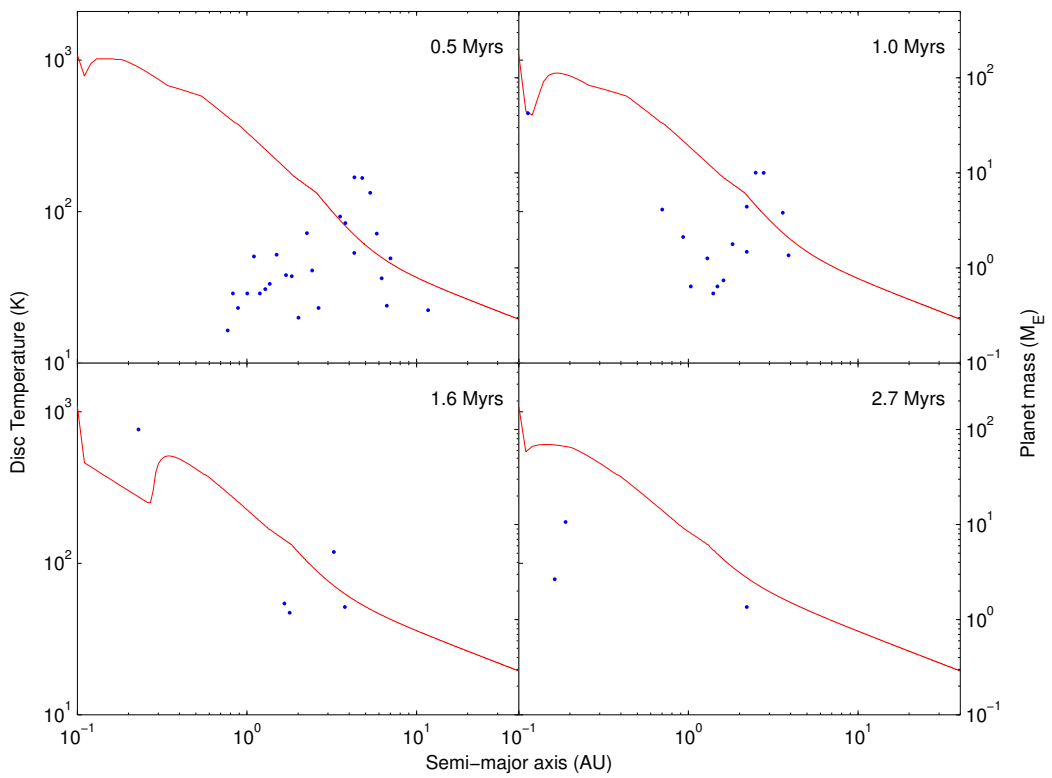
Figure 4.19: The locations and masses of the planets (blue dots) in run P30A plotted against the gas disc temperature (red line) at various times.
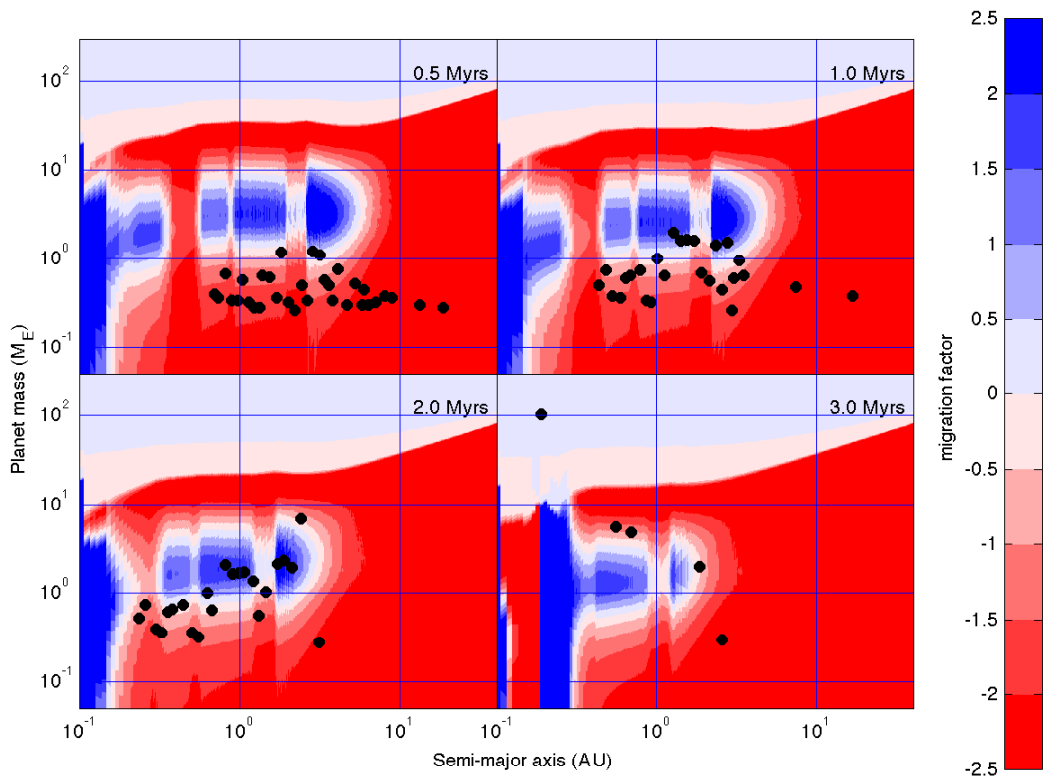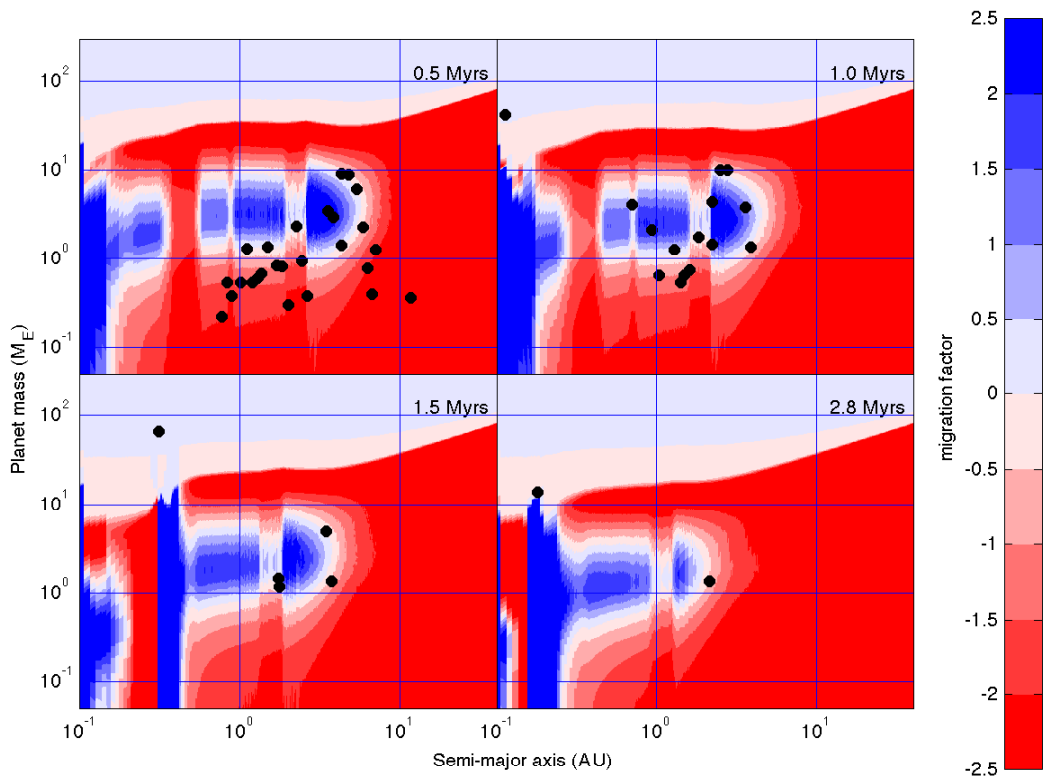
Figure 4.20: Contour plots showing regions of outward and inward migration for run P30A at various times. Regions of outward migration are shaded blue while regions of inward migration are shaded red. Planets are illustrated as black circles.
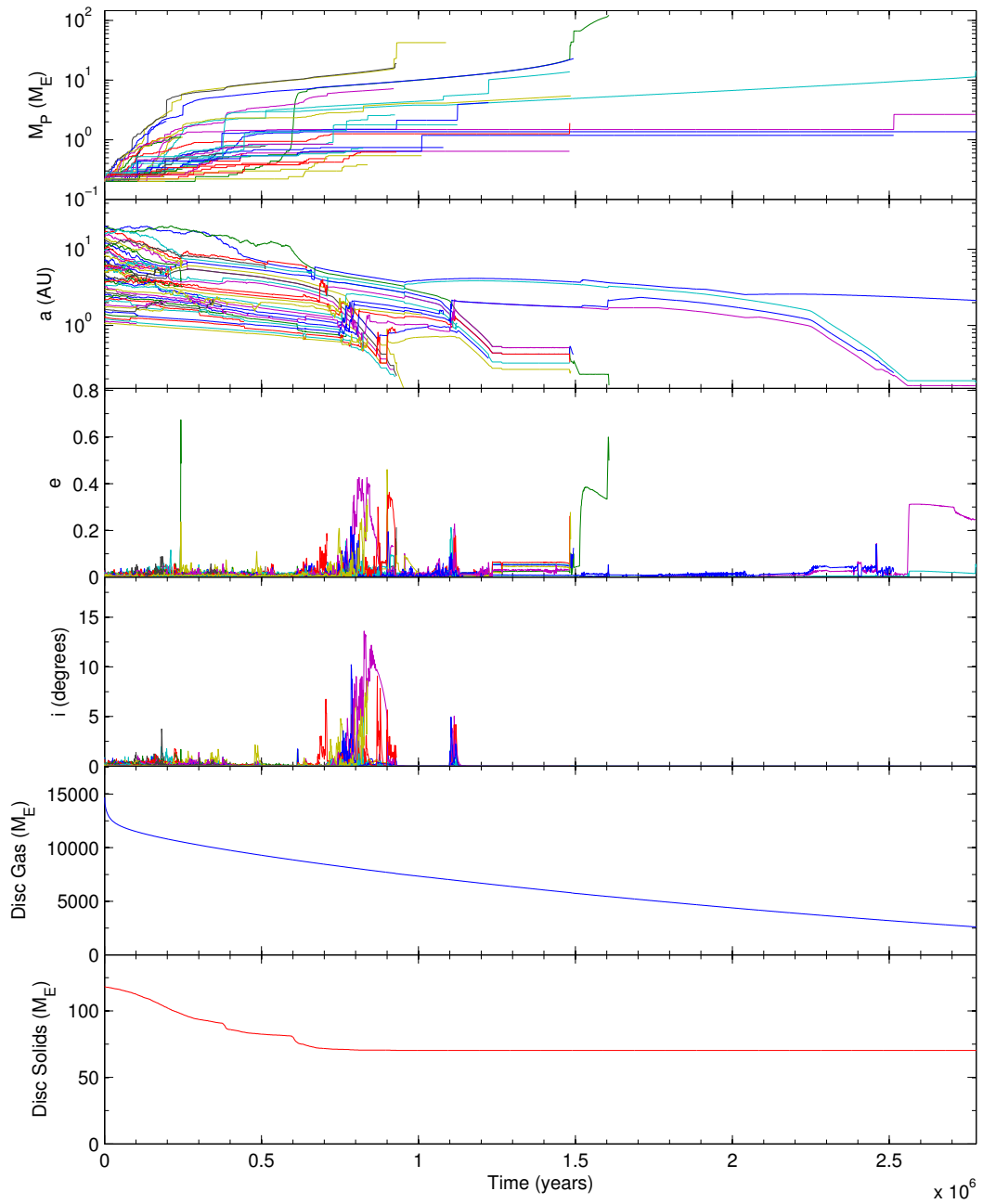
Figure 4.21: The evolution of masses, semimajor axes, eccentricities and inclinations for all protoplanets and the total gas disc mass and total planetesimal disc mass for simulation P30A.

accretion but has the downside that their orbital decay is faster.

By 0.5 Myrs, many planets have grown larger than 1 $M_\oplus$ with several almost 10 $M_\oplus$ already and sitting on zero migration lines around 5 AU. A number of the larger planets continue to grow and detach from their migration lines and migrate inwards before colliding just after 0.9 Myrs to form a 23.1 $M_\oplus$ planet at 0.33 AU. This planet forms a gap but then migrates inwards with the dissipation of the disc, being lost off the inner edge of the simulation range at 1.1 Myrs after reaching a mass of 42.5 $M_\oplus$.

The rest of the system continues evolving until just before 1.5 MYrs, two planets 22.3 and 22.0 $M_\oplus$ at 0.42 and 0.51 AU respectively cross the local criterion for gap formation and both create gaps in the disc. By 1.5 MYrs these two bodies have collided and also accreted a neighbouring super-earth such that the new planet has a mass of 66.5 $M_\oplus$ at 0.34 AU. It too migrates off the inner edge via type II migration shortly after 1.6 Myrs after reaching a mass of 120.8 $M_\oplus$.

The largest of the remaining planets (4.93 $M_\oplus$ at 3.5 AU at 1.5 Myrs) continues accreting until it grows large enough to detach from its migration line at 2.2 Myrs. It then migrates inwards, shepherding the inner two planets in along with it until they merge and migrate in to the edge of a very strong outward migration line at 2.6 Myrs. The two resonant planets now remain in situ while the larger planet continues to slowly accrete gas mass. At 2.8 Myrs, it accretes enough gas to fulfil the criterion for gap formation (signified by the upper edge to the red migration zones in the contour plots). Upon doing so, it accretes the inner planet as well.

The run ends shortly thereafter with the planet having reached a mass of 14.0 $M_\oplus$ with a gas mass of 5.7 $M_\oplus$ at 0.18 AU. Since it's composition is made up of 40% gas, this planet is classified as a neptune-like planet rather than a gas planet.

The run still has a a fair amount of disc mass left , equivalent to 0.53 MMSN. I classify this run as an early run although it is very close to being an intermediate run.

4.4.3 Summary of all runs

I ran 108 simulations covering two random-number seed realisations of 6 sets of discs with $f_{\mathrm{enh}} = 1, 2, 3, 4, 5, 6$ with an enhanced metallically factor of 1 and $f_{\mathrm{enh}} = 1, 2, 3, 4, 5, 6$ with an enhanced metallically factor of 2. Over those 6 sets I varied f_{41}, the EUV photoevaporation rate to three values, 1, 10 and 100 and I varied the planetesimal size to two values, 1 and 10 km. In total, 8 gas giant planets, 37 gas planets, 116 neptune-like planets, 154 super-earths and 519 terrestrial sized bodies were formed. The detailed break down of these is given in table 4.4.3 and their properties are summarised in figure 4.22. Plots showing the final semi-major axis and masses of planets formed in all of the runs as well as the planetesimal and gas surface densities are shown in figures 4.25 to 4.34.

Looking at table 4.4.3, it is clear that the majority of giant planets were formed in disc models that are considered to still be early in their development. The vast majority of these planets were formed in runs with a planetesimal size of 1 km which significantly decreased the formation time for large planetary cores at the beginning of a simulation's evolution. When in effect in discs with a large solids density such as the 5 and 6 MMSN and 3 MMSN with metalicity factor 2 models, this led to the very rapid growth of solid cores that detached from their zero migration lines and quickly migrated inwards. Inside 1 AU, the minimum planet mass for gap formation decreases with smaller semi-major axis as can be seen in the contour plots, figures 4.5, 4.10, 4.15 and 4.20. Thus a planet that has detached from its migration line due to being too massive can migrate inwards until it reaches a location where it meets the criterion for gap formation. While this improvs the likelihood that short period gas giants can form, such planets slow the finite-differencing method down by up to two orders of magnitude which has limited the degree to which I have been able to model such discs. All bar one of the giant planets were formed in simulations that are still considered to be in an 'early' state although some are close to being intermediate stage such as run P30A detailed above.

The heaviest planet formed in run P09A, a disc with a mass of 3 times MMSN and with a metallically enhancement factor of 2 so that it has the equivalent solids density as a 6 times MMSN disc. It reached 254.4 $M_{\oplus}$ with a solid core mass of

52.4 $M_\oplus$ and is located at 0.17 AU. Several runs generated more than one gap in the discs. Most of these were due to super-Earths or neptune-type planets such as in runs P18B (see figure 4.26) and P24B (see figure 4.28) but one run did form two gas giants very early on, both of which formed gaps (run P42B - see figure 4.32. Unfortunately, the time step requirements for this run have meant that it hasn't progressed beyond 0.2 Myrs.

All the giant planets formed in systems that had the solid material equivalent to 5 or 6 times MMSN. However, there are many of simulations containing what are currently neptune sized bodies that are still classed as 'early' and may therefore evolve into gas giant planets when run for longer.

A large number of neptune-like planets and super-earths were formed in a large proportion of the runs as well as a number of gas planets that are too low mass to qualify as gas giants. Furthermore, terrestrial sized planets were easily formed and survived throughout runs.

Early runs (60 runs)

type	no	$min(M_\mathrm{p})$	$max(M_\mathrm{p})$	M_p	$min(M_\mathrm{g})$	$max(M_\mathrm{g})$	M_g	$min(a_\mathrm{p})$	$max(a_\mathrm{p})$	$\bar{a}_\mathrm{p}$
gas giants	7	123.30	254.42	171.01	92.24	202.02	130.44	0.17	4.32	1.40
gas planets	26	8.95	34.93	15.39	5.01	18.94	8.93	0.15	3.33	0.51
neptune-like	91	3.53	77.45	14.23	0.21	17.75	3.81	0.15	8.07	1.93
super-earths	62	2.50	9.96	4.29	0.00	0.47	0.07	0.17	9.99	4.26
terrestrial	271	0.76	2.48	1.40	0.00	0.00	0.00	0.15	13.75	3.13

Intermediate runs (12 runs)

type	no	$min(M_\mathrm{p})$	$max(M_\mathrm{p})$	M_p	$min(M_\mathrm{g})$	$max(M_\mathrm{g})$	M_g	$min(a_\mathrm{p})$	$max(a_\mathrm{p})$	$\bar{a}_\mathrm{p}$
gas giants	1	104.23	104.23	104.23	82.85	82.85	82.85	0.19	0.19	0.19
gas planets	6	8.79	30.23	13.07	5.32	16.62	7.57	0.18	0.50	0.34
neptune-like	11	4.18	26.58	9.42	0.27	9.79	3.10	0.22	4.43	0.75
super-earths	10	2.54	4.62	3.22	0.00	0.04	0.00	0.21	6.55	1.69
terrestrial	44	0.78	2.38	1.40	0.00	0.00	0.00	0.31	14.95	2.40

Late runs (36 runs)

type	no	$min(M_\mathrm{p})$	$max(M_\mathrm{p})$	M_p	$min(M_\mathrm{g})$	$max(M_\mathrm{g})$	M_g	$min(a_\mathrm{p})$	$max(a_\mathrm{p})$	$\bar{a}_\mathrm{p}$
gas giants	0	0.00	0.00	0.00	0.00	0.00	0.00	0.00	0.00	0.00
gas planets	5	26.12	32.84	30.03	16.71	25.52	22.64	0.29	3.61	1.29
neptune-like	6	4.52	16.38	9.76	1.02	5.66	2.98	0.33	8.46	1.86
super-earths	54	2.50	10.00	4.16	0.00	0.08	0.00	0.30	14.63	2.54
terrestrial	191	0.76	2.48	1.30	0.00	0.00	0.00	0.29	20.47	3.79

4.5 Comparison with Observations and Previous Chapter

As in the previous chapter, this work is not intended to be a serious attempt at planetary population synthesis unlike the work presented by Ida et al. [2008] and
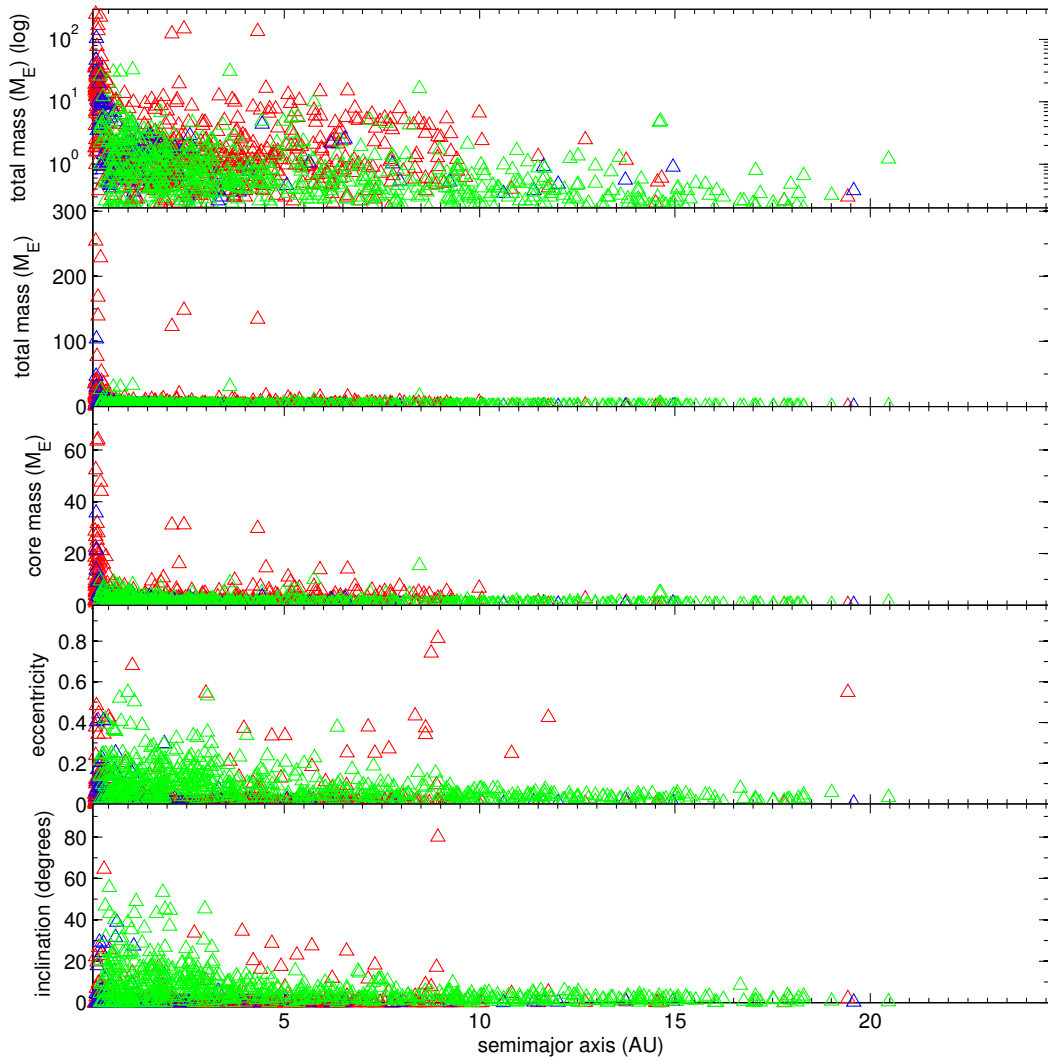
Figure 4.22: Summary of total masses, core masses, eccentricity and inclination against semi-major axis for all planets formed. The colour of the markers is dependent on the simulation state - red for early runs, blue for intermediate runs and green for late runs.

Figure 4.23: Summary of the semi-major axis and masses of all planets plotted alongside the gas and planetesimal surface densities for runs P01A - P09A. Runs P01A - P06A correspond to disc masses equivalent to 1 - 6 MMSN respectively. Runs P07A - P09A correspond to disc masses of 1 - 3 MMSN respectively with a metalicity enhancement factor of 2. The planetesimal size for all the runs is 10 km and the $f_4 1$ EUV photoevaporation rate is set to 1 for all runs. Planetesimal surface densities are plotted in grey. The colour of the gas surface density line and the planet plots is dependent on the simulation state - red plots for early runs, blue plots for intermediate runs and green plots for late runs.

Figure 4.24: Summary of the semi-major axis and masses of all planets plotted alongside the gas and planetesimal surface densities for runs P01B - P09B. Runs P01B - P06B correspond to disc masses equivalent to 1 - 6 MMSN respectively. Runs P07B - P09B correspond to disc masses of 1 - 3 MMSN respectively with a metalicity enhancement factor of 2. The planetesimal size for all the runs is 10 km and the f_41 EUV photoevaporation rate is set to 1 for all runs. Planetesimal surface densities are plotted in grey. The colour of the gas surface density line and the planet plots is dependent on the simulation state - red plots for early runs, blue plots for intermediate runs and green plots for late runs.

Figure 4.25: Summary of the semi-major axis and masses of all planets plotted alongside the gas and planetesimal surface densities for runs P10A - P18A. Runs P10A - P15A correspond to disc masses equivalent to 1 - 6 MMSN respectively. Runs P16A - P18A correspond to disc masses of 1 - 3 MMSN respectively with a metalicity enhancement factor of 2. The planetesimal size for all the runs is 10 km and the $f_4 1$ EUV photoevaporation rate is set to 10 for all runs. Planetesimal surface densities are plotted in grey. The colour of the gas surface density line and the planet plots is dependent on the simulation state - red plots for early runs, blue plots for intermediate runs and green plots for late runs.
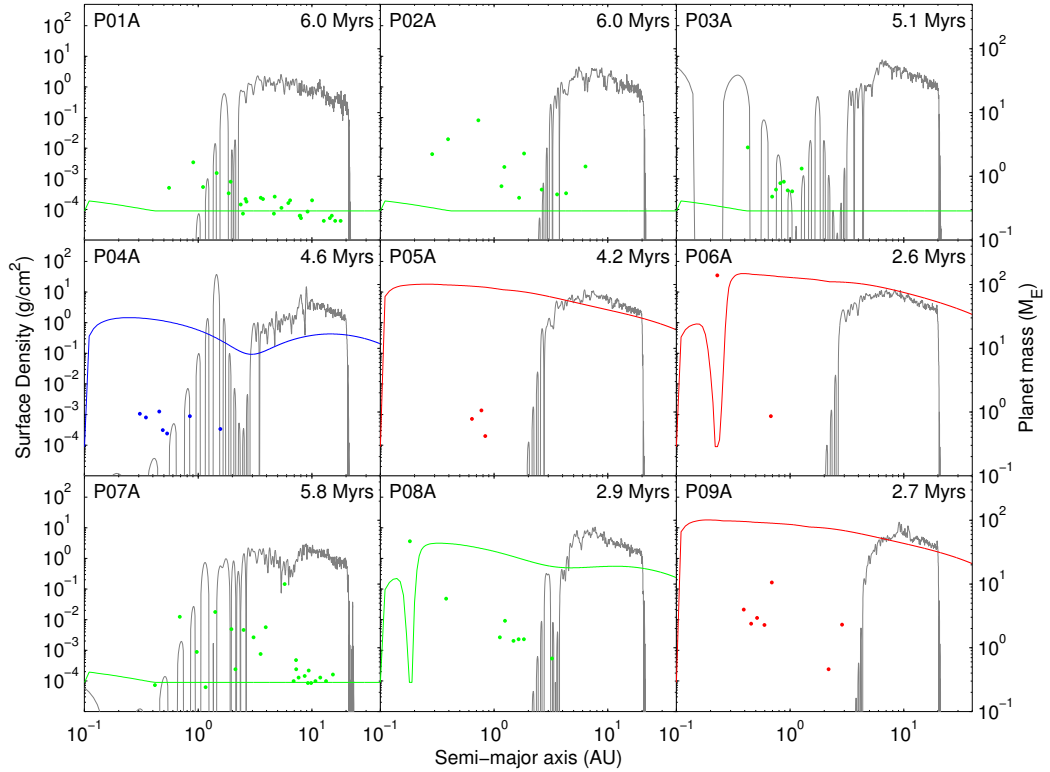
Figure 4.26: Summary of the semi-major axis and masses of all planets plotted alongside the gas and planetesimal surface densities for runs P10B - P18B. Runs P10B - P15B correspond to disc masses equivalent to 1 - 6 MMSN respectively. Runs P16B - P18B correspond to disc masses of 1 - 3 MMSN respectively with a metalicity enhancement factor of 2. The planetesimal size for all the runs is 10 km and the $f_4 1$ EUV photoevaporation rate is set to 10 for all runs. Planetesimal surface densities are plotted in grey. The colour of the gas surface density line and the planet plots is dependent on the simulation state - red plots for early runs, blue plots for intermediate runs and green plots for late runs.

Figure 4.27: Summary of the semi-major axis and masses of all planets plotted alongside the gas and planetesimal surface densities for runs P19A - P27A. Runs P19A - P24A correspond to disc masses equivalent to 1 - 6 MMSN respectively. Runs P25A - P27A correspond to disc masses of 1 - 3 MMSN respectively with a metalicity enhancement factor of 2. The planetesimal size for all the runs is 10 km and the $f_4$1 EUV photoevaporation rate is set to 100 for all runs. Planetesimal surface densities are plotted in grey. The colour of the gas surface density line and the planet plots is dependent on the simulation state - red plots for early runs, blue plots for intermediate runs and green plots for late runs.
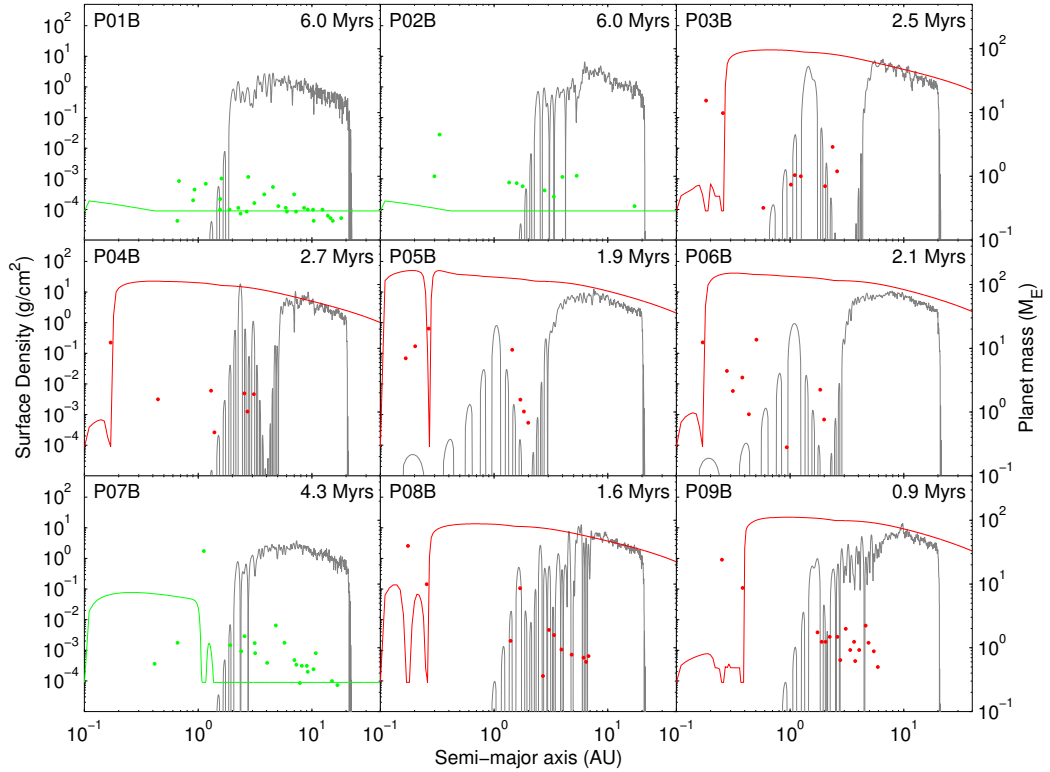
Figure 4.28: Summary of the semi-major axis and masses of all planets plotted alongside the gas and planetesimal surface densities for runs P19B - P27B. Runs P19B - P24B correspond to disc masses equivalent to 1 - 6 MMSN respectively. Runs P25B - P27B correspond to disc masses of 1 - 3 MMSN respectively with a metalicity enhancement factor of 2. The planetesimal size for all the runs is 10 km and the $f_4 1$ EUV photoevaporation rate is set to 100 for all runs. Planetesimal surface densities are plotted in grey. The colour of the gas surface density line and the planet plots is dependent on the simulation state - red plots for early runs, blue plots for intermediate runs and green plots for late runs.
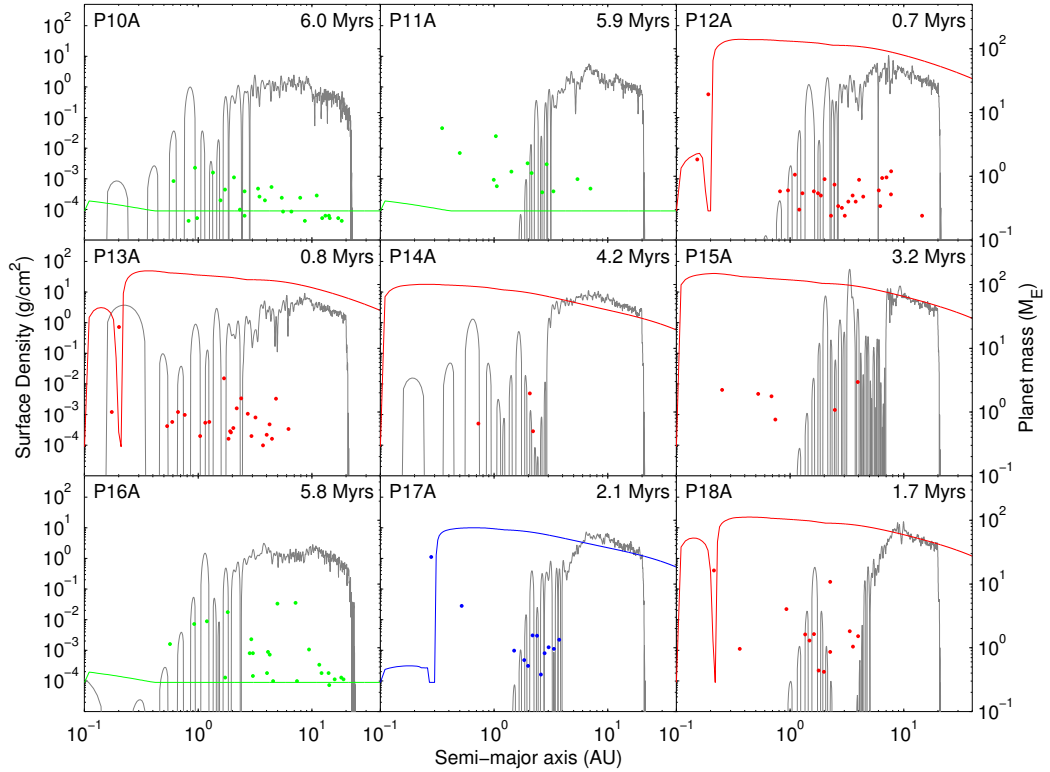
Figure 4.29: Summary of the semi-major axis and masses of all planets plotted alongside the gas and planetesimal surface densities for runs P28A - P36A. Runs P28A - P33A correspond to disc masses equivalent to 1 - 6 MMSN respectively. Runs P34A - P36A correspond to disc masses of 1 - 3 MMSN respectively with a metalicity enhancement factor of 2. The planetesimal size for all the runs is 1 km and the $f_4 1$ EUV photoevaporation rate is set to 1 for all runs. Planetesimal surface densities are plotted in grey. The colour of the gas surface density line and the planet plots is dependent on the simulation state - red plots for early runs, blue plots for intermediate runs and green plots for late runs.
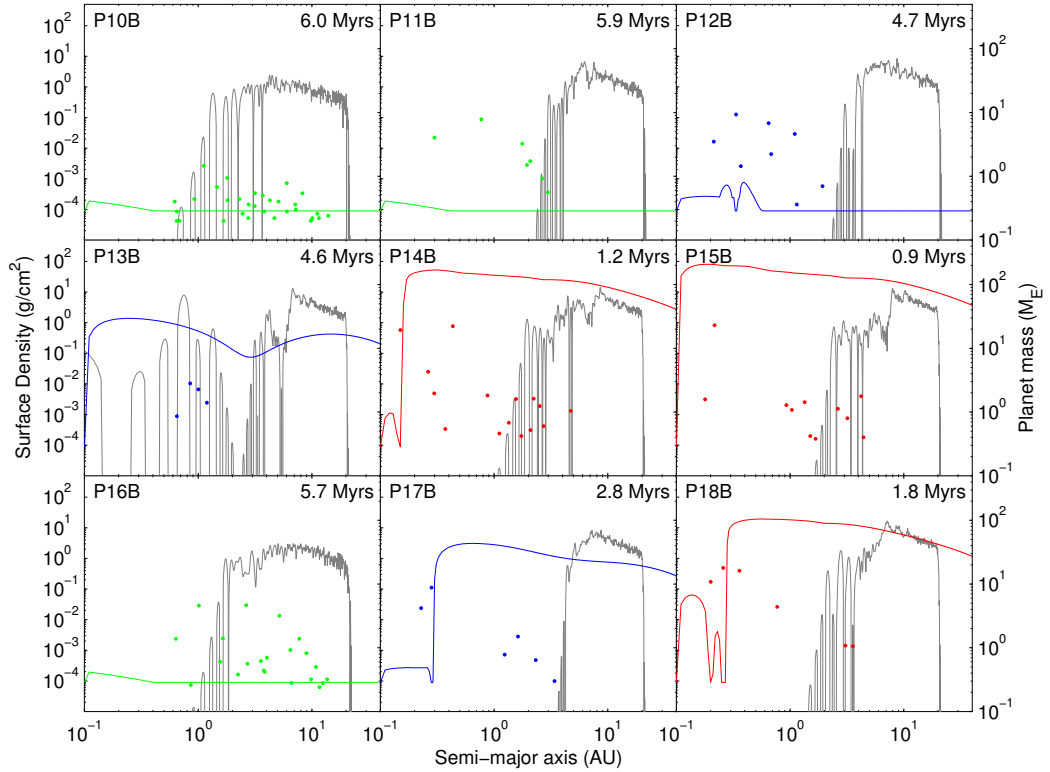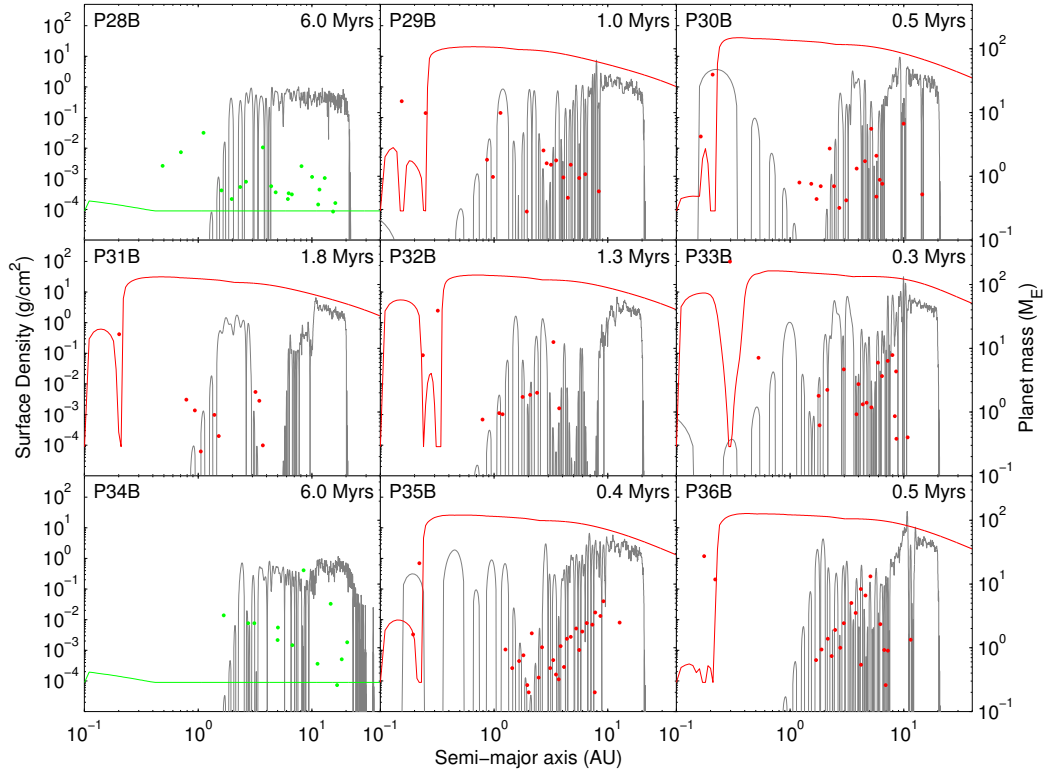
Figure 4.30: Summary of the semi-major axis and masses of all planets plotted alongside the gas and planetesimal surface densities for runs P28B - P36B. Runs P28B - P33B correspond to disc masses equivalent to 1 - 6 MMSN respectively. Runs P34B - P36B correspond to disc masses of 1 - 3 MMSN respectively with a metalicity enhancement factor of 2. The planetesimal size for all the runs is 1 km and the $f_4$1 EUV photoevaporation rate is set to 1 for all runs. Planetesimal surface densities are plotted in grey. The colour of the gas surface density line and the planet plots is dependent on the simulation state - red plots for early runs, blue plots for intermediate runs and green plots for late runs.
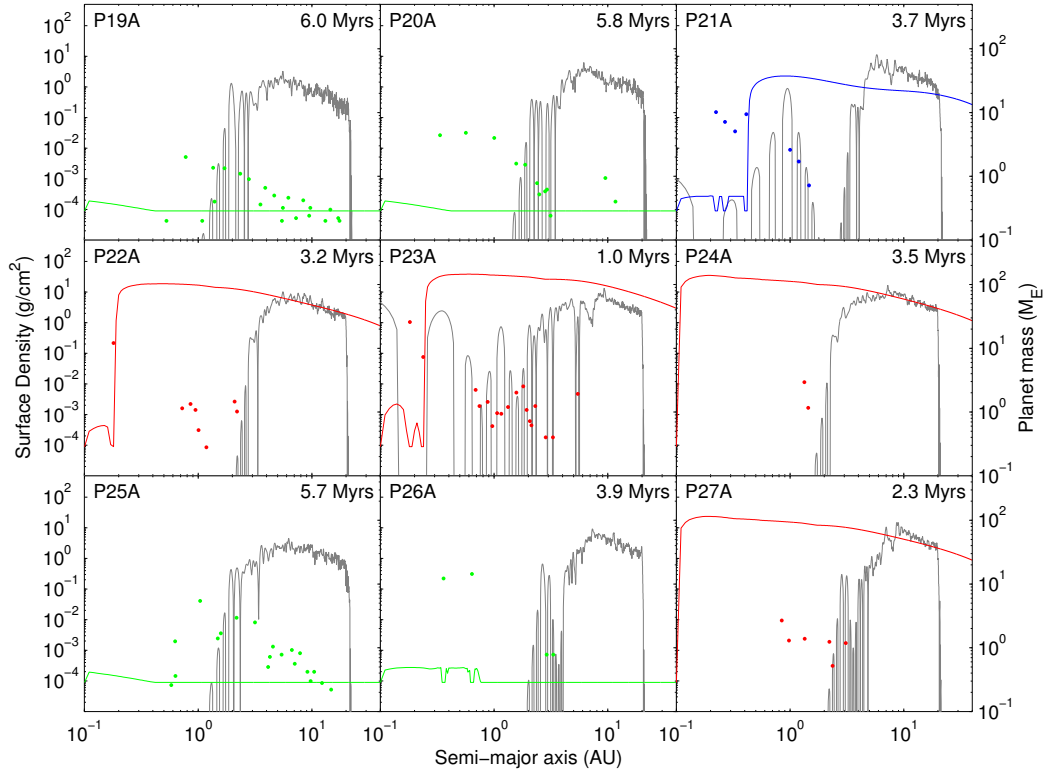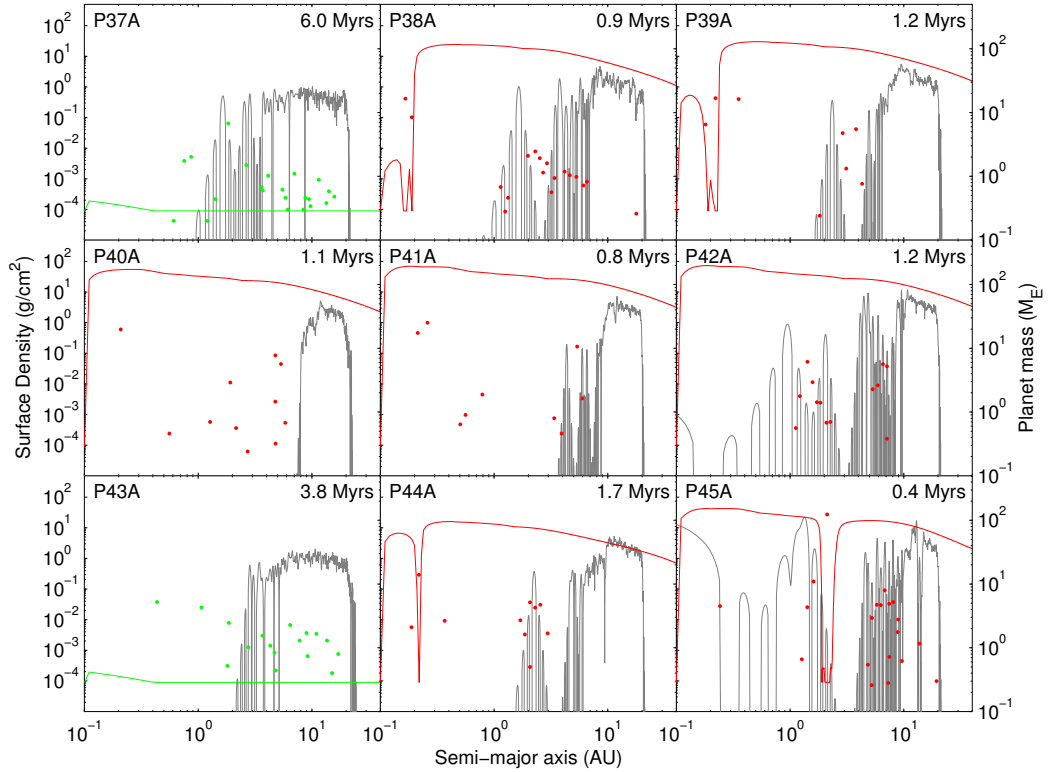
Figure 4.31: Summary of the semi-major axis and masses of all planets plotted alongside the gas and planetesimal surface densities for runs P37A - P45A. Runs P37A - P42A correspond to disc masses equivalent to 1 - 6 MMSN respectively. Runs P43A - P45A correspond to disc masses of 1 - 3 MMSN respectively with a metalicity enhancement factor of 2. The planetesimal size for all the runs is 1 km and the $f_4$1 EUV photoevaporation rate is set to 10 for all runs. Planetesimal surface densities are plotted in grey. The colour of the gas surface density line and the planet plots is dependent on the simulation state - red plots for early runs, blue plots for intermediate runs and green plots for late runs.
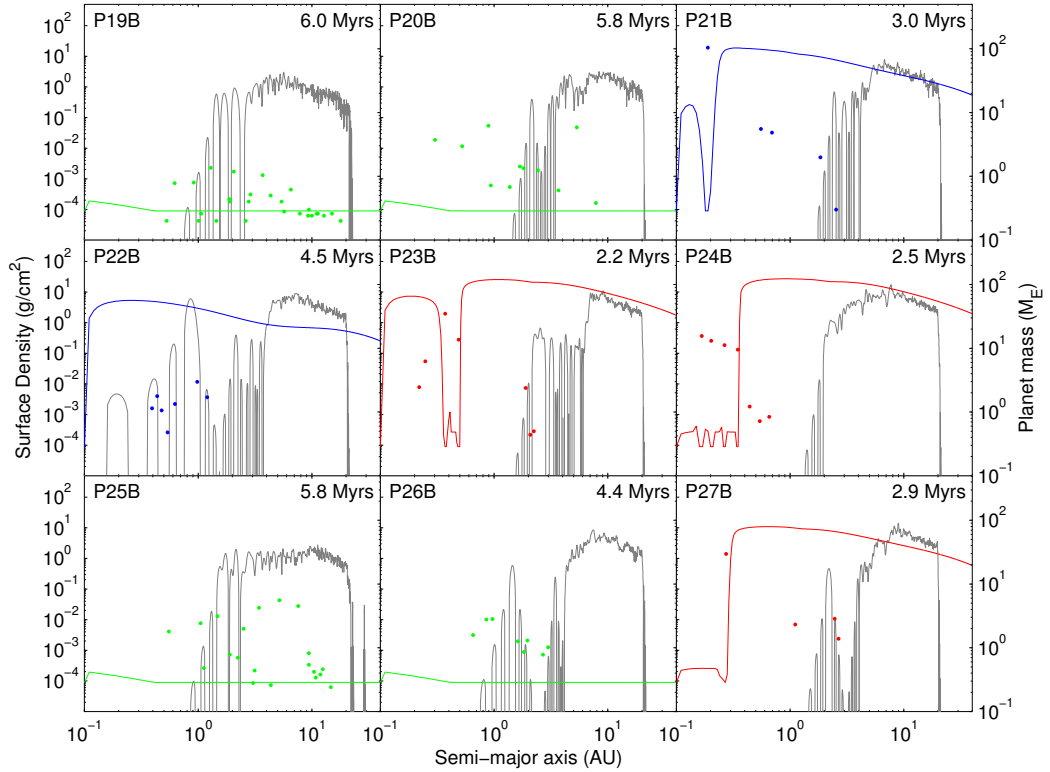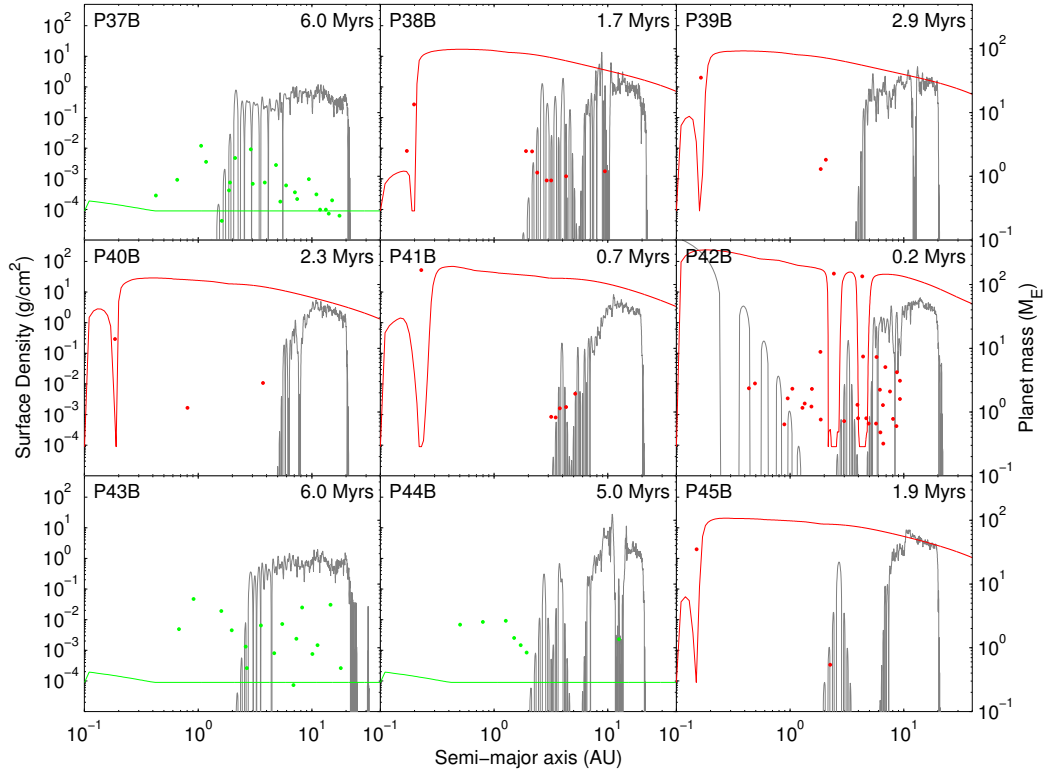
Figure 4.32: Summary of the semi-major axis and masses of all planets plotted alongside the gas and planetesimal surface densities for runs P37B - P45B. Runs P37B - P42B correspond to disc masses equivalent to 1 - 6 MMSN respectively. Runs P43B - P45B correspond to disc masses of 1 - 3 MMSN respectively with a metalicity enhancement factor of 2. The planetesimal size for all the runs is 1 km and the $f_4 1$ EUV photoevaporation rate is set to 10 for all runs. Planetesimal surface densities are plotted in grey. The colour of the gas surface density line and the planet plots is dependent on the simulation state - red plots for early runs, blue plots for intermediate runs and green plots for late runs.
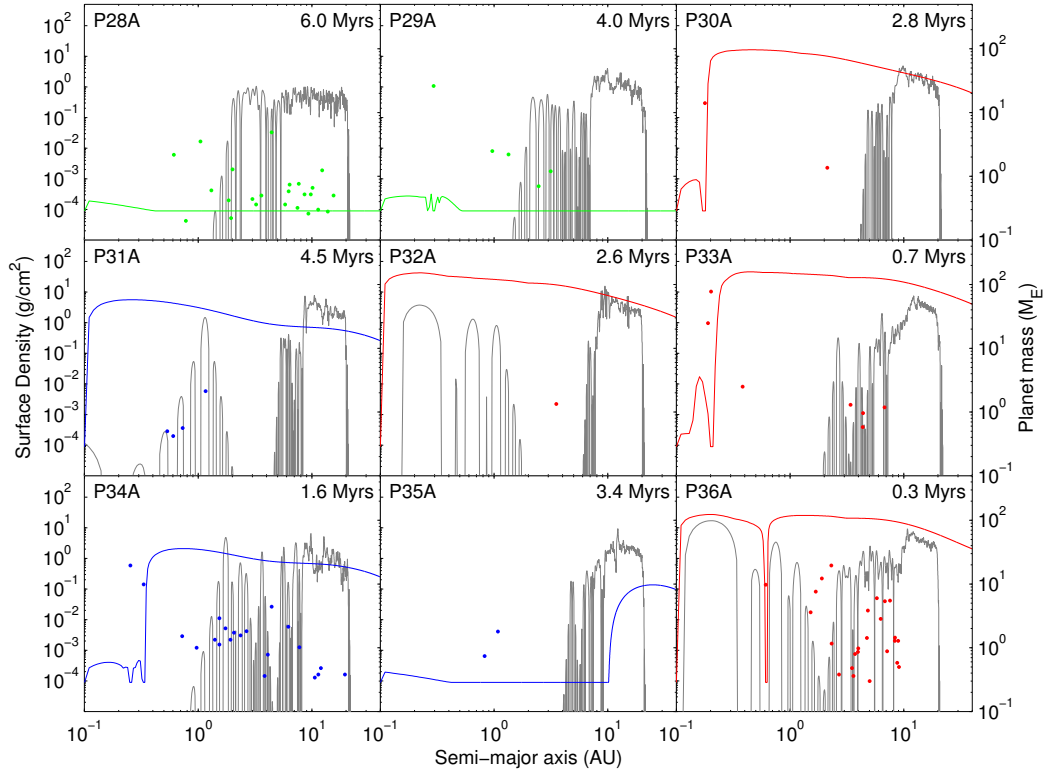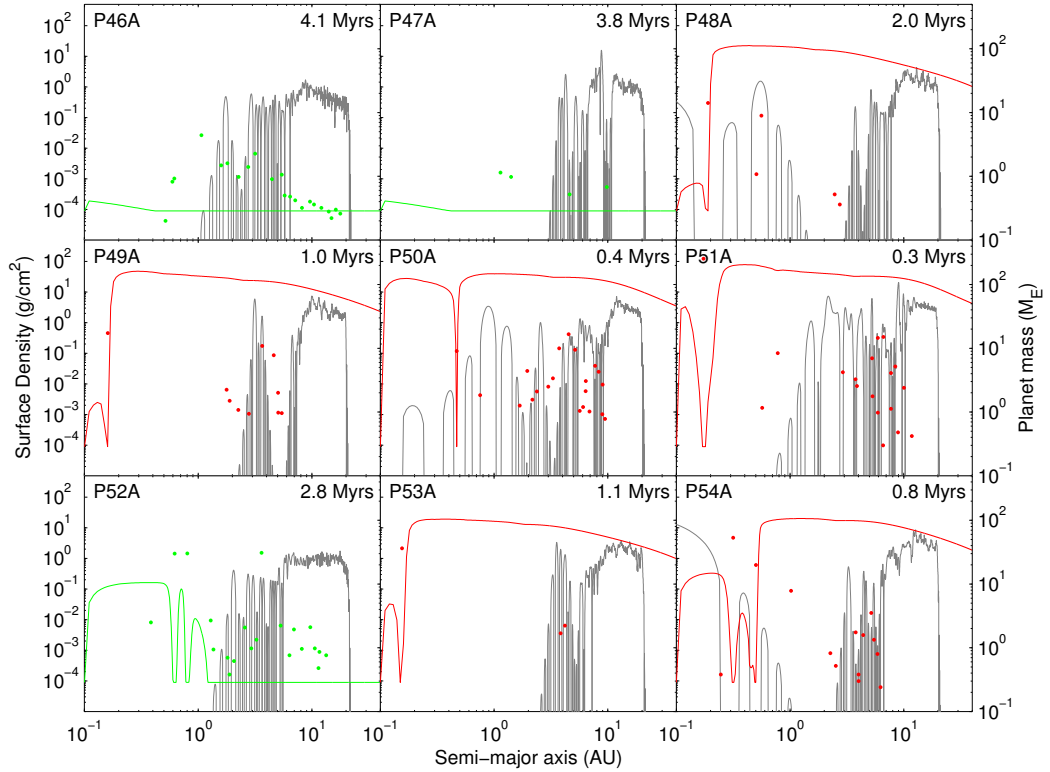
Figure 4.33: Summary of the semi-major axis and masses of all planets plotted alongside the gas and planetesimal surface densities for runs P46A - P54A. Runs P46A - P51A correspond to disc masses equivalent to 1 - 6 MMSN respectively. Runs P52A - P54A correspond to disc masses of 1 - 3 MMSN respectively with a metalicity enhancement factor of 2. The planetesimal size for all the runs is 1 km and the $f_4 1$ EUV photoevaporation rate is set to 100 for all runs. Planetesimal surface densities are plotted in grey. The colour of the gas surface density line and the planet plots is dependent on the simulation state - red plots for early runs, blue plots for intermediate runs and green plots for late runs.
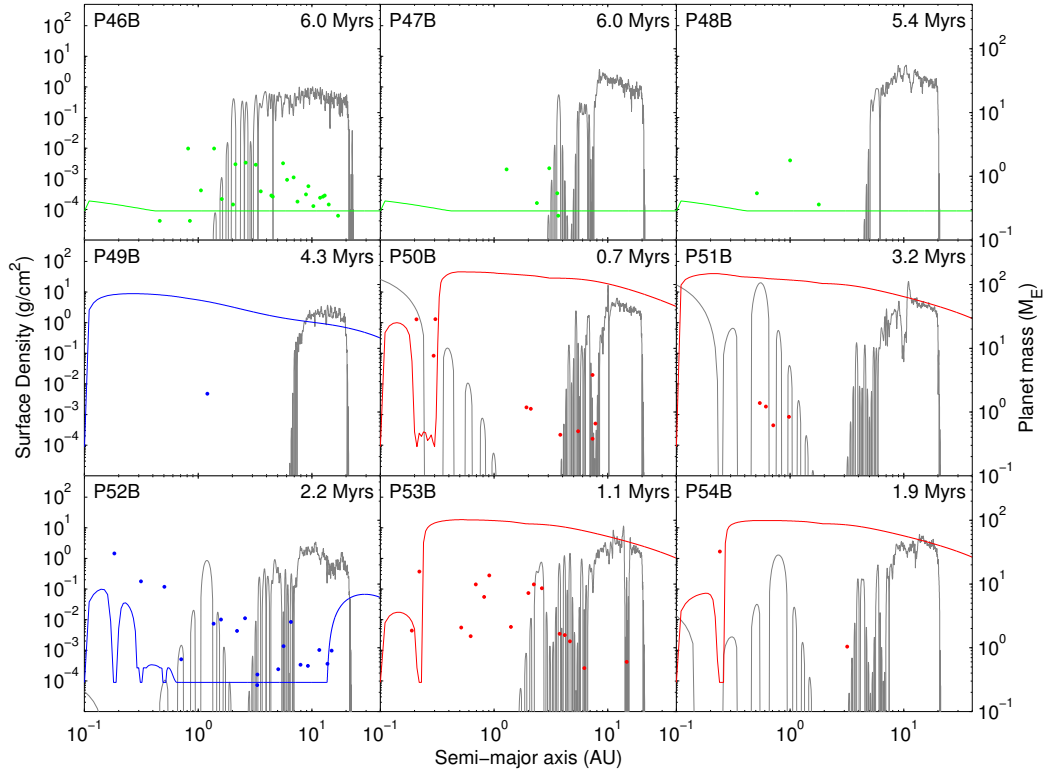
Figure 4.34: Summary of the semi-major axis and masses of all planets plotted alongside the gas and planetesimal surface densities for runs P46B - P54B. Runs P46B - P51B correspond to disc masses equivalent to 1 - 6 MMSN respectively. Runs P52B - P54B correspond to disc masses of 1 - 3 MMSN respectively with a metalicity enhancement factor of 2. The planetesimal size for all the runs is 1 km and the $f_4$1 EUV photoevaporation rate is set to 100 for all runs. Planetesimal surface densities are plotted in grey. The colour of the gas surface density line and the planet plots is dependent on the simulation state - red plots for early runs, blue plots for intermediate runs and green plots for late runs.

Mordasini et al. [2009b]. This work builds on my previous work in exploring the effect on planetary growth, migration and interaction in the presence of strong corotation torques. As before, it is still interesting to compare how well these simple models compare to real-world observations and what effect the increase in model complexity has had on the resulting planetary populations compared to the model of the previous chapter.

Figure 4.35 shows a mass-period diagram with the results of this chapter overlaid on both all current observed exoplanets as well as all planets formed in the results from the previous chapter. All of the giant planets formed in this chapter lie well within the region of observed exoplanets although the majority of those formed are still in discs with a considerable portion of disc mass sill left and therefore would likely migrate into the central star without the presence of an inner cavity in the disc formed by strong magnetic field lines from the central star. The greatest success of this model over the previous version is the large number of super-earths and neptune type planets, of which the previous model was unable to form any.

The biggest effect introducing an evolving 1 dimensional disc model has been to qualitatively improve the contour plots. Compare the contour plot for run M05A in the previous chapter (figure 3.6) to that for run P06A in section 4.4.2.2 (figure 4.10). The steep straight angles bounding regions of outward migration in M05A are far more conducive towards convergent migration than the relatively flat zones in run P06A. Although convergent migration does still occur, planets of similar masses must have both a closer ratio of masses and must start closer together. To illustrate this, consider two planets of identical mass, 5 $M_\oplus$, with one at 1 AU and one at 50 AU dropped into a disc such as in run M05A at time 1 Myr (top right frame of figure 3.6). The innermost planet starts off lying inside a zone of outward migration and moves out to the zero migration line at ~ 25 AU. The outer planet starts off in a zone of inward migration and moves inwards to the zero migration line. Even though both planets start a great distance apart, their final destination is at the same location and so they collide. Now consider the same planets embedded in a disc such as that for run P06A at 1.5 Myrs (top right frame of figure 4.10). The inner most planet again starts in a zone of outward migration and migrates out until it hits a boundary with an inward

migration zone at ~ 3 AU. The outer most planet again starts in a zone of inward migration and migrates in until it hits a boundary with an outward migration zone at ~ 7 AU.

The complexity in the contour plots and thus the underlying torques, is due primarily to the new temperature model that is built into the disc model. As described in section 4.1.1.2, the temperature in the disc is calculated by solving the energy flux equation of the disc. This has a large dependency on disc opacities which as shown in section 4.1.1.3, specifically equation 4.33 and figure 4.1, follow quite different forms depending on the local disc conditions. This can be seen in the temperature summary plots for the individual runs such as figure 4.9.

In the previous work, growing planets would often grow until they reached their zero migration line and would then sweep outwards through the disc as they accreted mass and so would be pushed to a greater semi-major axis. This would push them through large swathes of the planetary disc, accreting bodies along the way before finally growing so large as to either undergo rapid gas accretion or detach from the migration line and undergo type I migration into the star. This meant that it was comparatively difficult for super-earth and neptune like planets to form, masses of that size would migrate outwards and rapidly accrete more mass. The more complex torques in effect in the models of this chapter don't allow such behaviour to occur. Planetary solid accretion is largely based upon the local solids density rather than any migratory behaviour. Planets tend to in effect be locked in place once they hit an area of zero migration and then accrete gradually as planetesimals are accreted or other protoplanets move into their vicinity. Growth is remarkably similar in such situations to models without the presence of a gas disc.

Out of the few gas giants that have formed in this study, none are as large as Jupiter. This is due to a limit of a 1D disc model. Once a planet has formed a gap in a disc, it would typically accrete mass through streamline from the neighbouring material. As this is a 1D model, these streamlines are not modelled - their radial velocities are averaged out over grid cells that cover the whole ring of the gap which means their effect is lost. Mass simply cannot flow into a gap in a 1D disc. I have attempted to find a balance between the gap width formed in the disc by the model and the region over which a planet can viscously accrete

material by using a value of Q_{gap} of 3 in section 4.2.2.1.

In comparison to observational results, the planets formed in this paper align well although the majority of planets (i.e. the lower mass bodies) lie in regions of the mass-period space that is currently relatively unpopulated by exo-planets although this is likely due to the current limitations of observational technologies. As documented in table 4.4.3, I have a number of gas giants with relatively short periods. These are comparable to detected hot Jupiters such as 51-Peg b (0.47 Jupiter masses with period 4.23 days) [Mayor and Queloz, 1995] and HD 209458b [Deming et al., 2005] - the latter being a giant planet detected via transit and one of the only exoplanets to have had a temperature measured. Some of my gas giants have very large solid cores which is counter to what is theorised for Jupiter and Saturn, however, observational evidence supports the existence of such planets - planet HD 149026b is a Saturn sized planet with a suggested solid core of up to 67 $M_\oplus$ [Sato et al., 2005]. A number of hot neptunes similar to those formed in these simulations have been detected also, such as Gliese 436b [Butler et al., 2004] and Kepler-4 b [Borucki et al., 2011]. Rocky super earths have been detected similar to those produced in my runs such as CoRot-7b [Léger et al., 2009] and Kepler-10b [Batalha et al., 2011] and even some terrestrial sized planets have been detected analogous to some produced here such as alpha Cen B b [Dumusque et al., 2012]. Lastly, even low mass, low density planets have been detected such as Kepler-11f [Lissauer et al., 2011] that lend credence to the non giant gas planets formed in my simulations here.

4.6   Discussion and Conclusions

The models presented in this chapter include a large range of physical processes relevant to planetary formation (migration; planetary growth through mutual protoplanet collisions, planetesimal accretion, gas accretion, planet-planet interactions, nebula disc evolution). However, a number of simplifications and assumptions have been included that affect the realism of the simulations and results presented in this chapter. These include:

1. *Simulation domain.* A common problem when modelling planetary forma-
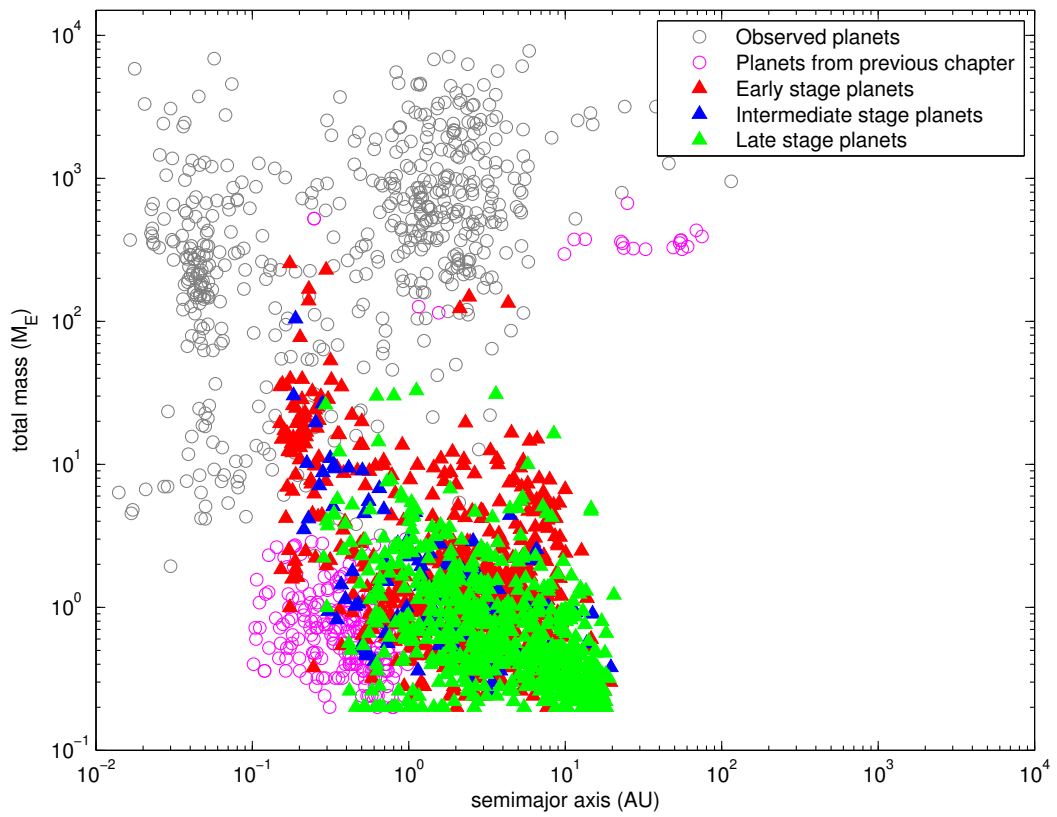
Figure 4.35: Mass vs semimajor axis plot comparing the results from this model to both observed extrasolar planets and the results from the previous chapter.

tion with the use of n-body models is the range over orbital radius which can be simulated. I have included a wider initial body distribution than in the work of the previous chapter (1-20 AU compared to 2-15 AU in chapter 3). With the use of a finite differencing based gas disc model, it has also been necessary to impose limits to which the gas disc is modelled. I took the limits to be 0.01-40 AU as examination of initial contour plots for this model suggested that migration of planets out beyond that range, as occurred in my previous model, was unlikely to occur. However, models covering an initial solids distribution and modelled gas disc from as far in to 0.1 AU out to 50 AU would be preferable as migration driven growth suggests protoplanets can begin from anywhere in the disc before its evolution is complete. Such a simulation is currently beyond modelling techniques due to the large required numbers of protoplanets. Although some methods suggest the use of multiple time steps in a parallel symplectic integrator [McNeil and Nelson, 2009, 2010] can achieve greater particle densities, global models of planetary formation with large numbers of particles and grid cells are more likely to require efficient use of GPGPU technologies. However, such models would limit the number of concurrent simulations that could be run compared to the single threaded nature of the Mercury code so investigations covering large parameter sets such as in this chapter are unlikely. A further modification to the code would be to use grid separations that are not linearly spaced. This would allow for a finer resolution at short periods without requiring the same to be imposed on larger periods where such small cells are not needed. This would still require small timesteps due to these being set by the smallest grid cells but it could allow simulations of the same overall resolution as those used here but with fewer cells thus speeding up computational time.

2. *Fresh protoplanet generation.* A common feature in the late stages of these models is a large domain of 'unused' planetesimal matter in the outer regions of simulations as seen in the final snapshots of runs in figures 4.25 through 4.34. These regions have been formed due to the protoplanets that were initially present migrating inwards. This was not an issue in the runs from

the previous chapter due to the strong outward migration along migration lines that led to very rapid accretion and allowed protoplanets to migrate through the outer regions of the planetary disc, accreting large amounts of solid matter before detaching from their migration lines, migrating inward via type I migration and colliding with the central star. In reality, these large protoplanet-free solids-rich zones would revert to a period of runaway growth leading to a new generation of protoplanets. A possible solution to this problem would be to introduce a mechanism by which a few planetesimals in these regions would be promoted to protoplanetary status and given a mass boost (removing a corresponding number of planetesimals from their vicinity in the process) which would allow the region to begin a new phase of oligarchic growth.

3. *Planetary atmosphere model and enhanced capture radii.* The model of an enhanced accretion rate due to the greater capture radius of a planet that has a planetary atmosphere works well when planetesimal accretion is dominating mass growth, however, it does not deal with planet-planet collisions in a realistic manner. A planetary atmosphere can be blasted off a planet during an impact with a second planet with a similar mass to its atmosphere. A further modification would be to include the accretion of in-falling gas in the luminosity calculation used for the enhanced capture radius. There is likely a range of planets that have yet to satisfy the gap formation criterion in the disc but are accreting a significant amount of gas that would increase the luminosity of a planet. This would have the effect of reducing the effective capture radius which would slow down planetesimal growth during the early gas accretion phase of a planet. This would likely reduce the overall core size of neptune-type planets, gas planets and gas giants.

4. *Timestep issue.* The small timesteps required due to the radial velocities near the edges of deep gaps around large planets is particularly problematic when such planets are at short periods - an unfortunate scenario in models where large planets can migrate inwards with the eventuality that they get accreted by the central star. To address this, an implicit solver technique

could be used so that larger timesteps could be used while maintaining stability.

5. *2D disc model.* Although this one dimensional disc model has added a significant level of complexity compared to the model of chapter 3, it does have a significant limitation in its inability to handle viscous accretion of gas onto planets within gaps via streamlines. A 1D model has only a single radial velocity value which is an average of all possible radial velocity values over the ring in the disc corresponding to the cell. This means that the counterflow velocity of streamlines that allow a planet to accrete gas matter from outside the gap are lost, limiting the realism of giant planet viscous gap accretion due to approximations such as those detailed in section 4.2.2.1.

I have presented the results of simulations that include recent torque formulae for type I migration (including Lindblad and corotation torques) with gas disc evolution of surface density and temperature including photo-evaporation, planet gas envelope accretion, enhanced capture radii of planets due to gas atmospheres and planet-planet gravitational dynamics. I have surveyed a range of disc models covering a wide variety of parameters. The main results that I have obtained may be summarised as follows:

- Inward migration can be halted by corotation torques when the thermal and viscous diffusion times are configured in such a way that corotation torques can oppose and equal the inward Lindblad torques. This can slow down migrating planets long enough for them to accrete further solid and gas mass until they become massive enough to form a gap in the disc or until the disc mass has dissipated so that it can no longer influence the planet.

- A large range of planetary types can be formed over a large range of semi-major axes. Terrestrial planets, super-earths, neptune-like planets, gas planets and gas giants were all formed throughout the protoplanetary disc. Interestingly, some super-earths larger than neptune-like planets are formed and similarly, some neptune-like planets larger than gas planets are formed. This wide variety of planetary types is a significant improvement

over the model of the previous chapter which lacked any planets between small super-earths and giant planets.

- Out of 108 simulations that covered a wide variety of parameters, 8 gas giants were formed. While this is fewer than in the previous chapter, their masses are far more varied due to the removal of artificial limits on mass growth made possible by the active modelling of the gas in the disc. Further giant planets are likely to form if the runs that are still in an early stage were to be allowed to continue to completion.

Chapter 5

Conclusion

The models presented in this thesis are an investigation into the effects of non isothermal corotation torques on planet formation and include a wide variety of physical processes relevant to planet formation. The features modelled are as follows:

1. *Oligarchic growth of a solids based disc.* The oligarchic growth phase of planet formation is modelled by using a hybrid-symplectic n-body model with protoplanets modelled individually and planetesimals modelled as effective superplanetesimals with a hit-and-stick collision model that allows the growth of protoplanets from protoplanet-protoplanet mergers and planetesimal accretion. The initial distribution of planets and protoplanets is matched to that of the gas disc and includes a snow line density enhancement due to condensation of materials in the disc in cooler regions.

2. *Gas disc.* The gas disc portion of a protoplanetary disc is modelled using a finite differencing model that allows for the evolution of gas surface density and temperature of a planetary disc in one dimension.

3. *Aerodynamic drag.* Planetesimals experience a frictional drag force due to the difference in a planetesimal's velocity and that of the gas disc. This acts to damp eccentricities, inclinations and semi-major axes of planetesimals over time.

4. *Atmospheric drag.* Planetesimal accretion onto protoplanets is enhanced due to the effective capture radius enhancement of planets as a result of

nascent planetary atmospheres. A thicker atmosphere applies more drag to a planetesimal passing through it, thus increasing the effective cross sectional accretion area, so a greater proportion of close encounters between protoplanets and planetesimals leads to accretion.

5. *Planetary migration.* Interactions between the gas in the disc and the protoplanets gives rise to torques that are applied to both the disc and the planets in the form of Lindblad and corotation torques. These give rise to migration of planets in the form of inward type I migration but with the modifications included in this thesis also allow the ability for migration to cease and even outward migration to occur due to the local thermal and viscous diffusion times in a disc equaling the horseshoe libration time and thus maximising the outward corotation torque such that it overcomes the inward Lindblad torques (or type I migration).

6. *Eccentricity and inclination damping.* The tidal interactions that give rise to type I migration also causes the damping of the orbital eccentricities and inclinations of planets.

7. *Gap formation.* Planets of a sufficient mass are able to clear the disc in their local vicinity of gas material, creating a gap in the disc. This stops the effects of Lindblad and corotation torque driven migration and switches a planet's migration to match the viscous evolution timescale of the disc i.e. type II migration.

8. *Gas accretion.* Sufficiently massive planets are able to accrete a gas envelope by accreting gas material from the nebula disc. For this to occur, a planet has to grow massive enough while there is still gas disc mass remaining, i.e. within the gas lifetime of the disc.

The models contained in this thesis demonstrate that strong corotation torques can substantially alter the qualitative outcomes of planet formation simulations. Even the simplest model of planet formation that involves non linear gravitational interaction between protoplanets and planetesimals during planetary accumulation is by its nature a chaotic process. Given a well-defined distribution of initial protoplanet/planetesimal masses and orbital elements from which individual

formation models are drawn, an ensemble of such models should give rise to a distribution of outcomes with well-defined statistical properties.

Allowing the set of initial conditions to be drawn from a range of disc models whose life-times, surface density and temperatures are either well-defined as in chapter 3 or carefully modelled as in 4 serve only to modify the distribution of outcomes, as does including additional physical processes such as type I migration. A corollary of this argument is that increasing the complexity of migration processes, as I have done in this paper, also serves to modify the distribution of outcomes in a quantifiable manner. In principle, this suggests that a statistically deterministic model of planetary formation can be developed that can be meaningfully compared with observational data. This work represents a step towards this ultimate goal.

Corotation torques, however, increase the dependency of formation outcomes on the details of the underlying disc model and microphysical processes such as those that control the opacity of disc material. The impact of this is only enhanced when the disc is modelled thoroughly rather than with a simple power law based model. The dependency of migration on opacity, turbulent viscosity and other disc properties, and the role of migration in shaping planetary system architectures increases the need for more refined observations of protoplanetary disc properties and improved disc models to allow planetary formation calculations to be compared with data on extrasolar planet systems in a meaningful way.

Future work would include modifications to the disc to deal with time stepping problems. An initial approach could be to limit the depth of gaps formed in the disc and also to evaporate off gap forming planets that reach short periods and give troublesome timesteps. A further approach would be to use an implicit solver to resolve the time stepping issue. A regime by which dense planetesimal regions in discs that have lost all protoplanets could generate new protoplanets would allow these regions of the disc to evolve in a more physical manner rather than all growth being switched off due to the lack of larger bodies. This could spawn a second generation of planet formation which could give rise to giant planet formation in discs that are either more massive or have a low photoevaporation criterion. A modification to include the effects of gas accretion on planetary lumi-

nosity that in turn regulates the effective cross-sectional capture radius of planets should also be incorporated. This would likely reduce the solids component of larger planets such as neptune-type and gas planets. Longer term modifications would include moving to a two dimensional disc model and switching to a model that can use the highly parallel capabilities of GPGPU machines which would allow a significant improvement in resolution and simulation domain.

To summarise: planetary formation is a chaotic process, but is deterministic in a statistical sense. Corotation torques do not change the validity of this statement, however, they can be included to construct realistic planetary formation models if they are modelled with a sufficient level of complexity.

References

I Adachi, C Hayashi, and K Nakazawa. The gas drag effect on the elliptical motion of a solid body in the primordial solar nebula. *Prog. Theor. Phys.*, 56: 1756–1771, December 1976. 27

Natalie M. Batalha, William J. Borucki, Stephen T. Bryson, Lars A. Buchhave, Douglas A. Caldwell, Jørgen Christensen-Dalsgaard, David Ciardi, Edward W. Dunham, Francois Fressin, Thomas N. III Gautier, Ronald L. Gilliland, Michael R. Haas, Steve B. Howell, Jon M. Jenkins, Hans Kjeldsen, David G. Koch, David W. Latham, Jack J Lissauer, Geoffrey W. Marcy, Jason F. Rowe, Dimitar D. Sasselov, Sara Seager, Jason H. Steffen, Guillermo Torres, Gibor S. Basri, Timothy M. Brown, David Charbonneau, Jessie Christiansen, Bruce Clarke, William D. Cochran, Andrea Dupree, Daniel C. Fabrycky, Debra Fischer, Eric B. Ford, Jonathan Fortney, Forrest R. Girouard, Matthew J. Holman, John Johnson, Howard Isaacson, Todd C. Klaus, Pavel Machalek, Althea V. Moorehead, Robert C. Morehead, Darin Ragozzine, Peter Tenenbaum, Joseph Twicken, Samuel Quinn, Jeffrey VanCleve, Lucianne M. Walkowicz, William F. Welsh, Edna Devore, and Alan Gould. Kepler's First Rocky Planet: Kepler-10b. *The Astrophysical Journal*, 729(1):27, March 2011. 1, 154

J P Beaulieu, D P Bennett, P Fouqué, A Williams, M Dominik, U G Jørgensen, D Kubas, A Cassan, C Coutures, J Greenhill, K Hill, J Menzies, P D Sackett, M Albrow, S Brillant, J A R Caldwell, J J Calitz, K H Cook, E Corrales, M Desort, S Dieters, D Dominis, J Donatowicz, M Hoffman, S Kane, J B Marquette, R Martin, P Meintjes, K Pollard, K Sahu, C Vinter, J Wambsganss, K Woller, K Horne, I Steele, D M Bramich, M Burgdorf, C Snodgrass,

M Bode, A Udalski, M K Szymański, M Kubiak, T Więckowski, G Pietrzyński, I Soszyński, O Szewczyk, Wyrzykowski, B Paczyński, F Abe, I A Bond, T R Britton, A C Gilmore, J B Hearnshaw, Y Itow, K Kamiya, P M Kilmartin, A V Korpela, K Masuda, Y Matsubara, M Motomura, Y Muraki, S Nakamura, C Okada, K Ohnishi, N J Rattenbury, T Sako, S Sato, M Sasaki, T Sekiguchi, D J Sullivan, P J Tristram, Yock, P. C. M., and T Yoshioka. Discovery of a cool planet of 5.5 Earth masses through gravitational microlensing. *Nature*, 439(7):437–440, January 2006. 11

K R Bell and D N C Lin. Using FU Orionis outbursts to constrain self-regulated protostellar disk models. *Astrophysical Journal*, 427:987–1004, June 1994. 42, 98

K R Bell, P M Cassen, H H Klahr, and Th Henning. The Structure and Appearance of Protostellar Accretion Disks: Limits on Disk Flaring. *Astrophysical Journal v.486*, 486:372, September 1997. 41, 98

B Bitsch and W Kley. Orbital evolution of eccentric planets in radiative discs. *Astronomy and Astrophysics*, 523:30, November 2010. 44, 82, 102

A. C. Boley, M. J. Payne, S. Corder, W. R. F. Dent, E. B. Ford, and M. Shabram. Constraining the Planetary System of Fomalhaut Using High-resolution ALMA Observations. *The Astrophysical Journal Letters*, 750(1):L21, May 2012. 1

William J. Borucki, David G. Koch, Gibor Basri, Natalie Batalha, Timothy M. Brown, Stephen T. Bryson, Douglas Caldwell, Jørgen Christensen-Dalsgaard, William D. Cochran, Edna Devore, Edward W. Dunham, Thomas N. III Gautier, John C Geary, Ronald Gilliland, Alan Gould, Steve B. Howell, Jon M. Jenkins, David W. Latham, Jack J Lissauer, Geoffrey W. Marcy, Jason Rowe, Dimitar Sasselov, Alan Boss, David Charbonneau, David Ciardi, Laurance Doyle, Andrea K Dupree, Eric B. Ford, Jonathan Fortney, Matthew J. Holman, Sara Seager, Jason H. Steffen, Jill Tarter, William F. Welsh, Christopher Allen, Lars A. Buchhave, Jessie L Christiansen, Bruce D Clarke, Santanu Das, Jean-Michel Desert, Michael Endl, Daniel Fabrycky, Francois Fressin, Michael Haas, Elliott Horch, Andrew Howard, Howard Isaacson, Hans Kjeldsen, Jeffery Kolodziejczak, Craig Kulesa, Jie Li, Philip W Lucas, Pavel Machalek,

Donald McCarthy, Phillip MacQueen, Søren Meibom, Thibaut Miquel, Andrej Prsa, Samuel N Quinn, Elisa V Quintana, Darin Ragozzine, William Sherry, Avi Shporer, Peter Tenenbaum, Guillermo Torres, Joseph D Twicken, Jeffrey Van Cleve, Lucianne Walkowicz, Fred C Witteborn, and Martin Still. Characteristics of Planetary Candidates Observed by Kepler. II. Analysis of the First Four Months of Data. *The Astrophysical Journal*, 736(1):19, July 2011. 1, 154

A P Boss. Giant planet formation by gravitational instability. *Science*, 276: 1836–1839, 1997. 2, 16

G Bryden, Xingming Chen, D N C Lin, Richard P Nelson, and John C B Papaloizou. Tidally Induced Gap Formation in Protostellar Disks: Gap Clearing and Suppression of Protoplanetary Growth. *The Astrophysical Journal*, 514 (1):344–367, March 1999. 48, 49

R. Paul Butler, Steven S. Vogt, Geoffrey W. Marcy, Debra A. Fischer, Jason T. Wright, Gregory W. Henry, Greg Laughlin, and Jack J Lissauer. A Neptune-Mass Planet Orbiting the Nearby M Dwarf GJ 436. *The Astrophysical Journal*, 617(1):580–588, December 2004. 1, 154

J. E. Chambers. A hybrid symplectic integrator that permits close encounters between massive bodies. *Monthly Notices of the Royal Astronomical Society*, 304(4):793–799, April 1999. 2, 49, 108

J. E. Chambers and G. W. Wetherill. Making the Terrestrial Planets: N-Body Integrations of Planetary Embryos in Three Dimensions. *Icarus*, 136(2):304–327, December 1998. 17, 23

David Charbonneau, Lori E Allen, S Thomas Megeath, Guillermo Torres, Roi Alonso, Timothy M. Brown, Ronald L. Gilliland, David W. Latham, Georgi Mandushev, Francis T O'Donovan, and Alessandro Sozzetti. Detection of Thermal Emission from an Extrasolar Planet. *The Astrophysical Journal*, 626(1): 523–529, June 2005. 9

E I Chiang and P Goldreich. Spectral Energy Distributions of T Tauri Stars with Passive Circumstellar Disks. *Astrophysical Journal v.490*, 490:368, November 1997. 97

C J Clarke, A Gendrin, and M Sotomayor. The dispersal of circumstellar discs: the role of the ultraviolet switch. *Monthly Notices of the Royal Astronomical Society*, 328(2):485–491, December 2001. 82

P Cresswell and R P Nelson. On the evolution of multiple protoplanets embedded in a protostellar disc. *Astronomy and Astrophysics*, 450(2):833–853, May 2006. 61

P Cresswell and R P Nelson. Three-dimensional simulations of multiple protoplanets embedded in a protostellar disc. *Astronomy and Astrophysics*, 482(2): 677–690, May 2008. 103, 104

Junko K Daisaka, Hidekazu Tanaka, and Shigeru Ida. Orbital evolution and accretion of protoplanets tidally interacting with a gas disk. II. Solid surface density evolution with type-I migration. *Icarus*, 185(2):492–507, December 2006. 3, 28, 44

Gennaro D'Angelo and Francesco Marzari. Outward Migration of Jupiter and Saturn in Evolved Gaseous Disks. *arXiv.org*, astro-ph.EP:2737, July 2012. 95, 98

Gennaro D'Angelo, Willy Kley, and Thomas Henning. Orbital Migration and Mass Accretion of Protoplanets in Three-dimensional Global Computations with Nested Grids. *The Astrophysical Journal*, 586(1):540–561, March 2003. 46

Drake Deming, Sara Seager, L Jeremy Richardson, and Joseph Harrington. Infrared radiation from an extrasolar planet. *Nature*, 434(7):740–743, March 2005. 9, 154

C P Dullemond, D Hollenbach, I Kamp, and P D'Alessio. Models of the Structure and Evolution of Protoplanetary Disks. *Protostars and Planets V*, pages 555–572, 2007. 101, 117

Xavier Dumusque, Francesco Pepe, Christophe Lovis, Damien Ségransan, Johannes Sahlmann, Willy Benz, François Bouchy, Michel Mayor, Didier Queloz,

Nuno Santos, and Stéphane Udry. An Earth-mass planet orbiting Centauri B. *Nature*, 491(7):207–211, November 2012. 154

Daniel C. Fabrycky, Eric B. Ford, Jason H. Steffen, Jason F. Rowe, Joshua A Carter, Althea V Moorhead, Natalie M. Batalha, William J. Borucki, Steve Bryson, Lars A. Buchhave, Jessie L Christiansen, David R Ciardi, William D. Cochran, Michael Endl, Michael N Fanelli, Debra Fischer, Francois Fressin, John Geary, Michael R. Haas, Jennifer R Hall, Matthew J. Holman, Jon M. Jenkins, David G. Koch, David W. Latham, Jie Li, Jack J Lissauer, Philip Lucas, Geoffrey W. Marcy, Tsevi Mazeh, Sean McCauliff, Samuel Quinn, Darin Ragozzine, Dimitar Sasselov, and Avi Shporer. Transit Timing Observations from Kepler. IV. Confirmation of Four Multiple-planet Systems by Simple Physical Models. *The Astrophysical Journal*, 750(2):114, May 2012. 9

Debra A. Fischer, Geoffrey W. Marcy, R. Paul Butler, Steven S. Vogt, Greg Laughlin, Gregory W. Henry, David Abouav, Kathryn M. G. Peek, Jason T. Wright, John A. Johnson, Chris McCarthy, and Howard Isaacson. Five Planets Orbiting 55 Cancri. *The Astrophysical Journal*, 675(1):790–801, March 2008. 2

M. J. Fogg and R P Nelson. On the formation of terrestrial planets in hot-Jupiter systems. *Astronomy and Astrophysics*, 461(3):1195–1208, January 2007. 3, 82

M. J. Fogg and R P Nelson. Terrestrial planet formation in low-eccentricity warm-Jupiter systems. *Astronomy and Astrophysics*, 498(2):575–589, May 2009. 3, 88

P Goldreich and S Tremaine. The excitation of density waves at the Lindblad and corotation resonances by an external potential. *Astrophysical Journal*, 233: 857–871, November 1979. 33

J Gradie and E Tedesco. Compositional structure of the asteroid belt. *Science*, 216:1405–1407, June 1982. 20

Lee Hartmann, Zhaohuan Zhu, and Nuria Calvet. On Rapid Disk Accretion and Initial Conditions in Protostellar Evolution. *arXiv.org*, 1106:3343, June 2011. 97

C Hayashi. Structure of the Solar Nebula, Growth and Decay of Magnetic Fields and Effects of Magnetic and Turbulent Viscosities on the Nebula. *Progress of Theoretical Physics Supplement*, 70:35–53, 1981. 19, 20

Coel Hellier, D R Anderson, A Collier Cameron, M. Gillon, L Hebb, P F L Maxted, D Queloz, B Smalley, A H M J Triaud, R G West, D M Wilson, S J Bentley, B Enoch, K Horne, J Irwin, T A Lister, M Mayor, N Parley, F Pepe, D L Pollacco, D Segransan, S Udry, and P J Wheatley. An orbital period of 0.94days for the hot-Jupiter planet WASP-18b. *Nature*, 460(7):1098–1100, August 2009. 1

I Hubeny. Vertical structure of accretion disks - A simplified analytical model. *Astrophysical Journal*, 351:632–641, March 1990. 96

S Ida and D N C Lin. Toward a Deterministic Model of Planetary Formation. IV. Effects of Type I Migration. *The Astrophysical Journal*, 673(1):487–501, January 2008. 30

S Ida and D N C Lin. Toward a Deterministic Model of Planetary Formation. VI. Dynamical Interaction and Coagulation of Multiple Rocky Embryos and Super-Earth Systems around Solar-type Stars. *The Astrophysical Journal*, 719 (1):810–830, August 2010. 3

Shigeru Ida and Junichiro Makino. Scattering of planetesimals by a protoplanet - Slowing down of runaway growth. *Icarus*, 106:210, November 1993. 21

Shigeru Ida, Tristan Guillot, and Alessandro Morbidelli. Accretion and Destruction of Planetesimals in Turbulent Disks. *The Astrophysical Journal*, 686:1292, October 2008. 3, 87, 91, 138

S Inaba and M Ikoma. Enhanced collisional growth of a protoplanet that has an atmosphere. *Astronomy and Astrophysics*, 410:711, November 2003. 24, 25, 89

P B Ivanov, J C B Papaloizou, and A G Polnarev. The evolution of a supermassive binary caused by an accretion disc. *Monthly Notices of the Royal Astronomical Society*, 307(1):79–90, July 1999. 45

A Johansen, A N Youdin, and Y Lithwick. Rapid Accretion of Large Planetesimals by Gravitational Instabilities. *Workshop on Formation of the First Solids in the Solar System*, 1639:9080, November 2011. 16

Paul Kalas, James R Graham, Eugene Chiang, Michael P Fitzgerald, Mark Clampin, Edwin S Kite, Karl Stapelfeldt, Christian Marois, and John Krist. Optical Images of an Exosolar Planet 25 Light Years from Earth. *arXiv.org*, astro-ph(5):1345–, November 2008. 1, 75, 90

Jacqueline Kessler-Silacci, Jean-Charles Augereau, Cornelis P Dullemond, Vincent Geers, Fred Lahuis, Neal J II Evans, Ewine F van Dishoeck, Geoffrey A Blake, A C Adwin Boogert, Joanna Brown, Jes K Jørgensen, Claudia Knez, and Klaus M Pontoppidan. c2d Spitzer IRS Spectra of Disks around T Tauri Stars. I. Silicate Emission and Grain Growth. *The Astrophysical Journal*, 639 (1):275–291, March 2006. 16

W Kley. Mass flow and accretion through gaps in accretion discs. *Monthly Notices of the Royal Astronomical Society*, 303(4):696–710, March 1999. 48, 49

Eiichiro Kokubo and Shigeru Ida. Oligarchic Growth of Protoplanets. *Icarus*, 131:171, January 1998. 17, 23

A M Lagrange, M Bonnefoy, G Chauvin, D Apai, D Ehrenreich, A Boccaletti, D Gratadour, D. Rouan, D Mouillet, S Lacour, and M Kasper. A Giant Planet Imaged in the Disk of the Young Star Pictoris. *Science*, 329(5):57–, July 2010. 1, 75, 90

A. Léger, D. Rouan, J. Schneider, P. Barge, M. Fridlund, B. Samuel, M. Ollivier, E. Guenther, M. Deleuil, H. J. Deeg, M. Auvergne, R. Alonso, S. Aigrain, A. Alapini, J. M. Almenara, A. Baglin, M. Barbieri, H. Bruntt, P. Bordé, F Bouchy, J. Cabrera, C. Catala, L. Carone, S. Carpano, Sz. Csizmadia, R. Dvorak, A. Erikson, S. Ferraz-Mello, B. Foing, F. Fressin, D. Gandolfi, M. Gillon, Ph. Gondoin, O. Grasset, T. Guillot, A. Hatzes, G. Hébrard, L. Jorda, H. Lammer, A. Llebaria, B. Loeillet, M Mayor, T. Mazeh, C. Moutou, M. Pätzold, F. Pont, D Queloz, H. Rauer, S. Renner, R. Samadi, A. Shporer, Ch. Sotin, B. Tingley, G. Wuchterl, M. Adda, P. Agogu, T. Appour-

chaux, H. Ballans, P. Baron, T. Beaufort, R. Bellenger, R. Berlin, P. Bernardi, D. Blouin, F. Baudin, P. Bodin, L. Boisnard, L. Boit, F. Bonneau, S. Borzeix, R. Briet, J.-T. Buey, B. Butler, D. Cailleau, R. Cautain, P.-Y. Chabaud, S. Chaintreuil, F. Chiavassa, V. Costes, V. Cuna Parrho, F. de Oliveira Fialho, M. Decaudin, J.-M. Defise, S. Djalal, G. Epstein, G.-E. Exil, C. Fauré, T. Fenouillet, A. Gaboriaud, A. Gallic, P. Gamet, P. Gavalda, E. Grolleau, R. Gruneisen, L. Gueguen, V. Guis, V. Guivarc'h, P. Guterman, D. Hallouard, J. Hasiba, F. Heuripeau, G. Huntzinger, H. Hustaix, C. Imad, C. Imbert, B. Johlander, M. Jouret, P. Journoud, F. Karioty, L. Kerjean, V. Lafaille, L. Lafond, T. Lam-Trong, P. Landiech, V. Lapeyrere, T. Larqué, P. Laudet, N. Lautier, H. Lecann, L. Lefevre, B. Leruyet, P. Levacher, A. Magnan, E. Mazy, F. Mertens, J.-M. Mesnager, J.-C. Meunier, J.-P. Michel, W. Monjoin, D. Naudet, K. Nguyen-Kim, J.-L. Orcesi, H. Ottacher, R. Perez, G. Peter, P. Plasson, J.-Y. Plesseria, B. Pontet, A. Pradines, C. Quentin, J.-L. Reynaud, G. Rolland, F. Rollenhagen, R. Romagnan, N. Russ, R. Schmidt, N. Schwartz, I. Sebbag, G. Sedes, H. Smit, M. B. Steller, W. Sunter, C. Surace, M. Tello, D. Tiphène, P. Toulouse, B. Ulmer, O. Vandermarcq, E. Vergnault, A. Vuillemin, and P. Zanatta. Transiting exoplanets from the CoRoT space mission. VIII. CoRoT-7b: the first super-Earth with measured radius. *Astronomy and Astrophysics*, 506(1):287–302, October 2009. 1, 154

D N C Lin and J Papaloizou. Tidal torques on accretion discs in binary systems with extreme mass ratios. *Monthly Notices of the Royal Astronomical Society*, 186:799–812, March 1979. 37

D N C Lin and John Papaloizou. On the tidal interaction between protoplanets and the protoplanetary disk. III - Orbital migration of protoplanets. *Astrophysical Journal*, 309:846–857, October 1986. 48, 94

D N C Lin, P Bodenheimer, and D C Richardson. Orbital migration of the planetary companion of 51 Pegasi to its present location. *Nature*, 380(6):606–607, April 1996. 124

J J Lissauer. Timescales for planetary accretion and the structure of the protoplanetary disk. *Icarus (ISSN 0019-1035)*, 69:249–265, February 1987. 23

J J Lissauer. Urey prize lecture: On the diversity of plausible planetary systems. *Icarus (ISSN 0019-1035)*, 114:217–236, April 1995. 23

Jack J Lissauer. Planet formation. *In: Annual review of astronomy and astrophysics. Vol. 31 (A94-12726 02-90)*, 31:129–174, 1993. 48

Jack J Lissauer, Olenka Hubickyj, Gennaro D'Angelo, and Peter Bodenheimer. Models of Jupiter's growth incorporating thermal and hydrodynamic constraints. *Icarus*, 199:338, February 2009. 37

Jack J Lissauer, Daniel C. Fabrycky, Eric B. Ford, William J. Borucki, Francois Fressin, Geoffrey W. Marcy, Jerome A Orosz, Jason F. Rowe, Guillermo Torres, William F. Welsh, Natalie M. Batalha, Stephen T. Bryson, Lars A. Buchhave, Douglas A. Caldwell, Joshua A Carter, David Charbonneau, Jessie L Christiansen, William D. Cochran, Jean-Michel Desert, Edward W. Dunham, Michael N Fanelli, Jonathan J Fortney, Thomas N. III Gautier, John C Geary, Ronald L. Gilliland, Michael R. Haas, Jennifer R Hall, Matthew J. Holman, David G. Koch, David W. Latham, Eric Lopez, Sean McCauliff, Neil Miller, Robert C. Morehead, Elisa V Quintana, Darin Ragozzine, Dimitar Sasselov, Donald R Short, and Jason H. Steffen. A closely packed system of low-mass, low-density planets transiting Kepler-11. *Nature*, 470(7):53–58, February 2011. 2, 154

Wladimir Lyra, Sijme-Jan Paardekooper, and Mordecai-Mark Mac Low. Orbital Migration of Low-mass Planets in Evolutionary Radiative Models: Avoiding Catastrophic Infall. *The Astrophysical Journal Letters*, 715(2):L68–L73, June 2010. 33, 53

Christian Marois, Bruce Macintosh, Travis Barman, B Zuckerman, Inseok Song, Jennifer Patience, David Lafrenière, and René Doyon. Direct Imaging of Multiple Planets Orbiting the Star HR 8799. *Science*, 322(5):1348–, November 2008. 2, 11

Christian Marois, B Zuckerman, Quinn M Konopacky, Bruce Macintosh, and Travis Barman. Images of a fourth planet orbiting HR 8799. *Nature*, 468(7): 1080–1083, December 2010. 75, 90

F S Masset. A few MPEGs illustrating some aspects of planetary migration. URL http://www.maths.qmul.ac.uk/~masset/moviesmpegs.html. x, 29

F S Masset. On the Co-orbital Corotation Torque in a Viscous Disk and Its Impact on Planetary Migration. *The Astrophysical Journal*, 558(1):453–462, September 2001. 33

F S Masset. The co-orbital corotation torque in a viscous disk: Numerical simulations. *Astronomy and Astrophysics*, 387:605–623, May 2002. 33

T Matsuo, H Shibai, T Ootsubo, and M Tamura. Planetary Formation Scenarios Revisited: Core-Accretion versus Disk Instability. *The Astrophysical Journal*, 662(2):1282–1292, June 2007. 16

Michel Mayor and Didier Queloz. A Jupiter-mass companion to a solar-type star. *Nature*, 378(6):355–359, November 1995. 1, 5, 154

D S McNeil and R P Nelson. New methods for large dynamic range problems in planetary formation. *Monthly Notices of the Royal Astronomical Society*, 392 (2):537–552, January 2009. 3, 88, 156

D S McNeil and R P Nelson. On the formation of hot Neptunes and super-Earths. *Monthly Notices of the Royal Astronomical Society*, 401(3):1691–1708, January 2010. 3, 88, 156

Douglas McNeil, Martin Duncan, and Harold F Levison. Effects of Type I Migration on Terrestrial Planet Formation. *The Astronomical Journal*, 130(6): 2884–2899, December 2005. 3, 61

Kristen Menou and Jeremy Goodman. Low-Mass Protoplanet Migration in T Tauri -Disks. *The Astrophysical Journal*, 606(1):520–531, May 2004. 96

Y Miguel, O M Guilera, and A Brunini. The role of the initial surface density profiles of the disc on giant planet formation: comparing with observations. *Monthly Notices of the Royal Astronomical Society*, 412(4):2113–2124, April 2011. 3

Dimitri Mihalas and Barbara Weibel Mihalas. Foundations of radiation hydrodynamics. *New York: Oxford University Press*, 1984. 96

C Mordasini, Y Alibert, and W Benz. Extrasolar planet population synthesis. I. Method, formation tracks, and mass-distance distribution. *Astronomy and Astrophysics*, 501(3):1139–1160, July 2009a. 3, 30

C Mordasini, Y Alibert, W Benz, and D Naef. Extrasolar planet population synthesis. II. Statistical comparison with observations. *Astronomy and Astrophysics*, 501(3):1161–1184, July 2009b. 3, 87, 152

C. Moutou, M Mayor, G Lo Curto, D Segransan, S Udry, F Bouchy, W Benz, C Lovis, D Naef, F Pepe, D Queloz, N C Santos, and S G Sousa. The HARPS search for southern extra-solar planets. XXVII. Seven new planetary systems. *Astronomy and Astrophysics*, 527:63, March 2011. 2

Naor Movshovitz, Peter Bodenheimer, Morris Podolak, and Jack J Lissauer. Formation of Jupiter using opacities based on detailed grain physics. *Icarus*, 209 (2):616–624, October 2010. 17, 38, 46, 89, 105

Sergei Nayakshin, Seung-Hoon Cha, and John C Bridges. The tidal downsizing hypothesis for planet formation and the composition of Solar system comets. *Monthly Notices of the Royal Astronomical Society: Letters*, 416(1):L50–L54, September 2011. 16

R P Nelson and J C B Papaloizou. Three-Dimensional Hydrodynamic Simulations of Collapsing Prolate Clouds. *Monthly Notices of the Royal Astronomical Society*, 265:905, December 1993. 107

Richard P Nelson, John C B Papaloizou, Frédéric Masset, and Willy Kley. The migration and growth of protoplanets in protostellar discs. *Monthly Notices of the Royal Astronomical Society*, 318(1):18–36, October 2000. 48, 49

S-J Paardekooper and G Mellema. Halting type I planet migration in non-isothermal disks. *Astronomy and Astrophysics*, 459(1):L17–L20, November 2006. 30

S-J Paardekooper and G Mellema. Growing and moving low-mass planets in non-isothermal disks. *Astronomy and Astrophysics*, 478(1):245–266, January 2008. 30

S-J Paardekooper and J C B Papaloizou. On disc protoplanet interactions in a non-barotropic disc with thermal diffusion. *Astronomy and Astrophysics*, 485 (3):877–895, July 2008. 33

S-J Paardekooper, C Baruteau, A Crida, and W Kley. A torque formula for non-isothermal type I planetary migration - I. Unsaturated horseshoe drag. *Monthly Notices of the Royal Astronomical Society*, 401(3):1950–1964, January 2010. 3, 30

S-J Paardekooper, C Baruteau, and W Kley. A torque formula for non-isothermal Type I planetary migration - II. Effects of diffusion. *Monthly Notices of the Royal Astronomical Society*, 410(1):293–303, January 2011. 3, 30, 35, 36, 102

J C B Papaloizou and J D Larwood. On the orbital evolution and growth of proto-planets embedded in a gaseous disc. *Monthly Notices of the Royal Astronomical Society*, 315(4):823–833, July 2000. 3

F Pepe, M Mayor, F Galland, D Naef, D Queloz, N C Santos, S Udry, and M Burnet. The CORALIE survey for southern extra-solar planets VII. Two short-period Saturnian companions to HD 108147 and HD 168746. *Astronomy and Astrophysics*, 388:632–638, June 2002. 5

F Pepe, C Lovis, D Segransan, W Benz, F Bouchy, X Dumusque, M Mayor, D Queloz, N C Santos, and S Udry. The HARPS search for Earth-like planets in the habitable zone. I. Very low-mass planets around HD 20794, HD 85512, and HD 192310. *Astronomy and Astrophysics*, 534:58, October 2011. 2

James B Pollack, Olenka Hubickyj, Peter Bodenheimer, Jack J Lissauer, Morris Podolak, and Yuval Greenzweig. Formation of the Giant Planets by Concurrent Accretion of Solids and Gas. *Icarus*, 124(1):62–85, November 1996. 2, 17, 37, 46, 89

J. E. Pringle. Accretion discs in astrophysics. *In: Annual review of astronomy and astrophysics. Volume 19. (A82-11551 02-90) Palo Alto*, 19:137–162, 1981. 93

Bun'ei Sato, Debra A. Fischer, Gregory W. Henry, Greg Laughlin, R. Paul Butler, Geoffrey W. Marcy, Steven S. Vogt, Peter Bodenheimer, Shigeru Ida, Eri Toyota, Aaron Wolf, Jeff A Valenti, Louis J Boyd, John A. Johnson, Jason T. Wright, Mark Ammons, Sarah Robinson, Jay Strader, Chris McCarthy, K L Tah, and Dante Minniti. The N2K Consortium. II. A Transiting Hot Saturn around HD 149026 with a Large Dense Core. *The Astrophysical Journal*, 633 (1):465–473, November 2005. 154

Aurora Sicilia-Aguilar, Lee W Hartmann, César Briceño, James Muzerolle, and Nuria Calvet. Low-Mass Stars and Accretion at the Ages of Planet Formation in the Cepheus OB2 Region. *The Astronomical Journal*, 128(2):805–821, August 2004. 49

D Stamatellos and A P Whitworth. Can giant planets form by gravitational fragmentation of discs?. *Astronomy and Astrophysics*, 480(3):879–887, March 2008. 2, 16

D Syer and C J Clarke. Satellites in discs: regulating the accretion luminosity. *Monthly Notices of the Royal Astronomical Society*, 277(3):758–766, December 1995. 45

Hidekazu Tanaka, Taku Takeuchi, and William R Ward. Three-Dimensional Interaction between a Planet and an Isothermal Gaseous Disk. I. Corotation and Lindblad Torques and Planet Migration. *The Astrophysical Journal*, 565 (2):1257–1274, February 2002. 28

Caroline Terquem and John C B Papaloizou. Migration and the Formation of Systems of Hot Super-Earths and Neptunes. *The Astrophysical Journal*, 654 (2):1110–1120, January 2007. 3

E W Thommes, M J Duncan, and H F Levison. Oligarchic growth of giant planets. *Icarus*, 161:431, February 2003. 21, 22, 23, 42, 43, 101

Giovanna Tinetti, Alfred Vidal-Madjar, Mao-Chang Liang, Jean-Philippe Beaulieu, Yuk Yung, Sean Carey, Robert J Barber, Jonathan Tennyson, Ignasi Ribas, Nicole Allard, Gilda E Ballester, David K Sing, and Franck Selsis. Water vapour in the atmosphere of a transiting extrasolar planet. *Nature*, 448 (7):169–171, July 2007. 9

W R Ward. Horsehoe Orbit Drag. *Abstracts of the Lunar and Planetary Science Conference*, 22:1463, March 1991. 33

William R Ward. Protoplanet Migration by Nebula Tides. *Icarus*, 126(2):261–281, April 1997. 46

Stuart J Weidenschilling. Formation of Planetesimals and Accretion of the Terrestrial Planets. *Space Science Reviews*, 92(1):295–310, April 2000. 16

F Windmark, T Birnstiel, C Güttler, J Blum, C P Dullemond, and Th Henning. Planetesimal formation by sweep-up: how the bouncing barrier can be beneficial to growth. *Astronomy and Astrophysics*, 540:73, April 2012. 16

A Wolszczan and D A Frail. A planetary system around the millisecond pulsar PSR1257 + 12. *Nature (ISSN 0028-0836)*, 355:145–147, January 1992. 14

G. Wuchterl, T. Guillot, and J J Lissauer. Giant Planet Formation. *Protostars and Planets IV (Book - Tucson: University of Arizona Press; eds Mannings*, page 1081, May 2000. 16

M R Zapatero Osorio, V J S Béjar, R Rebolo, E L Martín, and G Basri. An L-Type Substellar Object in Orion: Reaching the Mass Boundary between Brown Dwarfs and Giant Planets. *The Astrophysical Journal*, 524(2):L115–L118, October 1999. 14